

Diss. ETH No. 25968

**Experimental and virtual methods for the prediction
of the onset of ductile fracture in cross rolling
operations**

A thesis submitted to attain the degree of
DOCTOR OF SCIENCES of ETH ZURICH
(Dr. Sc. ETH Zürich)

Presented by

Tim Komischke

MSc ETH Mechanical Engineering

Born on 09 September 1990

from Germany

accepted on the recommendation of

Prof. Dr. Pavel Hora, examiner

Prof. Dr. Wolfram Volk, co-examiner

2019

Acknowledgements

This thesis was written during my employment at the Institute of Virtual Manufacturing at ETH Zürich. I would like to thank the Head of the Institute, Prof. Dr. Pavel Hora for offering me this opportunity and the trust he had in me. While granting me an autonomous project lead over most time of the employment, he was always available to give valuable inputs and new ideas in times of uncertainty. Many thanks also go to Prof. Dr. Wolfram Volk for taking over the position as co-examiner.

Special thanks also goes to the HILTI AG for providing the needed machinery, material and workforce for the experimental validations. I want to thank Mr. Günter Domani in particular for the great organization of our cooperation within the company and the numerous fruitful discussions we had on experimental procedures, tooling and rolling processes in general. Further thanks go to Mr. Robert Müller for operating the rolling machine used for experimental validation. His patience and willingness to achieve good results were highly appreciated.

Furthermore, I want to thank my more experienced researcher colleagues at the Institute of Virtual Manufacturing, Dr. Niko Manopulo and Dr. Bekim Berisha for always being open to questions and the helpful support they gave me.

Last but not least I want to thank my parents Birgit and Martin for making my studies possible and for their encouragements during my doctoral studies. Likewise special thanks go to Nadine for her encouraging positivity, support and motivation.

*Zürich, January 2019
Tim Komischke*

Abstract

In a more and more globalized manufacturing environment, companies in high wage countries have to be able to offer high quality defect-free products. This thesis gives a methodology to virtually assess the producibility of cross rolled products with respect to the occurrence of core cracks at an early stage of the product development process. This knowledge can save reworking time and costs and like this contribute to a company's international competitiveness.

The basis of a virtual model of these cross rolling processes is an adequate material modelling. The calibration of the investigated ductile fracture criteria is performed using various tensile and torsion experiments. The material's hardening behavior is investigated in compression tests. When approximating and extrapolating the material's hardening behavior, special attention has to be paid on the large strain hardening behavior, which was found to be highly relevant in numerical simulations of cross rolling operations.

While there is a variety of ductile fracture criteria available, it is not clear, which one of them is an accurate choice to predict core crack occurrence in cross rolling operations precisely. To investigate this question, a set of rollers is specifically designed to investigate the core crack occurrence under varying rolling conditions. Numerous cross rolling experiments are performed on a 20MnB4 low alloyed tempered steel and the dependency of crack occurrence on process parameters is assessed. A methodology to determine the instant of initiation of internal core cracks on the rolled samples is developed and applied. A virtual process model of the various cross rolling experiments was developed and stress and strain states in the workpiece core during rolling are investigated in detail. The previously calibrated ductile fracture criteria are implemented into finite element software packages and applied to the virtual models of the cross rolling processes. A comparison between the predicted instant of ductile fracture initiation and the experimentally observed one reveals that the Mohr-Coulomb ductile fracture criterion is an adequate choice for the prediction of core crack initiation in cross rolling processes.

Zusammenfassung

In einem zunehmend globalisierten Wettbewerbsumfeld müssen produzierende Unternehmen in Hochlohnländern in der Lage sein, qualitativ hochwertige, fehlerfreie Produkte zu liefern. Diese Arbeit trägt dazu bei, indem sie eine Methodik gibt, die Herstellbarkeit quergewalzter Produkte im Hinblick auf das Auftreten von Kernrissen zu einem frühen Zeitpunkt im Produktentstehungsprozess virtuell zu beurteilen. So können Nacharbeitskosten und –zeit gespart werden.

Eine Voraussetzung zur Modellierung dieser Querwalzprozesse ist eine geeignete Materialmodellierung. Die Parameteridentifikation der untersuchten duktilen Versagensmodelle wurde anhand von Zug- und Torsionsversuchen durchgeführt. Das Verfestigungsverhalten des Materials wurde in Stauchversuchen untersucht. Bei der Approximation und Extrapolation des Verfestigungsverhaltens wurde besonderes Augenmerk auf das Verhalten bei sehr hohen Dehnungen gelegt, da dieses sehr relevant für eine korrekte numerische Simulation von Querwalzprozessen ist.

Da es sehr viele verschiedene duktile Versagenskriterien gibt, ist nicht klar, welches Kriterium am genauesten ist, um das Auftreten von Kernrissen in Querwalzprozessen vorauszusagen. Um dies zu untersuchen, wurde eine Reihe von Walzen ausgelegt, welche unter verschiedenen Belastungszuständen zu Kernrissen führen. Zahlreiche Querwalz-Experimente wurden an einem 20MnB4 Stahl durchgeführt und die Abhängigkeit der Rissentstehung von verschiedenen Prozessparametern untersucht. Eine Methodik zur Ermittlung der Rissinitiierung der internen Kernrisse wurde entwickelt und angewendet. Ein virtuelles Modell der Querwalzprozesse wurde entwickelt und die Dehnungs- und Spannungszustände im Kern während der Umformung wurden detailliert untersucht. Verschiedene Versagensmodelle wurden in Finite Elemente Software implementiert und auf die Simulationen der Querwalzprozesse angewendet. Ein Vergleich der Voraussage der Rissinitiierung der Versagensmodelle und der tatsächlich experimentell beobachteten Rissinitiierung zeigt, dass das Mohr-Coulomb Versagensmodell gut in der Lage ist, die Kernrissinitiierung vorauszusagen.

Table of contents

Acknowledgements.....	II
Abstract.....	IV
Zusammenfassung.....	VI
Table of contents	VIII
List of abbreviations	XIV
1 Introduction.....	1
1.1 Cross rolling	1
1.1.1 Classification of the cross rolling process	1
1.1.2 Fields of application	3
1.1.3 Possible workpiece defects.....	5
1.2 Modelling core fracture in cross rolling	7
1.3 Need for research.....	10
1.4 Goal of this study.....	11
1.5 Organization of this study.....	12
2 Basics on the simulation of cross rolling processes.....	13
2.1 Continuum mechanics	13
2.1.1 Body and kinematics	13
2.1.2 Displacement, velocity, acceleration	14
2.1.3 Deformation and strain measures	15
2.1.4 Forces and stress measures.....	16
2.2 Parametrization of stress and strain states	18
2.3 Plasticity	21

2.3.1	Hardening.....	21
2.3.2	Yield locus	24
2.4	The finite element method.....	26
2.4.1	Discretization of continuous problems.....	26
2.4.2	Calculation procedures.....	27
2.4.3	Critical aspects of discretization.....	29
2.5	Ductile fracture modelling.....	31
2.5.1	Parametrization of fracture criteria.....	33
2.5.1.1	Modified Haigh Westergaard parametrization ..	33
2.5.1.2	Mixed stress strain parametrization.....	35
2.5.1.3	Conversion of different parametrizations	35
2.5.1.4	On varying Lode parameter definitions	37
2.5.2	Classification and overview	38
2.5.3	Focus of this study.....	40
2.5.4	Stress based macroscopic criteria.....	41
2.5.5	Strain based macroscopic criteria.....	43
2.5.6	Mixed stress- strain based macroscopic criteria.....	44
2.5.7	Damage accumulation rules	47
2.5.8	Continuum damage mechanics.....	48
2.5.9	Microscopic criteria- porous plasticity.....	49
2.5.10	Experimental methods for calibration.....	51
3	Cross rolling related material characterization.....	53
3.1	General considerations on the raw material.....	53
3.2	Characterization demands of cross rolling processes	54
3.3	Hardening behavior of 20MnB4	56
3.3.1	Methodology	56
3.3.2	Friction compensation.....	57
3.3.3	Results and mathematical approximation.....	59

3.3.3.1	Validation through torsion experiments	63
3.3.3.2	Validation through hardness measurements	65
3.4	Experimental fracture behavior of 20MnB4	67
3.4.1	Experimental setup and program	67
3.4.2	Evaluation methodology	69
3.4.3	Stress- and strain paths to fracture	73
3.4.4	Parametrization of the average stress state	74
3.4.5	Temperature- and strain rate dependency	76
3.4.6	Repeatability	78
3.5	Mathematical approximations to predict fracture	79
3.5.1	Parameter identification	80
3.5.1.1	Johnson Cook fracture criterion	80
3.5.1.2	Mohr Coulomb fracture criterion	81
3.5.1.3	Hosford Coulomb fracture criterion	83
3.5.2	Evaluation	84
3.5.3	Interpretation	85
3.5.4	Analysis of robustness	86
3.5.4.1	Procedure	86
3.5.4.2	Evaluation	87
4	Analysis of core cracking in cross rolling experiments	91
4.1	Raw material preforming	92
4.2	Tool geometry and experimental setup	93
4.3	Experimental methodology	95
4.4	Experimental program	98
4.5	Linear one-dimensional machine stiffness model	99
4.6	Derivation of machine control inputs	100
4.7	Cooling effect of the emulsion	103
4.8	Experimental fracture results	104

4.9	Repeatability and stability	106
4.9.1	Process repeatability and stability	106
4.9.2	Core crack-repeatability	107
5	Simulative analysis of cross rolling experiments	109
5.1	Simulative setup and preparation.....	109
5.1.1	Basics on simulative procedure.....	110
5.1.2	Details on cross rolling simulative setup.....	111
5.1.3	Simulation of preforming operation	113
5.2	Simulated process variables.....	115
5.2.1	Validation of used hardening model.....	115
5.2.2	Analysis of stress- and strain distribution	116
5.2.2.1	Strain distribution	116
5.2.2.2	Stress distribution	117
5.2.3	Definition of the critical particle	119
5.2.4	Stress and strain states at the critical particle	120
5.2.5	Comparison with standard experiments	124
5.2.6	Repeatability	125
5.2.7	Analysis of workpiece temperature distribution.....	126
5.3	Virtual prediction of core crack initiation.....	128
5.3.1	On the variation of stress state over the process.....	128
5.3.2	Preforming operation.....	129
5.3.3	Damage distribution over the workpiece.....	130
5.3.4	Fracture prediction (linear accumulation)	132
5.3.5	Fracture prediction (quadratic accumulation).....	135
5.3.6	Evaluation of robustness of fracture prediction.....	137
5.3.7	Incorporating material data scattering	138
5.3.8	Summary on core crack prediction.....	140
5.4	Analysis of robustness of numerical results.....	141

5.4.1	Modelling of friction	143
5.4.2	Modeling of heat transfer	144
5.4.3	Discretization error.....	145
5.4.3.1	Core Mesh	145
5.4.3.2	Outer Mesh.....	146
5.4.4	Modeling of material hardening.....	147
5.4.4.1	Simulated core strains and stresses.....	147
5.4.4.2	Shape of the MC fracture criterion	147
5.4.4.3	Combined effect	150
5.4.5	Summary on numerical robustness.....	151
6	Summary and conclusions.....	153
	Appendix.....	157
	List of references	167
	List of publications.....	175
	Curriculum Vitae	177

List of abbreviations

Abbreviations

AE <i>i</i>	Absolute error <i>i</i>
bcc	body center cubic crystal structure
CAE	Computer aided engineering
CDM	Continuum damage mechanics
CWR	Cross wedge Rolling
DR	Strain rate
fcc	Face center cubic crystal structure
FE	Finite Element
FEM	Finite Element Method
FLC	Forming limit curve
GTN	Gurson-Tvergaard-Needleman
HC	Hosford-Coulomb
hcp	Hexagonal closed packed crystal structure
HTC	Heat transfer coefficient to environment
JC	Johnson-Cook
MAE	Mean absolute error
MC	Mohr Coulomb
Mmax(AE)	Mean maximum absolute error
R <i>i</i>	Cross rolling experiment <i>i</i>
RVE	Representative volume element
TE <i>i</i>	Tensile experiment <i>i</i>
TL	Total Lagrange
TO <i>i</i>	Torsion experiment <i>i</i>
UL	Updated Lagrange

Greek letters

$\boldsymbol{\varepsilon}$	Strain tensor
ε	True uniaxial strain
	Or: Emission coefficient
$\bar{\varepsilon}$	Equivalent strain
$\dot{\bar{\varepsilon}}$	Equivalent strain rate
$\dot{\boldsymbol{\varepsilon}}$	Strain rate tensor
$\delta\boldsymbol{\varepsilon}$	Virtual strain vector
ε_{eng}	Engineering strain
ε_f	Equivalent fracture strain
$\varepsilon_{f, \text{fit}, i}$	Eq. fracture strain approximated for experiment i
$\varepsilon_{f, \text{meas}, i}$	Eq. fracture strain measured in experiment i
ε_i	i-th principal strain
ε_p	Plastic strain
ε_v	Volumetric strain
η	Stress triaxiality
$\eta_{\text{Av, lin}}$	Linearly averaged Stress triaxiality
$\eta_{\text{Av, quad}}$	Quadratically averaged Stress triaxiality
η_{PS}	Stress triaxiality in plane stress
θ	Lode angle parameter
$\bar{\theta}$	Normalized Lode angle parameter
$\bar{\theta}_{\text{Av,quad}}$	Quadratic. averaged Norm. Lode angle parameter
$\bar{\theta}_{\text{Av,lin}}$	Linearly averaged Norm. Lode angle parameter
$\bar{\theta}_{\text{PS}}$	Normalized Lode angle parameter in plane stress
λ	Plastic multiplier
μ	Coulomb friction coefficient
ξ	Normalized third deviatoric stress invariant
$\boldsymbol{\sigma}$	Cauchy stress tensor
σ	True uniaxial stress
$\bar{\sigma}$	Equivalent von Mises stress
$\tilde{\sigma}$	Effective stress
σ_{eng}	Engineering stress

σ_{Fit}	Approximated uniaxial stress
σ_H	Hydrostatic stress
σ_{HF}	Equivalent Hosford stress
σ_i	i-th principal stress
σ_m	Hydrostatic stress
σ_{Meas}	Experimentally measured uniaxial stress
σ_n	Normal stress on an arbitrary plane
σ_{Sat}	Saturation stress
$\sigma_{x, y, z}$	Stress in x, y or z-direction
σ_y	Yield stress
τ	Shear stress on an arbitrary plane
Φ	Angle of internal friction (Parameter of MC model) Or: Flow potential of Gurson model
Ω	Body Or: Rollers' rotational velocity

Latin letters

A	Current surface area Or: Parameter of hardening curve approximation
a	Hosford exponent
A_0	Initial surface area
b	Parameter of MC model
B	Strain-displacement matrix
C	Deformation energy
C	Elastic material matrix
c	Parameter of the hardening curve Or: Parameter of MC model
c1	Parameter of MC model Or : Parameter of HC model Or: Parameter of hardening curve
c2	Parameter of MC model Or : Parameter of HC model Or: Parameter of hardening curve
C_i	Constants of the JC damage model Or: Constants of the Xue-Wierzbicki damage model
D	Damage Or: Rolled workpiece diameter
D	Rate of deformation tensor
ΔD	Diameter reduction
ΔD_{Mach}	Diameter reduction entered into the machine control
ΔD_{Real}	True diameter reduction on the workpiece
dA	Infinitesimal surface element
D_{center}	Diameter in the center of the rolled notch
$D_{\text{crack-init}}$	Diameter of core crack initiation
D_{crit}	Critical damage value for fracture
$D_{\text{crit,safe}}$	Critical damage value adjusted by safety factor
D_{edge}	Diameter on the edge of the rolled notch

D_i	Constants of the Bai Wierzbicki damage model
D_{lin}	Linearly accumulated damage
D_{quad}	Quadratically accumulated damage
\mathbf{e}	Strain deviator tensor
\mathbf{F}	Deformation gradient tensor
	Or: Force vector
F	Uniaxial force
	Or: Plastic flow function
f	Pore volume fraction
df_{growth}	Increase of f due to pore growth
df_{nucl}	Increase of f due to pore nucleation
\mathbf{f}^B	Body forces per volume
\mathbf{f}^S	Surface forces per surface
\mathbf{H}	Displacement interpolation matrix
h	Probe height
h_{start}	Distance from rollers to workpiece at process-start
H_V	Vicker's hardness
\mathbf{I}	Identity matrix
I_i	i -th invariant of a tensor
j	Experimental combinations for robustness analysis
k	Correction factor for simulated torque under torsion
K_{mach}	linear one dimension rolling machine stiffness
l	Current length
l_0	Initial length
\mathbf{L}	velocity gradient tensor
m_1	Coefficient of temperature in hardening curve
m_2	Coefficient of strain rate in hardening curve
n	Damage exponent
	Or: Hardening exponent
\mathbf{n}	Normal vector
N	Number of workpiece revolutions
N_{Mach}	N entered into the machine control
N_{Real}	True N experienced by the workpiece
P_i	Position i in the cross rolled workpiece
\dot{Q}	Cooling rate of the emulsion

r	Probe radius
\mathbf{R}	Rotation tensor
\mathbf{R}^C	Vector of point forces
R_i	Rolling experiment i
\mathbf{s}	Stress deviator tensor
S	Surface
\tilde{S}	Effective surface
S_0	Shear Strength (Parameter of MC model)
S_f	Safety factor
\mathbf{t}	Stress vector
T	Temperature
t	Time
\mathbf{u}	Displacement field
$\delta\mathbf{u}$	Virtual displacement vector
$\hat{\mathbf{u}}$	Nodal displacement vector
$\delta\hat{\mathbf{u}}$	Virtual nodal displacement vector
\mathbf{U}	Stretch tensor
\mathbf{v}	Velocity field
V	Volume
\mathbf{x}	Current coordinates
\mathbf{X}	Reference coordinates
X	Workpiece revolutions per diameter reduction
X_{Mach}	X entered into the machine control
X_{Real}	True X experienced by the workpiece
Y	Ratio of core-strain over strain at outer diameter
z	Relative error in predicted ΔD to fracture

1 Introduction

In an environment of increasing globalization, the manufacturing industry is facing growing pricing pressure from countries with lower labour costs. In order to stay competitive, especially companies in higher wage countries have to be able to offer high quality, defect-free products. This creates the need to assess the defect-free producibility of new products prior to start of production. While some companies base their decisions concerning product producibility on experience or a trial-and-error approach, the more reproducible and often cheaper way is to make use of computer aided engineering (CAE) tools. For the planning and design of forming processes frequently used CAE tools are software packages making use of the finite element method (FEM). These allow for a quick assessment of needed process forces, workpiece temperatures, internal stresses and strains and many more. The goal of this study is to develop a numerical methodology that allows to virtually assess the occurrence of internal cracks, known as Mannesmann fracture, in cross rolling processes using existing CAE frameworks.

1.1 Cross rolling

1.1.1 Classification of the cross rolling process

According to (DIN8583-2) cross rolling is a compressive forming method with rotating tools, the rollers. For special applications instead of rotating tools flat roller dies are used. In contrast to longitudinal and helical rolling processes, in cross rolling processes, the rotating workpiece does not move axially during forming.

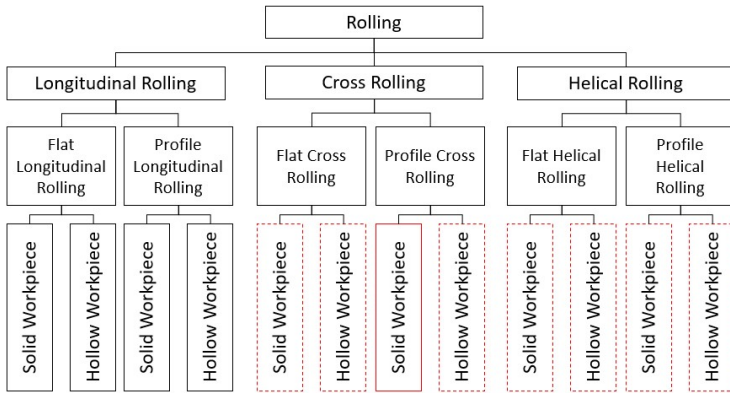


Figure 1: Classification of rolling processes according to (DIN8583-2). Red Frames: Focus of this study

Figure 1 shows the Classification of rolling processes according to (DIN8583-2). Besides the classification with respect to kinematics, the norm also differentiates between workpiece- and tool geometries. The illustration also indicates the main process focus of this work (red solid frame), which is the profile cross rolling of solid bars. Nevertheless, the results worked out in this study are expected to be transferrable to the other classes of rolling processes (red dashed frames) since the same internal crack effects are encountered in these forming processes. Especially some helical rolling processes of hollow products make active use of the Mannesmann-effect, like for example the hot rolling of seamless tubes.

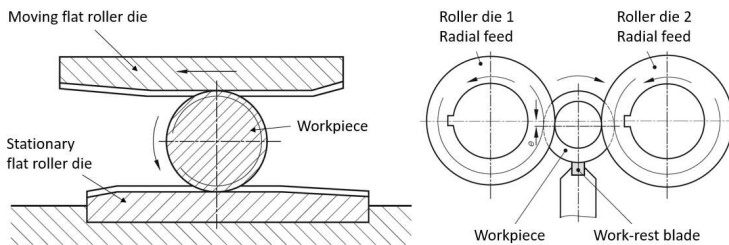


Figure 2: Left: Flat cross rolling, Right: Profile cross rolling of solid workpieces, translated from (Fritz & Schulze, 2010)

Cross rolling processes can be classified with respect to differences in tool geometry and tool motion. The process can either be carried out with flat tools moving translationally (eg. Cross wedge rolling) or with round tools rotating combined with a radial feed movement (Profile cross rolling). Figure 2 compares the flat cross rolling process with the profile cross rolling process.

1.1.2 Fields of application

A large variety of products can be produced by cross rolling. Figure 3 illustrates some exemplary products. Various preforms, shaft products, helical gears, such as transmission gear shafts, various threaded products and spline geometries are formed by cross rolling operations. Of course, this list of possible products is by far not complete.

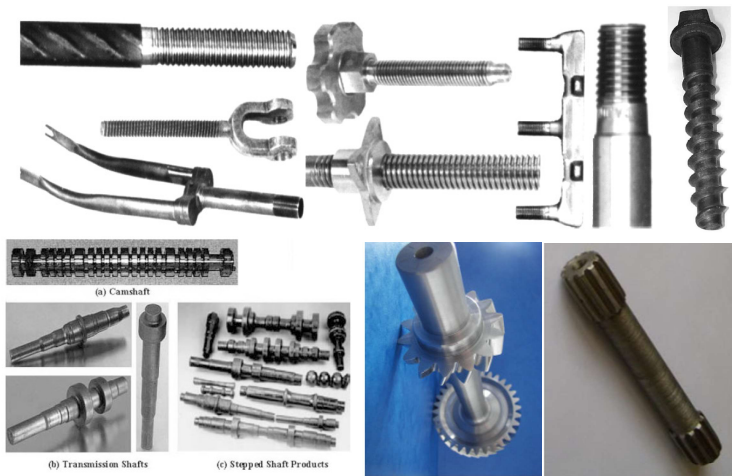


Figure 3: Various products formed by cross rolling operations (Kukielka & Kukielka, 2006; Li & Lovell, 2004; Neugebauer, Hellfritzsch, & Lahl, 2008; Pater, Gontarz, & Weronki, 2004; Zhang & Zhao, 2014)

The widespread application of cross rolling is due to its many advantages in comparison with other production processes. (Fritz & Schulze, 2010) and (Li & Lovell, 2008) summarized these advantages:

- 1) High productivity. Up to 30 parts per minute.
- 2) Strongly hardened end product, especially threads.
- 3) Optimal material usage. No waste material.
- 4) Good surface quality.
- 5) Increased fatigue resistance.

Cross rolling operations can be either performed as hot forming above recrystallization temperature or as cold forming processes. Hot cross rolling implies higher costs and lower accuracy due to temperature caused changes of dimensions but increased formability to fracture. Cold formed products on the other hand can be cheaper and have increased strength due to the plastic strain they have experienced. For these reasons products are produced in cold forming processes whenever the process limitations allow it. It is therefore of major importance to be aware of possible workpiece failure mechanisms in cold cross rolling processes.

1.1.3 Possible workpiece defects

(Johnson & Mamalis, 1977) observed different workpiece defects that can occur in cross wedge rolling operations and categorized them. Figure 4 gives a summary of a literature review on possible defects in cross rolling operations. Each defect will be explained briefly including at least one relevant reference on it..

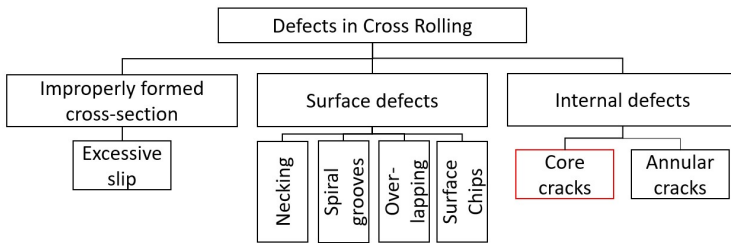


Figure 4: Classification of workpiece defects in cross rolling operations.
Red Frame: Focus in this study

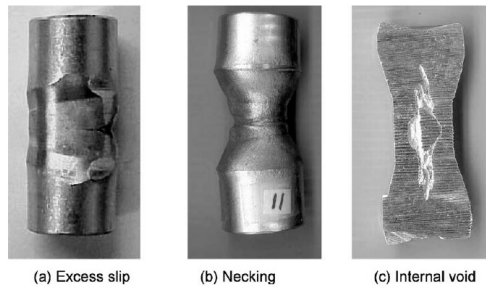


Figure 5: (Li et al., 2002) Examples of workpiece defects in CWR processes

The Improperly formed cross-section defect is characterized by compression without significant axial deformation of the workpiece. It happens due to excessive slip between workpiece and roller. In this case the interfacial forces between tool and workpiece are insufficient to cause rotational motion of the workpiece.

Necking means a thinning of the workpiece and happens in the presence of an asymmetric axial force. Spiral grooves are skrew-like features as a result of the indentation of the roll edge on the workpiece surface. Lapping in contrast happens as the workpiece folds during radial reduction (Li et al., 2002). (Houska & Rotarescu, 1999) also observed the occurrence of chip formation in cross rolling operations due to variable slip velocities on the contact surface.

Annular cracks at the mid-workpiece radius are reported in selected literature also (Dong et al., 2000), while most literature (Johnson & Mamalis, 1977) on workpiece defects in cross rolling processes has not encountered them. Much more often people encountered core cracks on the central axis of the workpiece, sometimes also referred to as “internal voids”. (Li et al., 2002) summed up that there is no clear agreement on the primary mechanisms for the formation of these cracks. This effect, also known as Mannesmann-effect is the effect that will be modelled in detail and is to be virtually predicted in the scope of this study.

1.2 Modelling core fracture in cross rolling

Different authors have simulated core crack failure in cross wedge rolling processes (CWR) making use of flat roller tools before, while no similar work was found for profile cross rolling processes with round roller tools. In this work, core crack formation in profile cross rolling processes will be experimentally investigated and modelled. Although there are some differences between CWR and profile cross rolling processes, it is assumed that the fracture criteria capable of predicting failure in CWR processes also yield good results in profile cross rolling processes and vice-versa since the core experiences similar loadings. For this reason different literature's results on the modeling of core crack occurrence in CWR processes is reviewed.

Dong (Dong et al., 2000) investigated the influence of the three process parameters in cold CWR, the forming angle, the area reduction and the friction coefficient on the stress state in the workpiece core for an Aluminum alloy through FE simulations. Their results are of relative nature, showing tendencies but lacking experimental verification.

(Li et al., 2002) in contrast conducted an extensive experimental program on a CWR machine on different materials to find the possible area reduction at the initiation of core cracks for different tool geometries. He then defined a variable that predicts the likelihood of core fracture in cold CWR processes as a function of the tool geometry and area reduction. (Li & Lovell, 2004) then also investigated the stress and strain fields in CWR processes numerically through FE simulations. He evaluated an effective stress criterion, a mean stress criterion and an effective plastic strain criterion, claiming that the effective plastic strain criterion predicts fracture best. Although they conducted experimental research on CWR, there is no experimental procedure given and no comparison, whether fracture criteria calibrated from standard experiments such as tensile and torsion tests can be used to predict core fracture in cross rolling processes. Also stress state dependency of fracture strains is not incorporated.

(Ghiotti et al., 2009) found that in the central axis of a cast bar the initial void volume fraction was clearly higher than at higher radii. Based on this finding they calibrated a modified Lemaitre model that takes pre-existing damages into account. They calibrated it from hot tensile tests both cut from the outer diameter of the bar and from the central axis. With this modelling procedure they were able to predict core crack initiation in hot tube piercing processes correctly.

(Silva, Pires, & Button, 2011) investigated the relative performance of a Cockroft-Latham criterion in the workpiece core in a hot cross rolling process for varying process parameters in a steel sample. Neither experimental investigation of the beginning of core crack occurrence during rolling nor a calibration procedure for the fracture criterion is given. The critical damage value for crack initiation could not be determined uniquely. Also (Wang, Li, & Du, 2009) showed that the Cockroft Latham criterion principally predicts the core to be the most critical region with respect to fracture in cross rolling operations on a purely relative basis without experimental verification or calibration.

(Jia et al., 2012) investigated the evolution of a relative density variable, which can be seen as his adopted fracture criterion, during FE simulations of cross rolling processes for varying process parameters. Again his simulations give purely relative results with no experimental investigation of core crack initiation and no experimental calibration procedure for fracture criteria.

(Çakırcalı et al., 2013) Cazirkah calibrated a Johnson Cook fracture criterion on round tensile and notched round tensile Titanium alloy probes under hot conditions. Experiments for calibration at lower stress triaxiality were not performed. He then conducted experiments on a CWR machine at 500°C. They monitored fracture occurrence by a drop in measured forces. It could be shown that the JC criterion predicts fracture occurrence correctly on the central axis and that it is generally able to predict core crack occurrence and expansion. Although having both experimental and numerical data on crack initiation, no clear comparison between simulated and experimentally

observed core crack initiation diameter and damage values could be found.

Reference	Year	Material	Temperature	Fracture Criterion used
(Dong et al., 2000)	1999	Aluminum alloy 1100	Cold	- Max. Shear Stress, - First principle Stress
(Li et al., 2002) (Li & Lovell, 2004)	2002-2004	Copper 11000, Aluminum 1100	Cold	- Mean stress - Effective stress - Plastic strain
(Wang, Li, & Du, 2009)	2009	AISI 5140	Hot	- Cockroft-Latham
(Ghiotti et al., 2009)	2009	DIN St52	Hot	- Lemaitre (modified)
(Silva, Pires, & Button, 2011)	2011-2012	Steel 38MnSiVS5, AISI 1045	Hot	- Cockroft Latham (modified)
(Jia et al., 2012)	2012	Aluminum 7075	Hot	- Relative density variable
(Çakırcalı et al., 2013)	2013	Ti6Al4V	Cold, max.750°C	- Johnson Cook
(Novella et al., 2015)	2014-2015	AA6082	Hot	- Oyane (modified)

Table 1: Advances in modelling of core fracture in cross rolling processes

(Novella et al., 2015) investigated and modeled core crack initiation in a hot CWR process of an Aluminum alloy with special attention on temperature and strain rate effects. They calibrated a modified Oyane Sato fracture criterion's temperature and strain rate dependency from unnotched tensile tests at different temperatures and strain rates. The stress state dependency, expressed through one constant, was chosen from literature. They then performed CWR experiments at different temperatures. The core crack occurrence could be predicted correctly for different temperatures, while the geometry of the rolled sample was not changed. Especially the question of the correct transferability of tensile test fracture strains to CWR processes remained unclear though, since part of the calibration procedure was skipped by choosing one constant from literature.

1.3 Need for research

Summing up the literature review on the modelling of the Mannesmann effect it can be concluded that there are some modelling approaches on its occurrence in CWR processes, while none on the occurrence in profile cross rolling processes was found. Furthermore, also for CWR, most fracture modelling approaches found are only of relative nature.

All studies mentioned are missing more than only one step of the following modelling and verification process chain that would be ideal from the author's point of view to guarantee a reliable virtual prediction of core crack occurrence in cross rolling processes:

- Calibration of different fracture criteria through laboratory experiments
- Execution of various cross rolling experiments under precisely defined conditions
- Investigation of core crack occurrence on the rolled samples
- Determination of core crack initiation for different rolling experiments
- Buildup of a virtual model of the performed cross rolling experiments
- Simulative prediction of core crack initiation in cross rolling processes using the calibrated criteria
- Comparison of experimental and simulated core crack initiation in cross rolling processes
- Concluding evaluation of the fracture criteria's performance

Furthermore, as it will be described in chapter 2.5 there is an abundance of ductile fracture criteria available and therefore it is not clear which fracture criterion is to be used to predict the occurrence of internal cracks in cross rolling operations reliably.

1.4 Goal of this study

The goal of this study is the reliable virtual prediction of core crack initiation in cold cross rolling operations of a conventional bulk forming steel. To avoid faulty tool design that leads to cracked products, a model for the virtual prediction of core crack initiation is created and implemented into FEM software packages in the framework of this study.

To achieve this, a precise procedure will be given. This includes the calibration of the criteria, the setup, planning and execution of the cross rolling experiments for verification, as well as their results and virtual models. The following sub-goals are formulated.

- A precise methodology to investigate the material's hardening behavior with special focus on large strain hardening.
- Development of a procedure for the measurement of material ductility in order to predict ductile fracture.
- Development of a procedure to transfer the experimental results into mathematical fracture criteria.
- Development of a precise experimental method, that causes core cracks in cross rolling experiments under varying stress states in the workpiece core.
- A precise methodology to determine the internal crack initiation in cross rolling experiments.
- Setup of a precise virtual model of the cross rolling experiments using an FEM software package.
- Simulation of the performed cross rolling experiments using the virtual model and the implemented fracture criteria.
- Evaluation of different fracture criteria's accuracy in predicting the initiation of core cracks.
- Assessment of the robustness of the numerical results obtained from cross rolling simulations.

1.5 Organization of this study

Chapter one gave an introduction to cross rolling processes and the core crack as a possible process limitation. Furthermore the state of the art in modelling core crack initiation was outlined. From this the need for research and the study goals were derived.

Chapter two will introduce the needed concepts used and applied in this thesis. This includes basics on continuum mechanics, plasticity, the finite element method and most important, basics and recent trends in the modelling of ductile fracture.

Chapter three then is the first chapter to give results from own material data acquisition on the used bulk forming material, as well as their mathematical approximations. This includes the material hardening behavior, as well as the material's fracture behavior. Also the robustness of fracture criteria when reducing the number of experiments used for calibration will be investigated.

Chapter four introduces the performed experimental setup to cause core cracks. The designed tool geometries and the experimental setup, as well as the applied procedure to find the beginning of the core cracks are described. The performed experimental program, as well as a simplified machine stiffness model are introduced. Finally, the results on core crack occurrence are given for all experiments.

Chapter five will give details on the virtual model of the cross rolling experiments. First, details on the setup are given, followed by various simulated results, such as strain and stress fields over the workpiece during rolling. In a next step, the fracture criteria are applied to the simulations of the experimental program of cross rolling operations. The accuracy of the fracture criteria in predicting core crack initiation in cross rolling is evaluated. Finally, by varying simulative parameters, such as friction, mesh size and others, the robustness of simulated results of cross rolling processes is quantified.

Chapter six will give concluding remarks.

2 *Basics on the simulation of cross rolling processes*

2.1 Continuum mechanics

Some selected concepts of continuum mechanics will be briefly explained in this section. The focus in this chapter is set on defining the quantities that are needed to understand the contents of the following chapters 2.2 to 2.5. (Belytschko, Liu, & Moran, 2000) give a detailed description of the concepts used. A precise and compressed summary of these concepts is given both by (Manopulo, 2011) and (Wesner, 2017). Chapters 2.1 to 2.4 are based on these three studies.

2.1.1 Body and kinematics

A body Ω , as a sum of particles, is assumed to change its position over time (see Figure 6). The *reference configuration* or *material configuration* X of the body is time independent. In contrast to the reference configuration the *current configuration* x is a function of time t and reference configuration X as given by equation 2.1.1.

$$x = f(X, t) \tag{2.1.1}$$

When the current configuration $x=x(t)$ is used as origin of the coordinate system at each time t the coordinates are referred to as the *Eulerian* or *spatial coordinates*. If the constant reference configuration $X=X(t)$ is used as coordinate system the coordinates are referred to as the *Lagrangian* or *material coordinates*. Most often, the Lagrangian coordinates are initialized at $t=0$, such that the relation $X=x^{t=0}$ holds.

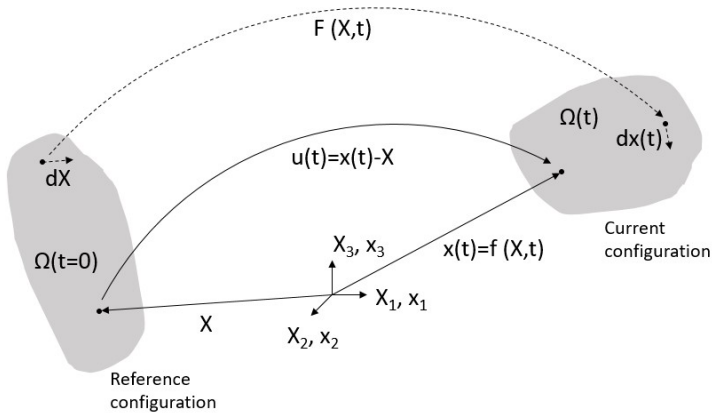


Figure 6: Reference configuration X and current configuration x of a body

2.1.2 Displacement, velocity, acceleration

In Lagrangian coordinates the displacement field of Ω can be described as follows:

$$\mathbf{u}(\mathbf{X}, t) = \mathbf{x}(t) - \mathbf{X} \quad (2.1.2)$$

Its material derivation is the particle's velocity.

$$\mathbf{v} = \dot{\mathbf{u}} = \frac{\delta(\mathbf{x}(t) - \mathbf{X})}{\delta t} = \frac{\delta \mathbf{x}(t)}{\delta t} \quad (2.1.3)$$

Since the Eulerian coordinates are not constant, the material velocity in Eulerian coordinates can be evaluated using the chain rule.

2.1.3 Deformation and strain measures

The *deformation gradient tensor* \mathbf{F} gives a mapping from an infinitesimal line element $\delta\mathbf{X}$ to an infinitesimal line element $\delta\mathbf{x}$ (see Figure 6).

$$\mathbf{F}(\mathbf{x}, t) = \frac{\delta\mathbf{x}(t)}{\delta\mathbf{X}} = \mathbf{1} + \frac{\delta\mathbf{u}(\mathbf{X}, t)}{\delta\mathbf{X}} \quad (2.1.4)$$

The non-symmetric deformation gradient \mathbf{F} can be decomposed into a rotation tensor \mathbf{R} and a symmetric stretch tensor \mathbf{U} as follows:

$$\mathbf{F} = \mathbf{R}\mathbf{U} \quad (2.1.5)$$

Many distinct strain measures exist. Only the most commonly used ones will be defined here. The *Green-Lagrange strain tensor* \mathbf{E} is a very commonly used strain measure that can be calculated from the deformation gradient tensor.

$$\mathbf{E} = \frac{1}{2}(\mathbf{F}^T\mathbf{F} - \mathbf{I}) \quad (2.1.6)$$

The *velocity gradient tensor* \mathbf{L} can be used to define the commonly used *rate of deformation tensor* \mathbf{D} .

$$\mathbf{L} = \dot{\mathbf{F}}\mathbf{F}^{-1} \quad (2.1.7)$$

$$\mathbf{D} = \frac{1}{2}(\mathbf{L} + \mathbf{L}^T) \quad (2.1.8)$$

For small deformations the following approximation is valid (MSC-Software, 2015).

$$\dot{\boldsymbol{\varepsilon}} \approx \mathbf{D} \quad (2.1.9)$$

In all upcoming calculations an updated Lagrangian formulation (see chapter 2.4.1) will be used. In case of an updated Lagrangian formulation the used finite element solver Marc of the MSC Software Corporation determines the strain tensor $\boldsymbol{\varepsilon}$ through the rate of deformation tensor \boldsymbol{D} (equations 2.1.9 and 2.1.10) (MSC-Software, 2015).

$$\boldsymbol{\varepsilon} = \int \dot{\boldsymbol{\varepsilon}} dt \quad (2.1.10)$$

2.1.4 Forces and stress measures

The stress vector \boldsymbol{t} is defined as the force vector $d\boldsymbol{F}$ acting per infinitesimal surface element dA with normal \boldsymbol{n} , defined by equation 2.1.11.

$$\boldsymbol{t} = \frac{d\boldsymbol{F}}{dA} \quad (2.1.11)$$

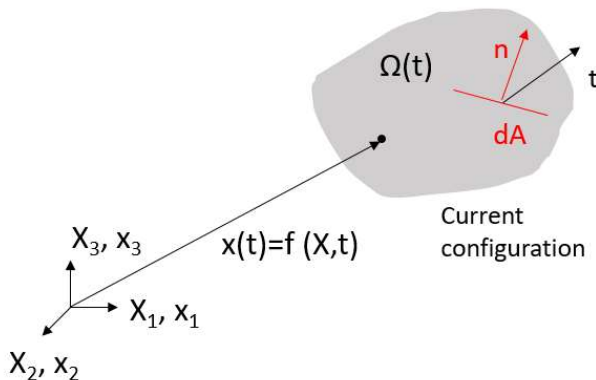


Figure 7: Illustration of the stress vector

Since the surface element dA can be chosen arbitrarily, there are infinitely many normal vectors \mathbf{n} that the relevant cutting plane can have in each single point of a 3D body. For this reason infinitely many stress vectors can be calculated in a single material point (equation 2.1.12). A second order tensor relates the normal vector to the stress vector.

$$\mathbf{t} = \boldsymbol{\sigma} \mathbf{n} \quad (2.1.12)$$

$$\boldsymbol{\sigma} = \begin{pmatrix} \sigma_{11} & \sigma_{12} & \sigma_{13} \\ \sigma_{21} & \sigma_{22} & \sigma_{23} \\ \sigma_{31} & \sigma_{32} & \sigma_{33} \end{pmatrix} \quad (2.1.13)$$

If the stress tensor is determined in the current configuration it is called the *Cauchy stress tensor* or *true stress tensor* $\boldsymbol{\sigma}$. It is symmetric and fully describes the stress state in a given material point. One way to visualize the Cauchy stress tensor is the unit cell given in Figure 8 left. Another way is the visualization by Mohr's Stress circles (Figure 8 right).

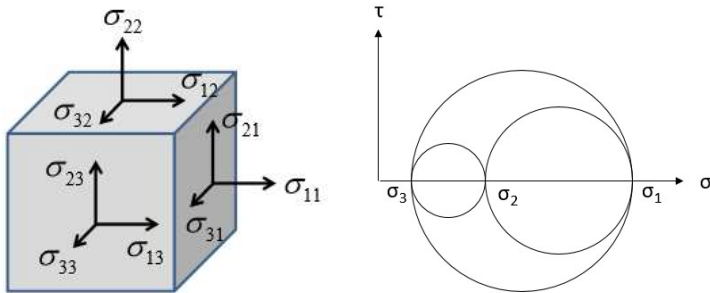


Figure 8: Visualization of the Cauchy stress tensor. Left: Infinitesimal cube, Right: Mohr's stress circles

2.2 Parametrization of stress and strain states

For each Cauchy stress tensor, there is a set of orthogonal directions, the principal directions, in which no shear stresses but only normal stresses are acting, the principal stresses σ_i . To obtain the principal stresses of the Cauchy stress tensor $\boldsymbol{\sigma}$ one has to solve the Eigenvalue-problem given by equation 2.2.1. The same holds for the principal strains ε_i .

$$\det(\boldsymbol{\sigma} - \sigma_i \mathbf{I}) = 0 \quad (2.2.1)$$

$$\det(\boldsymbol{\varepsilon} - \varepsilon_i \mathbf{I}) = 0 \quad (2.2.2)$$

The following order convention is introduced.

$$\sigma_1 > \sigma_2 > \sigma_3 \quad (2.2.3)$$

$$\varepsilon_1 > \varepsilon_2 > \varepsilon_3 \quad (2.2.4)$$

The three invariants of the Cauchy stress tensor I_1, I_2, I_3 are fully independent of the chosen coordinate system. The same holds for the stress tensor's invariants. The invariants of the stress tensor can be described as follows:

$$I_1(\boldsymbol{\sigma}) = \text{tr}(\boldsymbol{\sigma}) \quad (2.2.5)$$

$$I_2(\boldsymbol{\sigma}) = \frac{1}{2}(I_1(\boldsymbol{\sigma})^2 - I_1(\boldsymbol{\sigma}^2)) \quad (2.2.6)$$

$$I_3(\boldsymbol{\sigma}) = \det(\boldsymbol{\sigma}) \quad (2.2.7)$$

The hydrostatic stress or mean stress is an important stress measure both with respect to plastic material flow and fracture. Its comparable strain measure is the volumetric strain ε_v .

$$\sigma_h = \sigma_m = \frac{1}{3} I_1(\boldsymbol{\sigma}) \quad (2.2.8)$$

$$\varepsilon_v = I_1(\boldsymbol{\varepsilon}) \quad (2.2.9)$$

In general it is assumed that the hydrostatic stress doesn't contribute to plastic material flow of metals. For this reason the stress deviator tensor \mathbf{s} is formed as follows. The strain deviator \mathbf{e} is defined similarly.

$$\mathbf{s} = \boldsymbol{\sigma} - \sigma_h \mathbf{I} \quad (2.2.10)$$

$$\mathbf{e} = \boldsymbol{\varepsilon} - \frac{1}{3} \varepsilon_v \mathbf{I} \quad (2.2.11)$$

In order to be able to compare three-dimensional stress states to uniaxial ones, von Mises proposed the following equivalent uniaxial stress measure for isotropic materials.

$$\begin{aligned} \bar{\sigma} &= \sqrt{3I_2(\mathbf{s})} \\ &= \sqrt{\frac{1}{2} [(\sigma_1 - \sigma_2)^2 + (\sigma_2 - \sigma_3)^2 + (\sigma_3 - \sigma_1)^2]} \end{aligned} \quad (2.2.12)$$

The equivalent uniaxial strain measure is given by:

$$\begin{aligned} \bar{\varepsilon} &= \sqrt{\frac{4}{3} I_2(\mathbf{e})} \\ &= \sqrt{\frac{2}{3} [(\varepsilon_1 - \varepsilon_2)^2 + (\varepsilon_2 - \varepsilon_3)^2 + (\varepsilon_3 - \varepsilon_1)^2]} \end{aligned} \quad (2.2.13)$$

Three commonly used stress- and strain state parametrizations are used most frequently in this work.

- The first and most commonly used one is the one of principal stresses $\{\sigma_1, \sigma_2, \sigma_3\}$ and has already been introduced.
- The second one are the modified Haigh Westergaard coordinates $\{\bar{\sigma}, \eta, \bar{\theta}\}$ (see chapter 2.5.1)
- The third one is a mixed stress-strain formulation $\{\bar{\epsilon}, \eta, \bar{\theta}\}$ frequently used in terms of ductile fracture research (see chapter 2.5.1).

2.3 Plasticity

2.3.1 Hardening

When deforming a metallic material under cold isothermal conditions, in general the acting stresses in the material increase with increasing deformation. This process will be referred to as material hardening. On a microscopic scale, the hardening phenomenon is due to an increase of dislocation density in the material.

The hardening behavior can be measured by deforming a workpiece while measuring deformation and force needed. Most commonly, the material's hardening behavior is measured in uniaxial stress states, in particular uniaxial tensile tests or uniaxial compression tests. From the measured current force and length or height of the specimen one can calculate the acting engineering stress and strain:

$$\sigma_{eng} = \frac{F}{A_0} \quad (2.3.1)$$

$$\varepsilon_{eng} = \frac{l}{l_0} \quad (2.3.2)$$

Of much higher importance are the true stress and strain curves. In contrast to the engineering stress and strain they refer the acting force and elongation to the current area or length respectively. True stresses and strains are the ones currently acting on a material particle during deformation. For these reason these are the relevant inputs for numerical simulations.

$$\sigma = \frac{F}{A} \quad (2.3.3)$$

$$\varepsilon = \ln\left(\frac{l}{l_0}\right) \quad (2.3.4)$$

The true stress and true strain curves can only be measured up to certain limitations. For the uniaxial tensile test this limitation is the beginning of diffuse necking, whereas the limitation for uniaxial

compression tests is given by an excessive convexity of the probe, caused by friction phenomena, meaning a non uniaxial stress state. In order to guarantee a smooth stress- strain relationship and in order to extrapolate the stress strain curve up to higher strain values than the ones measured, mathematical approximations for the hardening behavior are used. The hardening approximations relating yield stress σ_y to current plastic strain ε_{pl} can be classified into saturating and non-saturating formulations. For simplicity reasons and since plastic strain will be much higher than elastic strains for all relevant calculations in this study, the subscript pl (plastic) will be neglected in the given formulas. A very simple frequently used non-saturating approach is the power law formulation proposed by Ludwik (Ludwik, 1909)

$$\sigma_y = \sigma_0 + A\varepsilon^n \quad (2.3.5)$$

where n is the hardening exponent. While Hollomon (Hollomon, 1945) simplified Ludwik's approach postulating $\sigma_0=0$, Ghosh (Ghosh, 1977) extended the formulation:

$$\sigma_y = A(c_1 + \varepsilon)^n - c_2 \quad (2.3.6)$$

Hensel and Spittel (Hensel & Spittel, 1979) used Hollomon's approach adding a dependency on temperature and strain rate. Unlike the formulation commonly used, the formulation given here is consistent with respect to units:

$$\sigma_y = A\varepsilon^n e^{m_1 T \frac{1}{[K]}} (\dot{\varepsilon}[s])^{m_2} e^{\frac{c}{\varepsilon}} \quad (2.3.7)$$

Saturating flow curve approaches were inspired by Voce's (Voce, 1948) investigations showing saturating flow stresses for different metals.

$$\sigma_y = \sigma_{sat} - (\sigma_{sat} - c_1)e^{-c_2\varepsilon} \quad (2.3.8)$$

Hockett and Sherby (Hockett & Sherby, 1975) modified Voce's approach:

$$\sigma_y = \sigma_{sat} - (\sigma_{sat} - c_1)e^{-c_2\varepsilon^n} \quad (2.3.9)$$

A modified version of the Hockett Sherby flow curve takes temperature- and strain rate dependency into account. Again, the formulation given here is consistent with respect to units:

$$\sigma_y = (\sigma_{sat} - (\sigma_{sat} - c_1)e^{-c_2\varepsilon^n})e^{m_1T\frac{1}{[K]}}(\dot{\varepsilon}[S])^{m_2} \quad (2.3.10)$$

Remarks on large strain hardening behavior

While the different hardening models reveal similar results for small strains (<50%), where stress strain relationships are known from mechanical testing, significant differences between the models are obtained for large strains. For this reason the chosen type of model is of significant importance for a simulation's validity when high strains are reached in the respective forming process, which is typically the case in bulk forming processes.

In (Gil Sevillano, van Houtte, & Aernoudt, 1980) different literature on the large strain hardening behavior of various metals was reviewed. The authors conclude that the Bravais lattices of the material's crystal system determine their large strain hardening behavior. For face-centered cubic (fcc) crystal systems (eg. Fe-Austenite, Al, Cu, Ag), the flow stress saturates at strains between 200 and 400%, while for body-centered cubic (bcc) crystal systems (eg. Fe-Ferrite, Nb, W) and hexagonal (hcp) crystal systems (eg. Ti), the yield stress keeps increasing also for very high strains. This finding is of high importance when choosing an appropriate approach for modeling the material's hardening, especially with respect to the model's saturation behavior.

Validating the hardening curve approximations for very high strains is demanding. A possible way to do so has been proposed by (Tabor, 1956) for the first time and then extensively been used more recently. This approach uses Hardness measurements, most commonly Vickers hardness H_v , to approximate the current flow stress σ_y . A linear relationship between Vicker's hardness and current flow stress was found in many studies, as summarized by (Pavlina & Van Tyne,

2008). The major advantage of this method is the possibility to approximate the current yield stress locally, even on a very small specimen, without any need to machine a tensile or compressive probe. A detailed study on correlating hardness to yield strength for a variety of steel alloys and yield strengths from 325MPa to 1700MPa can be found in (Pavlina & Van Tyne, 2008). In their study, they concluded empirically that for the variety of different steels investigated, the linear equation 2.3.11 minimizes the average error over all investigated steels.

$$\Delta\sigma_y = 2.876 \Delta H_v \quad (2.3.11)$$

2.3.2 Yield locus

The choice of the yield criterion determines how a three-dimensional stress state is transferred into an “equivalent” scalar uniaxial stress $\bar{\sigma}$.

$$\bar{\sigma} = f(\sigma_x, \sigma_y, \sigma_z, \tau_{xy}, \tau_{yz}, \tau_{xz}) \quad (2.3.12)$$

There are isotropic and anisotropic yield loci. An anisotropic yield locus is directionally dependent, while the isotropic one does not distinguish between different directions. While anisotropic yield loci are commonly used in sheet metal forming, where anisotropy is introduced into the material through rolling operations, in bulk metal forming anisotropic yield loci are not state of the art. In most bulk forming operations the assumption of an isotropic yield locus is reasonable because all preforming steps happen over recrystallization temperature, which means anisotropy is clearly less pronounced, if any. A general form of an isotropic yield locus is the Hershey- Hosford yield locus (Hershey, 1954; Hosford, 1979) that is given in terms of the stress tensor’s principal stresses in equation 2.3.13.

$$\bar{\sigma}_{Hos} = \sqrt[a]{\frac{1}{2} (|\sigma_1 - \sigma_2|^a + |\sigma_2 - \sigma_3|^a + |\sigma_3 - \sigma_1|^a) } \quad (2.3.13)$$

For $a=2$ the Hershey Hosford yield locus equals the von Mises yield locus already introduced (equation 2.2.12) being based on the energy needed for deformation. For $a \rightarrow \infty$ it equals the Tresca yield locus, which claims that the acting equivalent stress equals the maximum acting shear stress.

$$\bar{\sigma}_{Tresca} = \frac{1}{2} \max (|\sigma_1 - \sigma_2|, |\sigma_2 - \sigma_3|, |\sigma_1 - \sigma_3|) \quad (2.3.14)$$

A very basic anisotropic yield locus is the Hill48 yield locus given by equation 2.3.15 (Hill, 1948). Nowadays there are much more sophisticated anisotropic yield locus approximations that will not be relevant for this thesis.

$$\bar{\sigma}_{Hill48} = \left[\frac{1}{2} (F(\sigma_y - \sigma_z)^2 + G(\sigma_z - \sigma_x)^2 + H(\sigma_x - \sigma_y)^2 + 2L\sigma_{xz}^2 + 2M\sigma_{zy}^2 + 2N\sigma_{xy}^2) \right]^{\frac{1}{2}} \quad (2.3.15)$$

With the three-dimensional stress state being reduced to a scalar variable, the comparison between the current yield stress σ_y and the current equivalent stress $\bar{\sigma}$ can be performed using the flow function F , in order to determine whether plastic or elastic deformation occurs.

$$F(\boldsymbol{\sigma}, \bar{\varepsilon}) = \bar{\sigma}(\boldsymbol{\sigma}) - \sigma_y(\bar{\varepsilon}) \quad (2.3.16)$$

Plastic flow will occur for $F=0$, whereas there will not be plastic flow for $F<0$. If plastic flow occurs, it will follow the normality rule, meaning that flow will happen in a direction normal to the yield locus, where λ is the plastic multiplier.

$$\dot{\boldsymbol{\varepsilon}} = \dot{\lambda} \frac{dF}{d\boldsymbol{\sigma}} \quad (2.3.17)$$

2.4 The finite element method

The principals introduced in this section are summarized on the basis of the detailed work of (Bathe, 2006).

2.4.1 Discretization of continuous problems

According to (Bathe, 2006) solving a technical system implies the idealization of the system to a solvable form, the formulation of a mathematical model, as well as the solution and the interpretation of results. There are two distinct classes of mathematical models to describe a system's behavior, discrete and continuous models. Because continuous models can only be solved analytically for rather simple technical problems, in many cases a discrete idealization of the continuous technical problem is needed. The finite Element Method FEM is a systematic technique to discretize and solve complex continuous technical problems numerically. This method will be used extensively in this work.

The idealization is done by dividing the region of interest into elements whose boundaries are defined by meshes. There are mainly two distinct mesh types. While the *Eulerian mesh's* nodes are fixed in space meaning that the material moves between elements, the *Lagrangian mesh's* nodes are coincident with material points. In solid mechanics Lagrangian meshes are most popular.

Finite element methods using Lagrangian meshes can be classified with respect to the coordinate systems they use. While the *total Lagrangian formulation* (TL) makes use of the reference coordinate system defined at time $t=0$, the *updated Lagrangian formulation* (UL) makes use of a reference coordinate system defined at time $t-\Delta t$. Purely elastic problems typically make use of TL formulations, whereas problems with large deformations, as in this study, often use UL formulations. This is also the case for the Marc finite element solver used in this study (MSC-Software, 2015).

2.4.2 Calculation procedures

The basics of the finite element method is the *principle of virtual displacements (or work)*. It claims that the inner virtual work of a body is equal to its outer virtual work (equation 2.4.1). Assuming a quasi-static problem and neglecting thermal effects as well as initial stresses it can be written as given in equation 2.4.2 for a Lagrangian incremental analysis approach. Here, $\delta \mathbf{u}^{t+\Delta t}$ indicates virtual displacements at time $t+\Delta t$ and $\delta \boldsymbol{\varepsilon}^{t+\Delta t}$ indicates virtual strains at that time. The quantity $\mathbf{f}^{\mathbf{B}, t+\Delta t}$ represents acting body forces per volume at time $t+\Delta t$, $\mathbf{f}^{\mathbf{S}, t+\Delta t}$ represents acting surface forces per surface (stresses) and $\mathbf{R}_c^{t+\Delta t}$ represents acting single forces at that time.

$$\text{Inner Virtual work} = \text{Outer virtual work} \quad (2.4.1)$$

$$\int_{V^{t+\Delta t}} \delta \boldsymbol{\varepsilon}^{t+\Delta t} \boldsymbol{\sigma}^{t+\Delta t} dV^{t+\Delta t} = \int_{V^{t+\Delta t}} \delta \mathbf{u}^{t+\Delta t} \mathbf{f}^{\mathbf{B}, t+\Delta t} dV^{t+\Delta t} \quad (2.4.2)$$

$$+ \int_{S^{t+\Delta t}} \delta \mathbf{u}^{t+\Delta t} \mathbf{f}^{\mathbf{S}, t+\Delta t} dS^{t+\Delta t} + \sum_{i, t+\Delta t} \delta \mathbf{u}^{t+\Delta t} \mathbf{R}_c^{t+\Delta t}$$

In order to be able to solve this generally complex system, the finite element method then discretizes the system into elements. The discretization can be done by equations 2.4.3 and 2.4.4, where \mathbf{H} is the interpolation matrix for displacements for all elements and depends on the element formulation used. $\delta \hat{\mathbf{u}}^{t+\Delta t}$ is the vector of virtual nodal displacements, while $\delta \mathbf{u}^{t+\Delta t}$ is an arbitrary virtual displacement. $\hat{\mathbf{u}}^{t+\Delta t}$ is the vector of nodal displacements and $\mathbf{u}^{t+\Delta t}$ any displacement.

$$\delta \mathbf{u}^{t+\Delta t}(x, y, z) = \mathbf{H}(r, s, t) \delta \hat{\mathbf{u}}^{t+\Delta t} \quad (2.4.3)$$

$$\mathbf{u}^{t+\Delta t}(x, y, z) = \mathbf{H}(r, s, t) \hat{\mathbf{u}}^{t+\Delta t} \quad (2.4.4)$$

\mathbf{B} relates displacements to strains (equations 2.4.6 and 2.4.7) and is given by equation 2.4.5. Like \mathbf{H} , it is defined by the element formulation.

$$\mathbf{B}(x, y, z) = \text{grad}(\mathbf{H}(r, s, t)) \quad (2.4.5)$$

$$\delta \boldsymbol{\varepsilon}^{t+\Delta t}(x, y, z) = \mathbf{B}(x, y, z) \delta \hat{\mathbf{u}}^{t+\Delta t} \quad (2.4.6)$$

$$\boldsymbol{\varepsilon}^{t+\Delta t}(x, y, z) = \mathbf{B}(x, y, z) \hat{\mathbf{u}}^{t+\Delta t} \quad (2.4.7)$$

Neglecting initial stresses, \mathbf{C} relates an element's acting stresses to its strains. It is material dependent and given through the constitutive relations used (see chapter 2.3). While it is straightforward to be defined under purely elastic conditions, the determination of the elastic-plastic constitutive tensor is more demanding (Bathe, 2006). The elastic-plastic stress-strain relationship is then formulated incrementally:

$$\Delta \boldsymbol{\sigma}^{t+\Delta t} = \mathbf{C} \Delta \boldsymbol{\varepsilon}^{t+\Delta t} = \mathbf{C} \mathbf{B}^T \Delta \hat{\mathbf{u}}^{t+\Delta t} \quad (2.4.8)$$

Inserting equation 2.4.3, 2.4.6 and 2.4.8 into an incremental formulation of equation 2.4.2 and eliminating $\delta \hat{\mathbf{u}}^{t+\Delta t}$ the following *nodal force balance equation* results in case of m elements.

$$\begin{aligned} \left[\sum_m \int_{V^{t+\Delta t}} \mathbf{B}^T \mathbf{C} \mathbf{B} dV^{t+\Delta t} \right] \Delta \hat{\mathbf{u}}^{t+\Delta t} &= \sum_m \int_{V^{t+\Delta t}} \mathbf{H}^T \Delta \mathbf{f}^{\mathbf{B}, t+\Delta t} dV^{t+\Delta t} \\ &+ \sum_m \int_{S^{t+\Delta t}} \mathbf{H}^T \Delta \mathbf{f}^{\mathbf{S}, t+\Delta t} dS^{t+\Delta t} + \Delta \mathbf{R}_C^{t+\Delta t} \end{aligned} \quad (2.4.9)$$

The sum operator in this notation denotes that the equation has to be fulfilled for all m elements of the system in each integration point. After numerical integration, mostly Gauss integration, equation 2.4.9 is reformulated by assembling of the global stiffness matrix \mathbf{K} over all elements. Equation 2.4.10 results.

$$\mathbf{K}(\hat{\mathbf{u}}^{t+\Delta t}) \Delta \hat{\mathbf{u}}^{t+\Delta t} = \Delta \mathbf{F}^{t+\Delta t} \quad (2.4.10)$$

The solution of equation 2.4.10 can be found implicitly in an iterative numerical scheme in case of a nonlinear problem. The most basic method to do this is the Newton Raphson method that linearizes the system, finds a solution to the linear system using a linear matrix solver and then repeats this procedure until a convergence criterion is fulfilled.

In contrast to this iterative implicit solution procedure described in this section, an explicit time stepping procedure exists that is suitable for dynamic problems (unlike equation 2.4.2). For the quasi-static problems dealt within this study this explicit procedure is not suitable without mass-scaling and will not be used. For a dynamic FE-formulation the reader is referred to (Bathe, 2006).

2.4.3 Critical aspects of discretization

Setting up a FE simulation in a modern commercial FE software, several points have to be fulfilled to achieve an accurate approximation of the continuous system's behavior.

First, the increment time step between two successive solutions of the nodal force balance equation is of major importance. Unlike in explicit simulations, where there is an analytical formulation for the critical time step, in nonlinear implicit FE simulations there is no analytical formulation for the critical time step. To find it a convergence analysis can be performed.

Second, the elements have to be chosen such that the relevant geometries can be described without significant errors. This can either be guaranteed through a sufficient number of elements with linear functions H or through a lower number of elements of higher order functions H . Especially for cross rolling processes that have cylindrical workpieces this consideration is important. Only an infinite number of linear elements would be able to represent this shape without any error. Figure 9 left shows a cylindrical workpiece

meshed too coarsely, while Figure 9 middle shows a properly meshed workpiece.

Third, the same consideration holds for high gradients in result variables, such as stress or strains. Only a high number of elements with linear H functions (constant B functions) or a lower number of elements with higher order H functions (non-constant B functions) would be able to achieve satisfying results. With respect to fracture prediction in cross rolling operations both the core and the outer diameter show high gradients in result variables. For this reason they should be simulated with a sufficient number of small elements in order to guarantee correct stress and strain results. Figure 9 right shows the strain field over a cut section of a cross rolled bar. The high gradients over the workpiece are obvious.

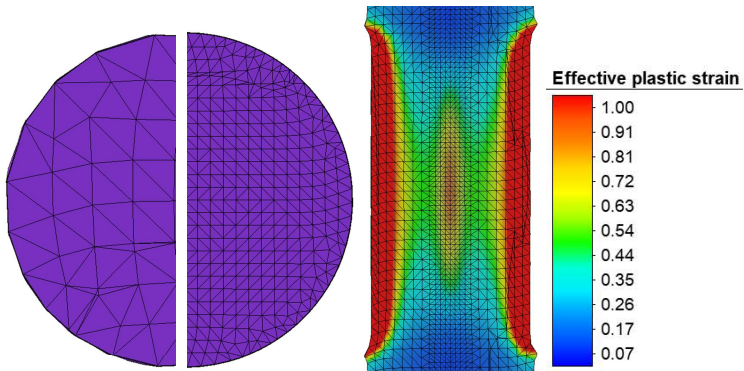


Figure 9: Left: Workpiece shape falsification by coarse element size, Middle: Correct mesh size, Right: High strain gradients over the workpiece

2.5 Ductile fracture modelling

After the pioneering studies of (McClintock, 1968) and (Rice & Tracey, 1969), many authors nowadays accept that the underlying mechanism of ductile fracture is first the nucleation of voids, which starts at inclusions, followed by void growth and finally coalescence of voids, which is imminent to complete fracture (see Figure 10) (Rousselier, 1987).

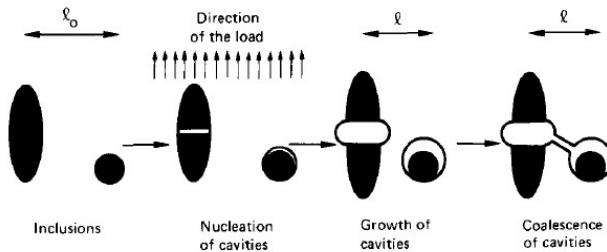


Figure 10 Mechanism of ductile fracture (Rousselier, 1987)

In contrast to brittle fracture surfaces, ductile fracture surfaces show the formed voids (see Figure 11). Ductile fracture is subsequent to material deformation. In case of ductile fracture of metals, fracture strains are usually high which often means that the stress state changes along the deformation path, making fracture prediction challenging.

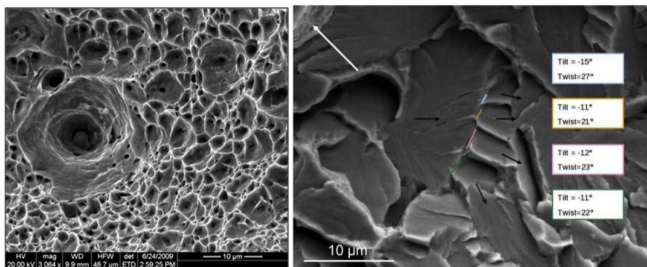


Figure 11: Left: Ductile fracture of steel, Right: Brittle fracture of steel (Pineau, Benzerga, & Pardoën, 2016)

The Mannesmann crack in the center of a cross rolled workpiece is embedded in solid material. For this reason necking doesn't occur prior to cracking under these circumstances as in many other bulk forming processes as well. That's why the fracture criteria evaluated and calibrated in this study, do not consider any necking phenomena. Instead, they try to explicitly quantify the material's fracture strains or stresses. This is a significant difference to sheet metal forming applications, where the well established forming limit curves (FLCs) quantify the beginning of localized necking. Figure 12 illustrates these two distinct possible deformation modes to ductile fracture.

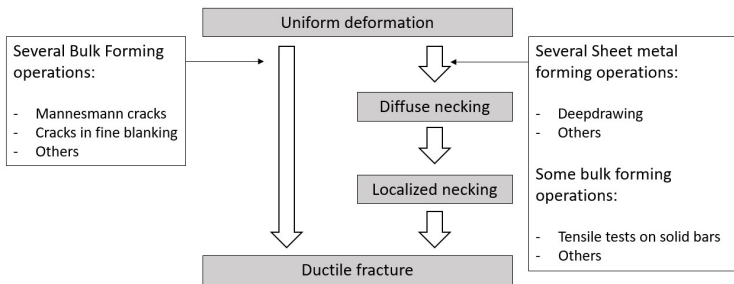


Figure 12: Possible deformation modes leading to ductile fracture

2.5.1 Parametrization of fracture criteria

A large variety of mathematical fracture criteria exists and their parametrizations often differ a lot. Although many criteria are formulated in terms of the quantities already introduced in chapters 2.1 to 2.3, many others are defined in terms of other stress measures that are typical for the formulation of ductile fracture criteria. These stress measures are defined in this section. Additionally, to be able to better compare the criteria parametrized differently, the conversion from one parametrization to another and vice-versa is explained here.

2.5.1.1 Modified Haigh Westergaard parametrization

A frequently used parametrization of the stress space makes use of the equivalent von Mises stress $\bar{\sigma}$, the dimensionless stress triaxiality η and the dimensionless normalized Lode angle parameter $\bar{\theta}$ to describe a material point's current stress state. Following Mohr's notations (Mohr & Marcadet, 2015) this parametrization will be referred to as the modified Haigh Westergaard coordinates $\{\bar{\sigma}, \eta, \bar{\theta}\}$. These coordinates are defined in this section.

Of major importance, especially with respect to ductile fracture is the dimensionless stress triaxiality η , defined as given by equation 2.5.1.

$$\eta = \frac{\sigma_h}{\bar{\sigma}} \quad (2.5.1)$$

Of growing importance in ductile fracture research is the Lode Parameter. The definition of the Lode Parameter is not unique, which is why a clear definition will be given here. A comparison between different formulations follows in chapter 2.5.1.4. The definition according to (Malvern, 1969) is also referred to as the normalized third deviatoric stress invariant ξ and $-1 \leq \xi \leq 1$.

$$\xi = \frac{27I_3(s)}{2\bar{\sigma}^3} = \frac{27(\sigma_1 - \sigma_h)(\sigma_2 - \sigma_h)(\sigma_3 - \sigma_h)}{2\bar{\sigma}^3} \quad (2.5.2)$$

The Lode angle θ is related to ξ as given in equation 2.5.3. The range of θ is given by $0 \leq \theta \leq \pi/3$.

$$\theta = \frac{1}{3} \arccos(\xi) \quad (2.5.3)$$

Since the range of possible values for θ is inconvenient and inconsistent with the value range of ξ , the normalized Lode angle parameter $\bar{\theta}$ was introduced. Its range of values is $-1 \leq \bar{\theta} \leq 1$.

$$\bar{\theta} = 1 - \frac{6}{\pi} \theta \quad (2.5.4)$$

$$\bar{\theta} = 1 - \frac{2}{\pi} \arccos(\xi) \quad (2.5.5)$$

Since the computation of $\bar{\theta}$ is inconvenient, a linear approximation is frequently used (equation 2.5.6). This formulation is equal to the negative of the original formulation of the ‘‘Lode-parameter’’ proposed by (Lode, 1926).

$$\bar{\theta} \cong - \left(2 \frac{\sigma_2 - \sigma_3}{\sigma_1 - \sigma_3} - 1 \right) \quad (2.5.6)$$

In different studies the plane stress state is of special importance. Firstly, since many experiments for calibration deliver plane stress data and secondly because many applications such as all stress states in thin sheet metal forming are plane stress states. While the definition of plane stress state in terms of principal stresses is trivial, this is not the case in the modified Haigh Westergaard space. The relation between η_{ps} and $\bar{\theta}_{ps}$ is given in equation 2.5.7 (Bai & Wierzbicki, 2008).

$$\bar{\theta}_{ps} = 1 - \frac{2}{\pi} \arccos \left(-\frac{27}{2} \eta_{ps} \left(\eta_{ps}^2 - \frac{1}{3} \right) \right) \quad (2.5.7)$$

2.5.1.2 Mixed stress strain parametrization

Another parametrization of stress and strain states is principally similar to the modified Haigh Westergaard coordinates $\{\bar{\sigma}, \eta, \bar{\theta}\}$. Following Mohr's notation (Mohr & Marcadet, 2015) in this study it is referred to as the mixed stress strain space $\{\bar{\varepsilon}, \eta, \bar{\theta}\}$ since it makes use of the equivalent strain $\bar{\varepsilon}$ instead of the equivalent stress $\bar{\sigma}$. These coordinates are especially common in ductile fracture research, where various recent fracture criteria are formulated in terms of these coordinates.

2.5.1.3 Conversion of different parametrizations

In order to be able to compare different fracture criteria formulated in terms of varying parametrizations it is useful to be able to transform them from one to another. For this reason the transformation equations between the different parametrizations are briefly outlined here.

To convert a parametrization from the mixed stress strain parametrization $\{\bar{\varepsilon}, \eta, \bar{\theta}\}$ to the parametrization of principal stresses $\{\sigma_1, \sigma_2, \sigma_3\}$ is straightforward. First, the parametrization is transformed into the modified Haigh Westergaard parametrization by the inverse of the hardening curve (equation 2.5.8).

$$\varepsilon_p = f^{-1}(\sigma_y) \quad (2.5.8)$$

Then one transforms the parametrization into the state of principal stresses $\{\sigma_1, \sigma_2, \sigma_3\}$ by using the given equations from chapters 2.5.1.1 and 2.2.

Converting parametrizations in the opposite direction, namely from the principal stress coordinates $\{\sigma_1, \sigma_2, \sigma_3\}$ to the mixed stress strain formulation $\{\bar{\varepsilon}, \eta, \bar{\theta}\}$ is slightly more demanding. Firstly, the principal stresses are eliminated by expressions of $\sigma_{1,2,3} = f(\bar{\sigma}, \eta, \bar{\theta})$. (Bai &

Wierzbicki, 2015) and (Mohr & Marcadet, 2015) give analytical solutions to this problem (equations 2.5.9 - 2.5.11).

$$\sigma_1 = \left[\eta + \frac{2}{3} \cos\left(\frac{\pi}{6}(1 - \bar{\theta})\right) \right] \bar{\sigma} \quad (2.5.9)$$

$$\sigma_2 = \left[\eta + \frac{2}{3} \cos\left(\frac{\pi}{6}(3 + \bar{\theta})\right) \right] \bar{\sigma} \quad (2.5.10)$$

$$\sigma_3 = \left[\eta + \frac{2}{3} \cos\left(\frac{\pi}{6}(7 + \bar{\theta})\right) \right] \bar{\sigma} \quad (2.5.11)$$

Then the effective stress is substituted by the equivalent plastic strain using the hardening curve formulation (see chapter 2.3.1). For calculation examples, see (Bai & Wierzbicki, 2010) and (Mohr & Marcadet, 2015) who have converted Mohr-Coulomb-type of fracture models into the mixed stress strain space, whereas (Bai & Wierzbicki, 2015) has converted numerous ductile fracture criteria into this space for comparison.

2.5.1.4 On varying Lode parameter definitions

In order to clarify the relations and differences between the different definitions of Lode parameters, they were calculated for variable σ_2 and the results compared as shown in Figure 13, where 0 on the horizontal axis means $\sigma_2 = \sigma_3$ and +1 on the horizontal axis means $\sigma_2 = \sigma_1$.

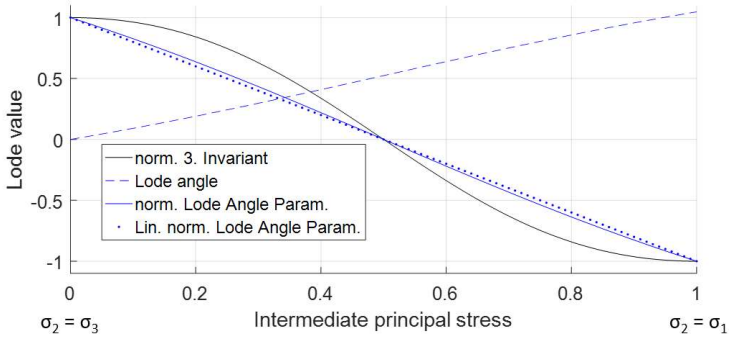


Figure 13: Comparison of different Lode parameter definition

It is found that the normalized third invariant ξ (equation 2.5.2) deviates by a maximum of roughly 0.2 from $\bar{\theta}$ (equation 2.5.5) for $\bar{\theta} \approx \pm 0.65$. This difference should not be neglected and can distort the shape of fracture criteria in the mixed stress strain space. The linearization of the normalized Lode angle parameter (equation 2.5.6), in contrast, deviates from its non-linearized formulation by a maximum of less than 0.04 $\bar{\theta} \approx \pm 0.65$. For this reason this approximation is reasonable in order to reduce computational complexity.

While in earlier studies (Wierzbicki et al., 2005) on the effect of the Lode parameter on ductile fracture it was common to use ξ as “Lode Parameter”, nowadays most studies (Mohr & Marcadet, 2015) are using the normalized Lode angle parameter $\bar{\theta}$. This study will align with recent research and use the normalized Lode angle parameter $\bar{\theta}$ as “Lode parameter”.

2.5.2 Classification and overview

There is an abundance of different ductile fracture criteria. For a list of available criteria including a chronological overview, the reader is referred to (Wesner, 2017). In this study in contrast, only the criteria most relevant for this study are introduced. Special focus is given to the most recent studies in selecting the relevant criteria for investigation of their accuracy in cross rolling operations. This study is clearly focusing on fracture criteria based on a macroscopic continuum mechanics approach. Nevertheless, in this section also the microscopic approach is briefly outlined.

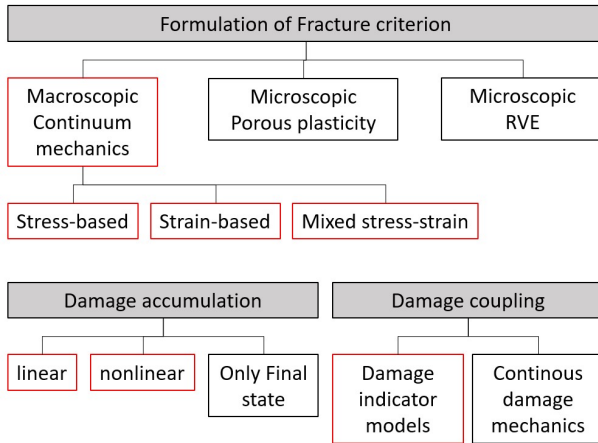


Figure 14: Differentiating factors and classes of ductile fracture criteria. Red: Focus of this study

Figure 14 illustrates the different categories of ductile fracture criteria with the differentiating categories being grey. There are various approaches how to model the underlying fracture phenomenon. While some models model the pore and its growth and coalescence (microscopic approach), others only model the phenomenon on a macroscopic level, using the particles' stress and strain state variables. Again others model even the microstructure on a basis of

representative volume elements (RVE). The available models also differ with respect to the coupling between constitutive relations and damage. While damage indicator models do not couple damage with constitutive relations, the continuum damage mechanics models reduce the material's stiffness with increasing damage. Another major difference is how the damage is accumulated. While some models do it in a linear way, others use nonlinear accumulation rules and again others don't accumulate damage but only consider the final state. In chapters 2.5.4 to 2.5.9 the different classes of ductile fracture criteria are introduced and their concepts explained.

Another way to classify fracture criteria is based on their derivation and underlying assumptions (see Figure 15). Purely phenomenological criteria base their modelling approach on experimental results that they are trying to approximate as accurately as possible. In contrast, physically motivated models base their modelling approach on a logically justifiable assumption, eg. maximum critical shear stress, maximum plastic deformation energy to fracture or pore volume growth. Other criteria base their failure prediction on a complete mathematical set of differential equations to assess stability, eg. (de Borst & Verhoosel, 2018), which is beyond the scope of this work.

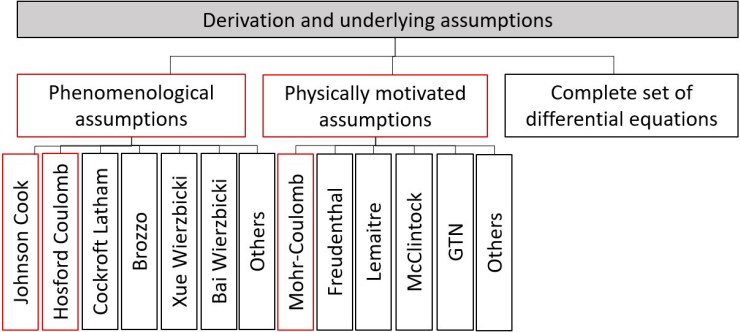


Figure 15: Classes of fracture criteria with respect to derivation. Red: Focus of this study

2.5.3 Focus of this study

This study is clearly focusing on macroscopic fracture criteria. With respect to damage, this study will treat damage as a pure indicator variable, meaning that there will be no coupling between damage and material properties, such as elasticity or density. For this reason, damage will not affect acting stresses in all calculations from chapter 3 onwards. This approach appears sufficient, since the achieved results are of very good accuracy (see chapter 5). Under these premises the following definitions are used from chapter 3 on:

- **Fracture:** Local material separation of a size of at least $50\mu\text{m}$ (equals 5-10 grain sizes for the investigated steel). Both material separation with and without subsequent structural instability is considered as fracture. This definition implies that fracture can occur purely internally without complete separation of the whole sample into several pieces.
- **Crack:** Equivalent to fracture.
- **Failure:** Equivalent to fracture.
- **Damage:** Purely mathematical indicator variable to assess the onset of ductile fracture. No coupling to actual material behavior is assumed. At a damage of 100%, immediate fracture is predicted to occur.

Although only macroscopic damage criteria and uncoupled damage models will be used from chapter 3 onwards, for the sake of completeness also microscopic fracture criteria (chapter 2.5.9) and the concept of coupled damage mechanics (chapter 2.5.8) will be shortly introduced later.

2.5.4 Stress based macroscopic criteria

Macroscopic fracture criteria do not model the void formation explicitly, but assume that this can be done implicitly by macroscopic measures. These criteria are formulated in terms of stress, strain or combined stress strain measures. In many cases a classification is not unique, since all the criteria can be transformed from stress to strain space and vice-versa. The continuum mechanics approach is the oldest approach to material fracture with Coulomb having described his limit stress criterion in 1776 already (Coulomb, 1776).

Mohr (Mohr, 1914) assumed that failure depends only on σ_1 and σ_3 and the critical relationship between σ_n and τ can be linear or nonlinear. Coulomb's criterion (Coulomb, 1776) in contrast assumed a linear failure envelope. Coulomb formulated it as given in equation 2.5.12, when compressive stresses are defined as negative:

$$|\tau| = S_0 - \sigma_n \tan(\phi) = c_2 - c_1 \sigma_n \quad (2.5.12)$$

S_0 is the inherent shear strength, also known as cohesion coefficient and ϕ is the angle of internal friction. In order to express the criterion in terms of principal stresses Figure 16 gives the Mohr-Coulomb criterion in conjunction with a material particle's Mohr's stress circle that has just reached the critical fracture state. This is given through the fact that the Mohr's circle just touches the critical fracture line.

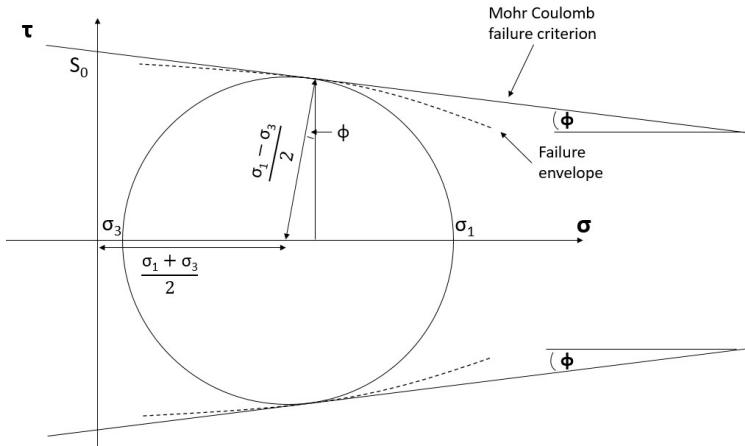


Figure 16: The Mohr Coulomb fracture criterion in space of normal and shear stresses

Trigonometric considerations from Figure 16 give relations for shear and normal stress on an arbitrary cutting plane:

$$\tau = \cos(\phi) \frac{\sigma_1 - \sigma_3}{2} \quad (2.5.13)$$

$$\sigma_n = \frac{\sigma_1 + \sigma_3}{2} + \sin(\phi) \frac{\sigma_1 - \sigma_3}{2} \quad (2.5.14)$$

Inserting these relations into the Mohr Coulomb criterion (equation 2.5.12), which is equivalent to assuming that fracture is just about to occur and simplifying yields:

$$(\sigma_1 - \sigma_3) + \sin(\phi) (\sigma_1 + \sigma_3) = 2S_0 \cos(\phi) \quad (2.5.15)$$

Noting that ϕ is constant in the linear Mohr Coulomb criterion and adapting the constants of the model for simplification purposes the criterion can be written as follows, which is fully equivalent to equation 2.5.12.

$$(\sigma_1 - \sigma_3) + c(\sigma_1 + \sigma_3) = b \quad (2.5.16)$$

$$c = \frac{c_1}{\sqrt{1 + c_1^2}} \quad (2.5.17)$$

$$b = \frac{2c_2}{\sqrt{1 + c_1^2}} \quad (2.5.18)$$

Although the linear assumption is simplifying especially for strong multiaxial tension, the Mohr- Coulomb criterion is the most widely used stress based fracture criterion. It has been used to predict fracture in rock and soil mechanics for many years. The application to ductile fracture in contrast is less established. In recent years several publications have drawn attention to Mohr-Coulomb type criteria for ductile fracture prediction (Bai & Wierzbiki, 2010), (Dunand & Mohr, 2014), (Mohr & Marcadet, 2015).

Different variations of the Mohr Coulomb model have been published recently. (Mohr & Marcadet, 2015) proposed an extension of the Mohr Coulomb fracture criterion, called the Hosford-Coulomb criterion. They reformulated the fracture criterion itself using the Hershey Hosford yield stress (equation 2.3.13) instead of the maximum shear stress.

$$\max_n [\sigma_{HF} + c_1 \sigma_n] = c_2 \quad (2.5.19)$$

2.5.5 Strain based macroscopic criteria

Purely strain based fracture criteria are rarely used in bulk metal forming, while they are frequently employed in sheet metal forming. Here, forming limit diagrams give a relationship between the first principal strain and the maximum second principal strain before localized necking occurs. In this study purely strain based criteria will not be used.

2.5.6 Mixed stress- strain based macroscopic criteria

A simple, very basic mixed stress-strain criterion was developed by (Freudenthal, 1950) assuming that fracture occurs at a critical value of deformation energy C . In contrast to the aforementioned criteria this criterion incorporates the deformation history by accumulating plastic energy through its integral formulation.

$$C = \int_0^{\varepsilon_f} \bar{\sigma} \, d\bar{\varepsilon} \quad (2.5.20)$$

A major drawback of this model is that it does not distinguish between compressive and tensile deformations. For this reason (Cockroft & Latham, 1968) formulated a model that accumulates damage by integrating the first principal stress over the equivalent plastic strain.

$$D_{Cockroft} = \int_0^{\varepsilon_f} \sigma^* \, d\bar{\varepsilon} \quad (2.5.21)$$

$$\sigma^* = 0 \text{ if } \sigma_1 < 0$$

$$\sigma^* = \sigma_1 \text{ if } \sigma_1 > 0$$

(Brozzo, Deluca, & Rendina, 1972) modified the model by normalizing the first principal stress by the stress deviator.

$$D_{Brozzo} = \frac{2}{3} \int_0^{\varepsilon_f} \frac{\sigma_1}{(\sigma_1 - \sigma_h)} \, d\bar{\varepsilon} \quad (2.5.22)$$

A frequently used model is the one proposed by (Johnson & Cook, 1985). It explicitly contains the stress triaxiality and assumes an exponential decay of ductility with respect to stress triaxiality. Also strain rate and temperature influences are included. A linear damage accumulation is assumed (see chapter 2.5.7) and a damage indicator D used.

$$\varepsilon_f = (C_1 + C_2 \exp(C_3 \eta)) \left(1 + C_4 \ln \left(\frac{\dot{\varepsilon}}{\dot{\varepsilon}_0} \right) \right) \left(1 + C_5 \frac{T}{T_0} \right) \quad (2.5.23)$$

(Bao & Wierzbicki, 2005) postulated the existence of a cutoff stress triaxiality of $\eta = -0.333$, below which fracture will never occur, meaning $\varepsilon_f \rightarrow \infty$.

(Wierzbicki & Xue, 2005) noted that stress triaxiality is not sufficient to accurately describe the material's ductility based on Bao's extensive experimental program on Aluminum (Wierzbicki et al., 2005). For this reason they included the normalized third invariant in their model. They assumed that the dependency of fracture strain on the normalized third invariant ξ can be described by a family of elliptic functions. In their work, Xue and Wierzbicki made use of the normalized third invariant ξ instead of the normalized Lode angle parameter $\bar{\theta}$ that is used in more recent research. As shown in chapter 2.5.1.4 the differences between the two formulations are not neglectable, but the shape of the resulting fracture criteria in the mixed stress strain space is in principal similar. The resulting surfaces in the mixed stress strain space are symmetric with respect to $\bar{\theta} = 0$. A possible surface in that space is given in Figure 17. Note that the model is purely phenomenological.

$$\varepsilon_f = C_1 \exp(-C_2 \eta) - (C_1 \exp(-C_2 \eta) - C_3 \exp(-C_4 \eta)) \left(1 - \xi^{\frac{1}{n}}\right)^n \quad (2.5.24)$$

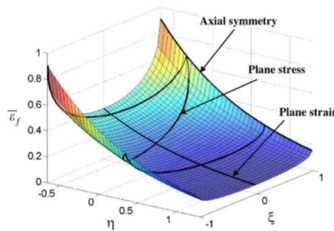


Figure 17: Xue-Wierzbicki fracture criterion in the mixed stress-strain space (Wierzbicki et al., 2005)

(Bai & Wierzbicki, 2008) postulated a new phenomenological 3D fracture locus in the mixed stress strain space $\{\bar{\varepsilon}, \eta, \bar{\theta}\}$. In contrast to

the Xue-Wierzbicki model, the Bai-Wierzbicki model is generally asymmetric with respect to $\bar{\theta} = 0$.

$$\varepsilon_f = \left[\frac{1}{2} (D_1 e^{-D_2 \eta} + D_5 e^{-D_6 \eta}) - D_3 e^{-D_4 \eta} \right] \bar{\theta}^2 + \frac{1}{2} (D_1 e^{-D_2 \eta} - D_5 e^{-D_6 \eta}) \bar{\theta} + D_3 e^{-D_4 \eta} \quad (2.5.25)$$

(Bai & Wierzbicki, 2010) transformed the physically motivated and reasonable Mohr-Coulomb stress model into the mixed stress strain space $\{\bar{\varepsilon}, \eta, \bar{\theta}\}$ (equation 2.5.26) using the coordinate transformations described in chapter 2.5.1.3 assuming a Hollomon hardening curve approximation. They showed that the resulting 3D fracture locus has strong similarity with the asymmetric Bai-Wierzbicki fracture locus (equation 2.5.25).

$$\varepsilon_f = \left[\frac{A}{c_2} \left[\sqrt{\frac{1 + c_1^2}{3}} \cos\left(\frac{\bar{\theta}\pi}{6}\right) + c_1 \left[\eta + \frac{1}{3} \sin\left(\frac{\bar{\theta}\pi}{6}\right) \right] \right] \right]^{\frac{1}{n}} \quad (2.5.26)$$

(Dunand & Mohr, 2014) subjected a unit cell with a central void to more than 160 combinations of shear and normal loading to determine the macroscopic plastic strain at the onset of localization. Their results demonstrated that the shape of the MC fracture criterion in the mixed stress strain space given by equation 2.5.26 is a suitable fracture criterion, assuming that secondary localization is imminent to fracture.

(Bai & Wierzbicki, 2008) came up with an adaption of the MC model, the so-called extended Mohr-Coulomb criterion applicable to ductile fracture. They proposed a stress triaxiality and Lode angle parameter dependent hardening rule, which is equivalent to varying the shape of the yield locus. By this variation of the yield locus, the shape of the extended Mohr Coulomb criterion in the mixed stress-strain space can be varied. To account for non-monotonic loading conditions, they used a linear damage accumulation rule (see chapter 2.5.7) and a damage indicator D .

2.5.7 Damage accumulation rules

When deformation happens under constant stress state, the current material damage can be accumulated according to equation 2.5.27.

$$D = \left(\frac{\varepsilon}{\varepsilon_f} \right)^n \quad (2.5.27)$$

In order to account for changing stress states during deformation, one way to incorporate the material's deformation history is by accumulating a damage indicator variable D . In case of the assumption of a linear accumulation rule ($n=1$) as in the Johnson Cook (Johnson & Cook, 1985) failure model this relation is formulated by equation 2.5.28. Equation 2.5.29 is a generalized form of equation 2.5.28, that allows for accumulating damage nonlinearly as applied by (Xue, 2007) and (Neukamm, Feucht, & Haufe, 2008). Damage should occur when the damage value D reaches 100%.

$$D = \int \frac{d\varepsilon}{\varepsilon_f(\eta, \theta)} \quad (2.5.28)$$

$$D = \int \frac{n}{\varepsilon_f(\eta, \theta)} D^{\frac{n-1}{n}} d\varepsilon \quad (2.5.29)$$

The underlying assumption for nonlinear damage accumulation is that the deformation increment gets a higher weighting factor the closer it is to fracture. Damage then grows slowly in the beginning of the forming process and fast towards the end (Figure 18).

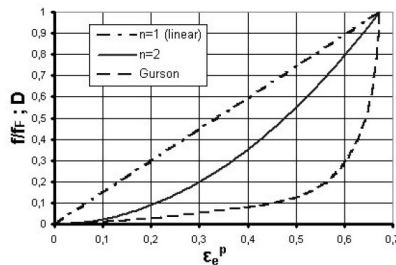


Figure 18: Linear and nonlinear damage accumulation (Neukamm, Feucht, & Haufe, 2008)

2.5.8 Continuum damage mechanics

The continuum damage mechanics (CDM) approach redefines the effective surface \tilde{S} based on the assumption that the existing damaged surface S_D has to be subtracted from the initial undamaged surface S (Rabotnov, 1963), (Lemaitre, 1984). Figure 19 illustrates the underlying assumption.

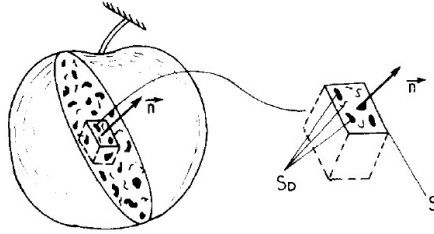


Figure 19: Concept of effective surfaces (Lemaitre, 1984)

The effective surface \tilde{S} is defined as given by equation 2.5.30. The corresponding damage can be calculated from the remaining effective surface as given by equation 2.5.31.

$$\tilde{S} = S - S_D \quad (2.5.30)$$

$$D = \frac{S - \tilde{S}}{S} \quad (2.5.31)$$

Having reduced the surface on which the force is acting, the acting effective stresses $\tilde{\sigma}$ on the remaining surface are higher than without this correction.

$$\tilde{\sigma} = \frac{\sigma}{1 - D} \quad (2.5.32)$$

Like this, the damage variable D is coupled to the constitutive relations and affects the acting stresses in the material in this approach to ductile fracture. This assumption is in contrast to the damage indicator approach and will not be used in this study as explained in chapter 2.5.3.

2.5.9 Microscopic criteria- porous plasticity

An approach that goes further into the micromechanics than the CDM approach are fracture criteria based on porous plasticity. They attempt to model porosity in a solid material matrix in order to determine the onset of fracture. These models aim at modeling the behavior of solids with isotropic distributions of porosity. The first model of porous plasticity was developed by (McClintock, Kaplan, & Berg, 1966), who modeled pore growth of cylindrical pores in an infinitely long matrix material.

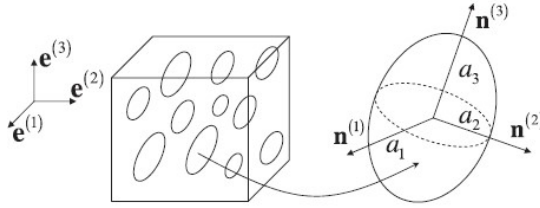


Figure 20: Porous volume element (Danas & Aravas, 2012)

The probably most popular model of that kind is the Gurson-model (Gurson, 1977), that followed earlier work by (Rice & Tracey, 1969). The Gurson model uses an exact solution for a unit cell with spherical or cylindrical cavity under hydrostatic loadings. Gurson uses the pore volume fraction f as a major state variable in his model. It is defined by equation 2.5.33. The void volume fraction's evolution is governed by nucleation and growth of voids (equations 2.5.34 to 2.5.36).

$$f = \frac{V_{Pores}}{V_{Total}} \quad (2.5.33)$$

$$df = df_{nucl} + df_{growth} \quad (2.5.34)$$

$$df_{nucl} = C(1 - f)d\bar{\epsilon} \quad (2.5.35)$$

$$df_{growth} = (1 - f)d\epsilon_v \quad (2.5.36)$$

In order to determine whether plastic flow occurs the flow potential Φ is used (equation 2.5.37). It depends on the macroscopic stress Σ and on the microscopic stress σ , as well as the current void volume fraction f . This clearly shows the coupling between damage and plastic flow.

$$\Phi = \frac{\bar{\Sigma}^2}{\sigma_y^2} + 2f \cosh\left(\frac{3\Sigma_H}{2\sigma_y}\right) - 1 - f^2 \quad (2.5.37)$$

The Gurson model was later extended for effects of void nucleation, corrected void growth and void coalescence effects and then referred to as Gurson-Tvergaard-Needleman model (GTN model). The most commonly criticized drawback of this GTN model is that fracture would never occur under pure shear. For this reason (Nahshon & Hutchinson, 2008) then extended the GTN model again to capture shear fracture modes.

Even the not shear-extended GTN model has eleven parameters to be calibrated. From an industrial point of view the application is questionable due to a high calibration effort and the question of transferability of results from one process to another. There are also authors questioning porous plasticity and fracture models in general, such as (Coppola, Iob, & Campanelli, 2014). In their studies, they conducted tensile and torsion experiments on nine different standard steels until fracture. Afterwards they cut the fractured specimens open and polished the surfaces. Taking micrographs, they measured the void volume fraction at virgin material elements, as well as right next to the fractured area and in between. Their finding is that the void volume fraction right next to fracture is “fully negligible” and that there is no correlation between void volume fraction and plastic strain. This raises the question of reasonability of both porous plasticity and porous fracture models. Due to these drawbacks, this study is focusing on macroscopic fracture criteria.

2.5.10 Experimental methods for calibration

In sheet metal forming there is a more or less standardized procedure for the investigation of forming limit curves given by the Nakazima test. (Gorji Bandpay, 2015) furthermore listed the uniaxial tensile test, the hydraulic bulge test, the Hecker test and the Marciniak test and possible experimental methods for the determination of strain limits for sheet metal forming.

All the mentioned experimental methods are making use of sheet metal raw material. To investigate the fracture behavior of bulk metal material, the procedures are less standardized than for sheet metal. In this section, the most important approaches for the calibration of ductile bulk fracture criteria will be summarized.

Many experimental studies were conducted using pre-notched or unnotched round tensile steel bars (Hancock & Mackenzie, 1976). Deforming the specimen in tensile state, the works were missing data points for lower stress triaxiality levels. For this reason different authors (Johnson & Cook, 1985) additionally used torsion tests for the investigation of fracture behavior at low stress triaxiality. While Johnson and Cook used solid specimens in their torsion experiments under pure torsion, other authors ((Gao et al., 2011), (Barsoum & Faleskog, 2007)) varied both geometry of the testing specimen and the stress state in their torsion experiments. (Barsoum & Faleskog, 2007) for example used a hollow double notched torsion specimen and superimposed a varying tensile stress component. By using a hollow double notched specimen they optimized the triaxiality and Lode angle parameter paths to fracture, as well as these parameters' homogeneity over the specimen's radius.

A recent series of studies conducted by (Wierzbicki et al., 2005) uses a variety of different sample geometries made from aluminum. The experimental geometries include round tensile bars, round tensile notched bars, flat grooved tensile specimens, upsetting specimens, shear specimens and flat tensile specimens (see Figure 21). By varying

the specimen geometry and load, they try to cause fracture under a variety of stress states (see Figure 22).

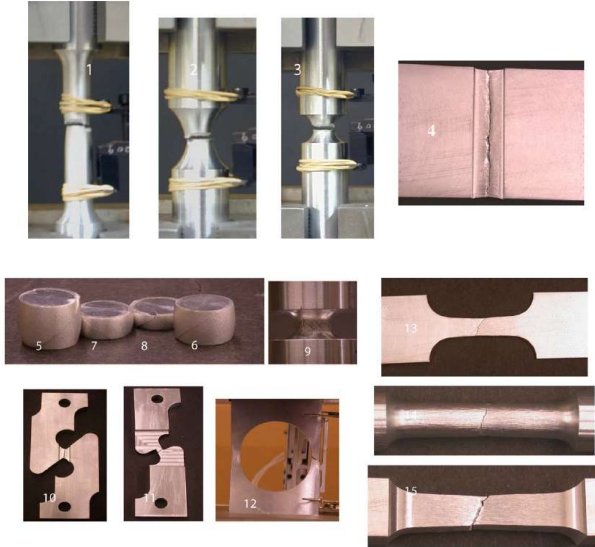


Figure 21: Sample shapes used by Wierzbicki's research group in order to characterize ductile fracture behavior (Wierzbicki et al., 2005)

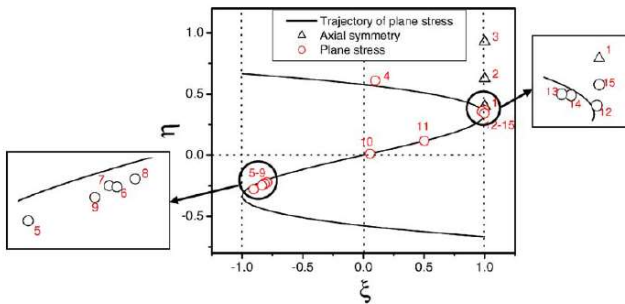


Figure 22: Averaged stress states reached by experimental program proposed by (Wierzbicki et al., 2005)

3 Cross rolling related material characterization

3.1 General considerations on the raw material

The material investigated in this work is a Manganese-Boron alloyed tempered heat treatable steel 20MnB4 produced according to (EN-10263-4, 2002). Table 2 gives its chemical composition. It is delivered as a wire (see Figure 46 left) produced by normalizing hot rolling. The material is typically known for its good cold formability, which makes it a common choice for bulk formed products. Products from 20MnB4 are frequently used for fastening technology applications (Noneder & Merklein, 2012).

%	C	Si	Mn	P	S	Cr	Cu	B
≥	0,17	-	0,7	-	-	-	-	0,0005
≤	0,24	0,4	1,2	0,035	0,035	0,3	0,3	0,005

Table 2: Chemical composition of the used material (EN-10263-4, 2002)

To investigate grain sizes, structures and possible previous deformation, metallographic micrographs (see Figure 23) were made. To do so, a material sample was polished and then etched for 10 seconds with a Nital solution (98% Ethanol, 2% Nitric Acid) at room temperature. The micrograph clearly shows the bright Ferrite grains in contrast to the dark Pearlite regions. At sufficient magnification, the Zementit lamellas can be identified in the pearlitic regions. Grain sizes are around 10 μ m, which makes it a fine grain steel. Deformations or texture could not be detected in the micrographs.

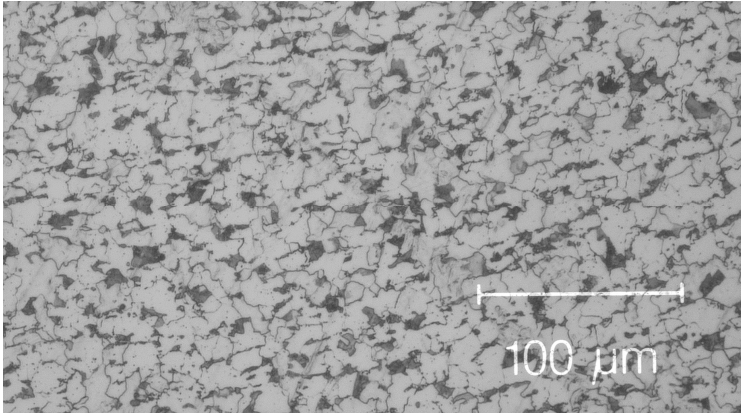


Figure 23: Metallographic micrograph of the used raw material 20MnB4

The raw material's production process is a hot normalizing wire rolling process, which according to (Gorni & Soares, 2015) and (voestalpineGrobblechGmbH, 2018) typically leads to a homogenized microstructure with a fine grain size that corresponds extensively to the properties in normalized annealed condition. Since this production process is carried out above recrystallization temperature, grains can ideally reform during rolling, eliminating possible textures, which gives a homogenized microstructure, as also visible in Figure 23.

3.2 Characterization demands of cross rolling processes

Material data acquisition is a crucial point to ensure correct results from numerical simulations. Depending upon the type of process to be modelled, different material data has to be experimentally investigated and modelled.

While in sheet metal forming the use of anisotropic yield loci is standard, this is not the case for bulk metal forming processes like the cross rolling process where typically isotropic *von-Mises type yield loci* (equation 2.2.12) are used. Due to the normalizing production

process of the used raw material and the texture-free micrographs from the previous chapter the assumption of a von-Mises yield locus will be used for the given material.

Typical process characteristics of cross rolling operations are:

- Very large strains reached in compressed areas
- High strain rates
- Temperature increase over the process
- Cyclicity of the process

To be precise, therefore the material's *hardening behavior* should be modeled as temperature- and strain rate dependent. Furthermore the correctness of the large strain hardening behavior has to be enforced.

Since the process is cyclic, the question whether a purely isotropic hardening assumption can describe the material's hardening behavior correctly, should be answered. This will be done by assessing the correctness of simulated process forces and torques using a purely isotropic von Mises yield locus. If the accuracy is not sufficient, then the hardening behavior has to be modeled as a superposition of *kinematic hardening* and isotropic hardening. To calibrate these models, cyclic tension-compression or cyclic torsion tests would be needed.

The overall goal of this study is the prediction of core fracture initiation. As a consequence, an important part of the material data acquisition is the investigation of the material's *fracture behavior*. Since the stress state in the workpiece core highly depends on tool geometry in cross rolling operations, the fracture behavior over a wide range of stress states is relevant and should be captured by the fracture modeling. Again, because of the characteristics of cross rolling operations, the temperature- and strain rate dependency of the material's fracture behavior is relevant.

In the upcoming subchapters the material's hardening- and fracture behavior will be experimentally investigated and mathematically described with special attention on the demands of the cross rolling process described in this subchapter.

3.3 Hardening behavior of 20MnB4

3.3.1 Methodology

Since in tensile tests the material's hardening behavior can only be measured up to the end of uniform elongation (strain of 14% for 20MnB4), the hardening behavior was mainly measured in dilatometer compression tests on a TA Instruments Dilatometer 805A/D. This reduces extrapolation uncertainty with respect to stresses at higher strains. With these compression experiments, stress values for higher strains of up to 40% were investigated experimentally. Experiments were performed at varying temperatures and strain rates.

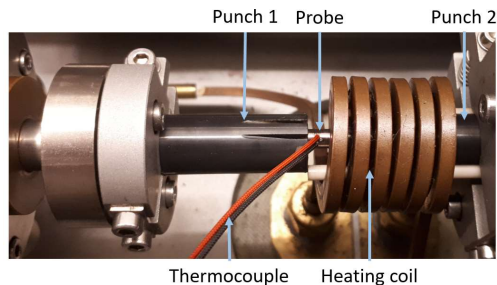


Figure 24: Experimental setup in dilatometer compression experiments

Figure 24 gives the experimental setup, where the probe is moved out of the heating coil for better visibility. During deformation, a type S thermocouple spot welded to the probe measured the current temperature which was then used to control the inductive heating coil's power. Appendix 1 gives the geometry of the used compression probes.

3.3.2 Friction compensation

Evaluating the experiments, a probe barreling can be observed (see Figure 25). It is well known (Hochholdinger, Hora, & Wegener, 2012) that this barreling is caused by friction effects between the probe and the punches. The bigger the barreling, the further the stress state deviates from uniaxial compression. For this reason the barreling should be minimized if possible. To achieve this, a molybdenum sulfide lubricant (MOLYKOTE HSC Plus) was applied on both sides of the probe.



Figure 25: Left: Undeformed compressive probe, middle: Ideal deformation, no friction, right: deformed probe with friction

To eliminate the influence of the remaining friction effects on the measured experimental stress strain relationship, the following analytical approximation for the frictional correction of the flow stress according to equation 3.3.2 was used (Siebel & Pomp, 1927). This relation is a first order Taylor approximation of a more complex relation (Han, 2002) valid if $\mu d/h < 0.35$, which is the case in this work.

$$\sigma_y \cong \frac{F(\varepsilon)}{\pi r(\varepsilon)^2} \frac{1}{\left[1 + \frac{2\mu r(\varepsilon)}{3h(\varepsilon)}\right]} \quad (3.3.1)$$

Inserting $r(\varepsilon)$ and $h(\varepsilon)$:

$$\sigma_y \cong \frac{F(\varepsilon)}{\pi r(\varepsilon)^2} \frac{1}{\left[1 + \frac{2\mu r_0 \exp(1.5|\varepsilon|)}{3h_0}\right]} \quad (3.3.2)$$

To evaluate the equation, the friction coefficient μ is needed. It has been approximated by a combined simulative-experimental procedure:

- 1) The barreling of the probe has been measured.
- 2) The experiment has been simulated with $n=20$ varying friction coefficients ($0.05 < \mu_i < 0.25$)
- 3) The friction coefficient μ was chosen according to equation 3.3.3:

$$\min_{1 < i < n} \{ |Barreling_{Exp} - Barreling_{Sim,i}| \} \quad (3.3.3)$$

This procedure lead to a friction coefficient of $\mu=0.08$, which was used for the flow stress correction according to equation 3.3.2 in the upcoming dilatometer compression results.

Validation of friction compensation

To verify this evaluation procedure, a tensile test (technical drawing of used probe in Appendix 2) has been performed at a temperature of 160°C and a strain rate of $\dot{\varepsilon} = 0.1/s$. The stress-strain curve from the frictionless tensile test was compared to the friction-corrected (equation 3.3.2: $\mu=0.08$) and uncorrected (equation 3.3.2: $\mu=0.0$) stress strain curves from compression tests at the same temperature and strain rate. A very good agreement of the friction-corrected stress strain curve with the tensile test- curve was found, while the deviation of the uncorrected compressive curve was obvious (see Figure 26).

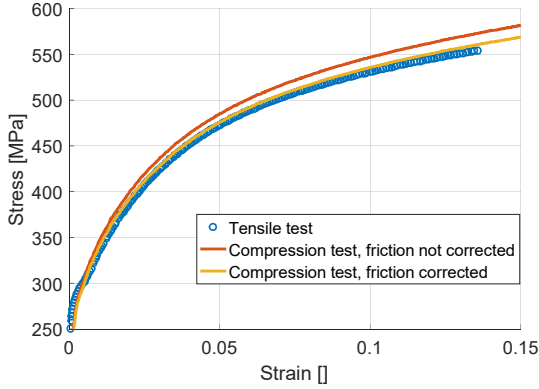


Figure 26: Comparison of stress-strain relations of compressive tests with and without friction-correction ($T=160^{\circ}\text{C}$, $\dot{\varepsilon} = 0.1/\text{s}$) with tensile test

3.3.3 Results and mathematical approximation

The parameter identification of different flow curve approximations has been performed by finding the solution to the least square problem given in equation 3.3.4. An additional constraint has been enforced that demands that the slope in one of the last experimentally measured points in the stress strain relationship (at $\varepsilon=40\%$) has to equal the slope of the mathematical approximation at that point (equation 3.3.5). This constraint ensures a better agreement of the stress strain relation for very large extrapolated strain values (see Figure 27).

$$\min \left\{ \sum_i (\sigma_{fit}^i - \sigma_{meas}^i)^2 \right\} \quad (3.3.4)$$

$$\left. \frac{d\sigma_{fit}}{d\varepsilon_{fit}} \right|_{\varepsilon=40\%} = \left. \frac{d\sigma_{meas}}{d\varepsilon_{meas}} \right|_{\varepsilon=40\%} \quad (3.3.5)$$

A saturating extended Hockett-Sherby flow curve formulation (equation 2.3.10) and a non-saturating Hensel-Spittel flow curve formulation (equation 2.3.7) were chosen to be fitted to the experimental data. Because the Hensel Spittel flow curve is not formulated in terms of $Rp_{0,2}$ it tends to underestimate stresses at very low strains. For this reason only stresses at strains higher than 1% were used for the Hensel Spittel parameter identification. This procedure is expected to lead to negligible errors since cross rolling operations lead to very large strains far higher than 100%. In case of a Hensel Spittel hardening curve approximation the needed derivation of the hardening curve with respect to the strain is given by equation 3.3.6, in case of an extended Hockett Sherby approximation by equation 3.3.7:

$$\frac{d\sigma_{fit}}{d\varepsilon_{fit}} = A e^{m_1 T \frac{1}{[K]}} (\dot{\varepsilon}[s])^{m_2} \left[n \varepsilon^{n-1} \exp\left(\frac{C}{\varepsilon}\right) - C \varepsilon^{n-2} \exp\left(\frac{C}{\varepsilon}\right) \right] \quad (3.3.6)$$

$$\frac{d\sigma_{fit}}{d\varepsilon_{fit}} = (\sigma_{sat} - C_1) e^{m_1 T \frac{1}{[K]}} (\dot{\varepsilon}[s])^{m_2} \exp(-c_2 \varepsilon^n) c_2 n \varepsilon^{n-1} \quad (3.3.7)$$

Due to the nature of the listed constraint (equation 3.3.5) it cannot be enforced for an arbitrary number of experimental stress-strain curves. For this reason it is only enforced for the reference configuration ($T=90^\circ\text{C}$, $\dot{\varepsilon}=0.1/\text{s}$). The following two step parameter identification procedure has been employed:

1. Identification of the stress-strain relationship parameters for the reference configuration solving equation 3.3.4 under constraint from equation 3.3.5. The results after this step are illustrated in Figure 27. Identified parameters:
 - Hensel Spittel: n , A and C
 - Hockett Sherby: c_2 , n , C_1 and σ_{sat}

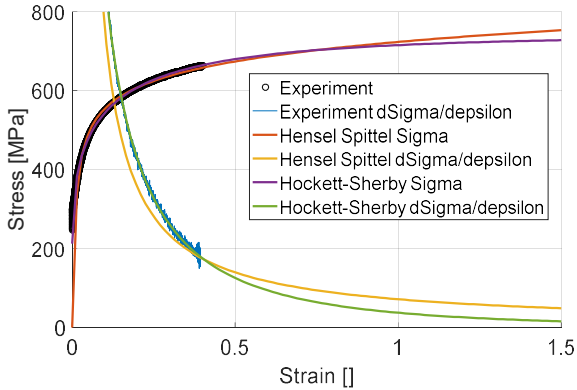


Figure 27: Experimental and approximated stress strain curves and their derivatives

2. Identification of the temperature- and strain rate dependency from all experimental data solving equation 3.3.4. All experiments used have been reduced to the same number of data points for the parameter identification, so that each experiment weighs the same. Identified parameters:
 - Hensel Spittel: m_1 and m_2
 - Hockett-Sherby: m_1 and m_2

Temperatures of 20°C, 90°C and 160°C were tested at a constant strain rate of 0.1/s. This strain rate has been chosen because it is the highest strain rate that did not lead to non-isothermal conditions.

Strain rates of 0.01/s, 0.1/s, 1/s and 10/s were tested at a constant increased temperature of 90°C. By performing these tests at an elevated temperature, the deformation induced heat generation of the probe could be partially compensated through the machine's temperature control by reducing the heating power. This leads to more isothermal conditions. The experiments under the high strain rates 1/s and 10/s were only used up to strains of 20% because for higher strains non-isothermal temperature increase became significant. Figure 28 shows the measured stress-strain relationships (friction-corrected) for different temperatures and strain rates, as well as the fitted

approximations. It is found that the different approximations reveal similar accuracy in approximating the measured data.

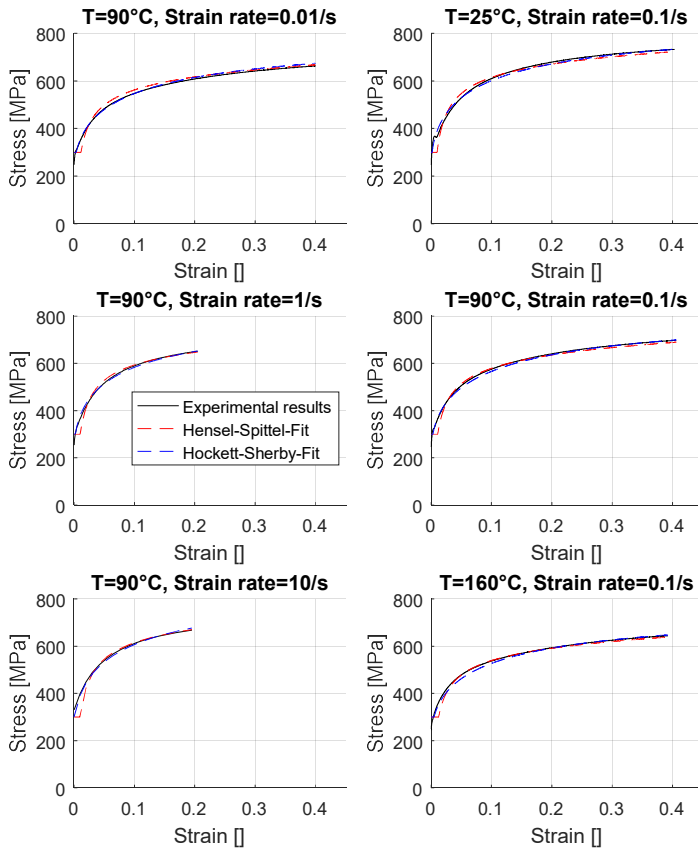


Figure 28: Experimental and approximated stress-strain relations for various temperatures and strain rates

The introduced parameter identification procedure ensures a correct slope in the last measured data point while at the same time being able to model strain rate and temperature dependence of the flow stress

correctly. Table 3 shows the identified flow curve coefficients. They are only valid when inserting the temperature in Kelvin [K].

Parameters Hensel Spittel					
A	n	C	m ₁	m ₂	
1146.6 MPa	0.0944	-0.0055	-0.001	0.013	

Parameters Hockett Sherby extended					
σ _{sat}	C ₁	n	c ₂	m ₁	m ₂
1182.7 MPa	313.4 MPa	0.4855	3.011	-0.001	0.013

Table 3: Identified parameters of hardening curve approximations for 20MnB4

3.3.3.1 Validation through torsion experiments

To verify the stress-strain relationships for high strain values that are dominant in cross rolling operations and to conclude which approximation is most accurate for high strain values, torsion tests were employed. The used specimen geometries are given in Appendix 3. These tests are frictionless and show no necking in contrast to tensile experiments, which qualifies them for the verification of the extrapolated stress-strain relationships. Furthermore, fracture strains under shear stresses are higher than under tensile stresses. On the other hand, it is well known (Pöhlandt, 2013) that plastic flow under shear often happens at lower equivalent von-Mises stresses than in uniaxial stress states (equation 3.3.8). In torsion tests, for this reason torque-angle curves are often found to be slightly lower than analytically calculated under the assumption of a von-Mises yield locus having measured the hardening behavior under uniaxial stress conditions.

$$\sigma_y = k(\sqrt{3} \tau) \quad (3.3.8)$$

The torsion experiments were simulated with the two different hardening curve approximations from Table 3. In order to be able to better compare the shapes of the simulated torque curves with the experiments, the parameter k from equation 3.3.8 has been found for each hardening curve approximation under the constraint:

$$Torque_{exp,\varepsilon=80\%} = Torque_{Sim,\varepsilon=80\%} \quad (3.3.9)$$

This procedure gave $k=0.946$ for the Hensel Spittel approximation and $k=0.926$ for the Hockett Sherby Approximation. Figure 29 shows the measured torque as a function of the strain at the outer diameter, analytically calculated and the torque-strain curves received from simulations of the torsion experiments using the different flow curve approximations, as well as their slopes. Strains of 150% at the outer diameter could be reached in this experimental setup. The slope of the experimental torque curve shows a local maximum around 130%. This maximum is an artefact due to machine eccentricity.

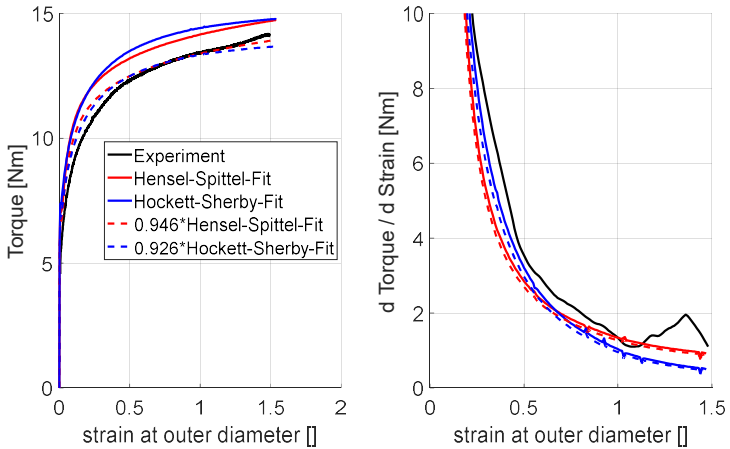


Figure 29: Experimental and simulated torque-strain relationships and their derivatives using different hardening curve approximations

Figure 29 right clearly shows, that the Hockett-Sherby extended approximation tends to underestimate the slope of the torque curve for high strains due to its saturating nature. The Hensel Spittel approximation does not have this saturating nature and fits the slope better for high strains. It fits the data very well, neglecting the local maximum in experimental data due to machine excentricity.

3.3.3.2 Validation through hardness measurements

Another approach for validation of the large strain hardening approximation comes from hardness measurements. As described in chapter 2.3.1 the current yield stress can be approximated by a hardness measurement. An empirical linear relation is given by equation 2.3.11. To transfer the relative to an explicit formulation, one point with known hardness and yield stress is needed as reference point. This point was obtained by measuring the hardness of a compressed dilatometer probe, of which also the current yield stress is known from the dilatometer test. This reference point has a strain of 40%, a Vickers hardness of 205.5 Hv and a yield stress of 736MPa. Under these constraints, equation 2.3.11 can be expressed explicitly as given by equation 3.3.10 for one measurement i .

$$\sigma_{y,i} = 736MPa + 2.876(H_{V,i} - 205.5H_V) \quad (3.3.10)$$

The data points with higher strains used for validation come from samples, that were rolled over, as described later in chapter 4. Measuring the hardness of the samples near their surface gave hardness measurements at very high strains. The corresponding strain values for each sample were quantified by simulations of the cross rolling process as described in chapter 5. Figure 30 gives the resulting flow stress approximations from hardness measurements (equation 3.3.10) at the corresponding strain values, as well as the flow curve approximation from the Hensel Spittel and the Hockett Sherby

approximations. It is clear from this chart that the Hensel-Spittel flow curve formulation approximates the yield stress data points obtained from hardness measurements better than the Hockett Sherby formulation which tends to underestimate the large strain hardening behavior of this material.

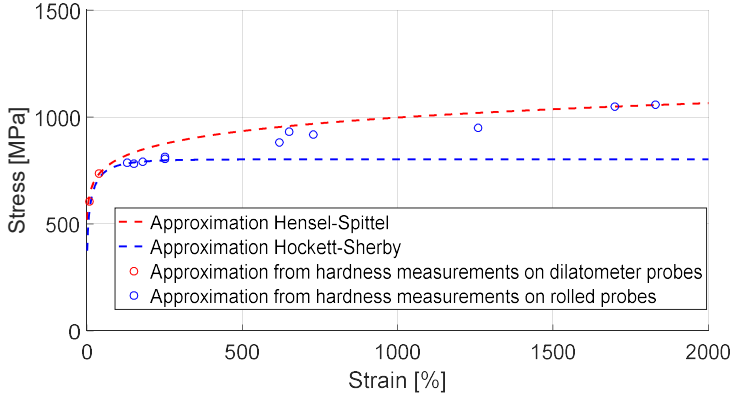


Figure 30: Hardness measurements and corresponding flow stress approximations

This finding is in good agreement with the work of (Gil Sevillano, van Houtte, & Aernoudt, 1980) who recommend non-saturating flow curve approximations for ferritic-pearlitic steels as introduced in chapter 2.3.1. For all the given reasons the Hensel Spittel formulation is chosen for all following simulations.

3.4 Experimental fracture behavior of 20MnB4

Having investigated the hardening behavior of 20MnB4, the investigation of the material's fracture behavior will be discussed in this section. Being the basis for the parameter identification of all used fracture criteria this chapter is of major importance. The following subchapter will then mathematically model the material's fracture behavior based on the results obtained in this subchapter.

3.4.1 Experimental setup and program

In order to quantify the material's fracture behaviour as a function of the stress state, unnotched tensile experiments, differently notched tensile experiments, as well as torsion experiments with different levels of superimposed tension or compression have been performed. Figure 31 shows the specimen geometries used. For details on the geometries see Appendix 1 to Appendix 4.

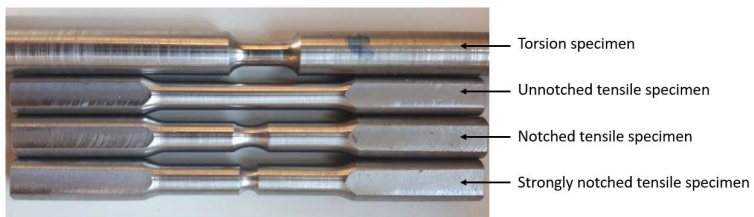


Figure 31: Specimen geometries used for investigation of fracture behavior

Tensile tests were performed at a ZwickRoell machine of type BZ1-MMRM050.ST02. The experiments were performed inside a thermal chamber which gives the option to vary the testing temperature. Extensometers were directly mounted to the probe ensuring a correct elongation and strain measurement. In order to also be able to quantify

the current diameter of the tensile specimen during deformation, a Panasonic AG-AC160AEJ camera with a frame rate of 25 frames per second was used to record the probe's dimensional changes.

While for the mentioned tensile tests, the evolution of the stress state over the experiment is mostly predefined by the probe's initial geometry, for the torsion tests the stress state during forming can be defined through an arbitrary superposition of tensile or compressive strain rate components.

Torsion tests were performed on a STD810 torsion-deformation machine produced by Bähr Thermoanalyse GmbH. Figure 32 left shows the experimental setup of the torsion experiments. The used probe is inductively heated and its temperature measured through a type S thermocouple and controlled by the machine. The thermocouple is spot welded as visible in Figure 32 right on the sample's shoulder. Although the temperature measurement would be more precise if the thermocouple was welded to the deformed area of reduced diameter, this could not be done since the spot weld created an inhomogeneity on the probes surface that lead to early cracking of the probe.

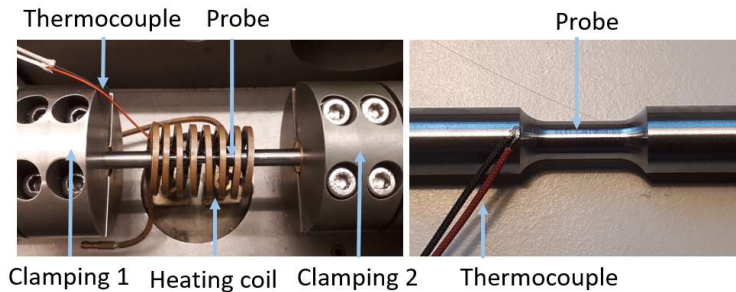


Figure 32: Left: Setup of torsion experiments, Right: Position of thermocouple

In order to investigate the temperature- and strain-rate dependency of the material's ductility, torsion tests have been performed at varying temperatures and strain rates. Table 4 shows the full experimental program for the investigation of the fracture behavior in function of stress state, temperature and strain rate.

Experimental code	Specimen geometry	Load type	Av. Strain Rate Tension [1/s]	Av. Strain Rate Torsion [1/s]	Av. Temp. [°C]
TO1	Torsion	Torsion + Compression	-0.01	0.1	170
TO2	Torsion	Pure Torsion	0	0.1	170
TO3	Torsion	Torsion + Tension	0.035	0.1	170
TO4	Torsion	Torsion + Strong Tension	0.06	0.1	170
TO5	Torsion	Pure Torsion	0	0.1	20
TO6	Torsion	Pure Torsion	0	0.1	250
TO7	Torsion	Pure Torsion	0	0.1	300
TO8	Torsion	Pure Torsion	0	0.1	400
TO9	Torsion	Pure Torsion	0	1	170
TO10	Torsion	Pure Torsion	0	10	170
TE1	Unnotched Tensile	Pure Tension	0.1	0	170
TE2	Notched Tensile	Pure Tension	0.1	0	170
TE3	Strongly notched Tensile	Pure Tension	0.1	0	170

Table 4: Experimental program to investigate the fracture behavior

3.4.2 Evaluation methodology

All the experiments listed in the experimental program were deformed until fracture occurred. Each experiment was then rebuilt as a finite element simulation in the FE software Simufact forming v14. The evolution of stress- and strain state over the sample until fracture could be extracted from these simulations. One major challenge here is how to synchronize the moment of fracture between experiment and simulation. For the two major types of experiments- torsion and tension experiments- this key point in accuracy of fracture prediction will be discussed on the following three pages.

Tension experiments

Simulating the tensile experiment until the total elongation to fracture as measured by extensometer is reached is one possible approach frequently used in the literature (Wesner, 2017). A major challenge in this approach is that necking will occur somewhere between the two extensometer sensors and is not quantified by the elongation. Depending upon the extent of material necking, stress and strain states at the particle of crack initiation can be significantly different. Furthermore the necking behavior in the FE-simulation is sensitive to the used element edge sizes and the hardening curve's sensitivity to strain rate and temperature. All these dependencies may falsify results. This approach is not followed in this study.

A second possible approach that overcomes the disadvantages of the first approach is just measuring the remaining fractured probe diameter and then simulating until this diameter is reached, similar to the approach of (Gorji Bandpay, 2015) who evaluated fracture strains of sheet metal. Since it measures the fractured surface it quantifies the extent of necking directly. On the other hand it has been proven (Tvergaard & Needleman, 1984), (Besson, Steglich, & Brocks, 2001) that the measured diameter of the fractured specimen deviates from the one at which fracture initiates for round tensile bars (see also Figure 33 middle and right). This is due to the typical cup cone fracture mechanism that governs ductile fracture in a cylindrical tensile probe. The crack initiates in the center of the probe. While growing to the outer diameter, the probe diameter keeps reducing, falsifying the remaining fractured diameter. For this reason also this approach is not followed in this study.

Instead, the tensile experiments are recorded optically with a Panasonic AG-AC160AEJ camera at a frame rate of 25 frames per second. The probe diameter imminent to fracture has been optically measured in the video recordings on the last picture before fracture. This is assumed to be the crack initiation diameter (see Figure 33 middle).

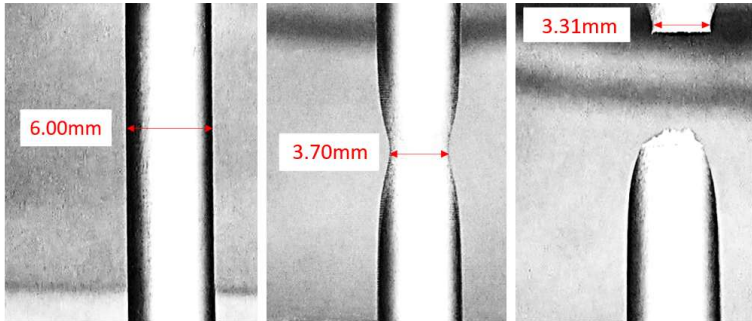


Figure 33 : Left: Initial tensile Probe shape, Middle: Shape one picture before fracture, Right: Fractured shape

Since an analytical strain calculation is always a simplification due to non-uniform strain distribution over the radius (see Figure 34 right), the tensile experiments were then simulated until the optically measured crack initiation diameter was reached in the simulation. The fracture strain and stress state was evaluated at the centerline of the probe, which is the point of the highest strain and stress triaxiality in the specimen.

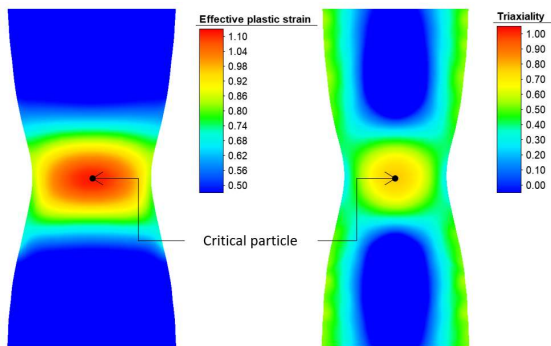


Figure 34: Strain- and triaxiality distribution over a cut section of a simulated unnotched tensile experiment imminent to fracture

Torsion experiments

For the torsion experiments with superimposed tension it is a valid evaluation approach to measure the remaining necked probe diameter and simulate the experiment until this diameter is reached. This is because the highest strains in torsion experiments are reached at the outer diameter (see Figure 35 left) indicating fracture initiation on the probe surface, which is in contrast to fracture initiation in tensile experiments. In torsion experiments with superimposed tension, not only the remaining diameter but also the twisting angle to fracture determines the resulting fracture strain. For this reason the moment of crack initiation was defined as the simultaneous agreement of simulation with both the experimentally measured fracture diameter and the twisting angle to fracture. The same reasoning holds for the torsion experiments with superimposed compression.

The definition of the moment of crack initiation for pure torsion tests is straightforward. Since there is in general no change of probe diameter in pure torsion tests, the moment of crack initiation can be purely defined by the twisting angle to fracture. Fracture strains are then extracted from a simulation of the process to the experimentally observed final twisting angle (see Figure 35). Like this, also the reduction of the yield stress due to non-uniform temperature increase is incorporated.

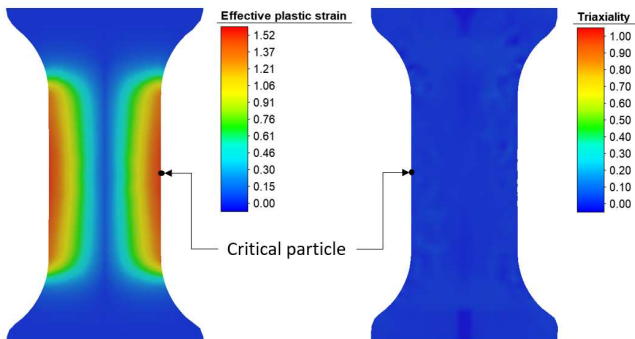


Figure 35: Strain- and triaxiality distribution over a cut section of a simulated pure torsion experiment imminent to fracture

3.4.3 Stress- and strain paths to fracture

Having set up the simulations and determined the instants of fracture as described above, a material particle was generated at the critical particle position indicated in Figure 34 for tensile experiments and Figure 35 for torsion experiments. At this point, stress and strain state evolution over the forming process were evaluated. The simulated stress paths (Normalized Lode angle parameter and stress triaxiality) and strain paths for torsion experiments TO1-TO4 and tension experiments TE1-TE3 evaluated at the respective critical particle until fracture are given in Figure 36.

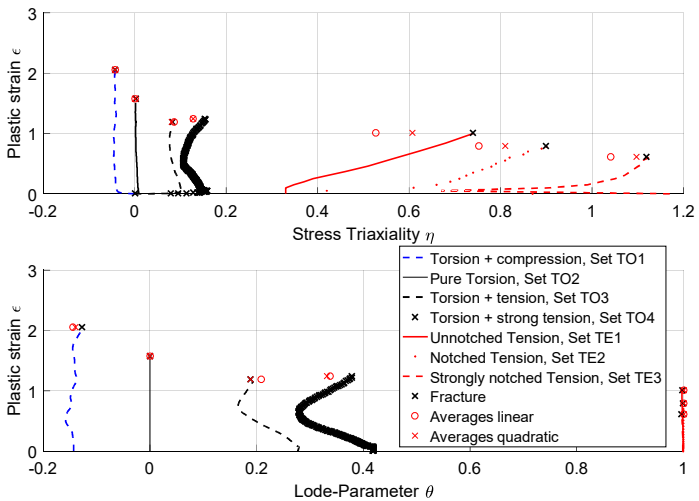


Figure 36: Evolution of stress states to fracture for all torsion and tension experiments.

3.4.4 Parametrization of the average stress state

While the torsion experiments' stress states do not vary very much over the experiment, the tension experiments' stress triaxiality-values increase significantly over the experiment due to necking (see Figure 36). The question how to reduce this non constant stress state variable to a single "equivalent" point for each experiment is a question of ongoing research. The most general approach can be formulated as given in equation 3.4.1 (Neukamm, Feucht, & Haufe, 2008; Xue, 2007). It is the averaging equivalent to the general nonlinear damage accumulation assumption introduced in chapter 2.5.7. The same equation holds for averaging normalized Lode angle parameters with $\bar{\theta}_{av}$ instead of η_{av} .

$$\eta_{av} = \frac{1}{D} \int_0^{\varepsilon_i} \frac{n}{\varepsilon_f} D^{\frac{n-1}{n}} \eta d\varepsilon \quad (3.4.1)$$

For D equation 2.5.29 from chapter 2.5.7 holds. In case of linear damage accumulation (equation) and assuming integration until fracture, meaning $n=1$ and $\varepsilon_i=\varepsilon_f$, the averaging equation reduces to the simple equation 3.4.2 proposed in (Johnson & Cook, 1985). This linear formulation is the standard averaging procedure nowadays, used most frequently (Wesner, 2017; Wierzbicki et al., 2005).

$$\eta_{av,lin} = \int_0^{\varepsilon_f} \frac{\eta}{\varepsilon_f} d\varepsilon \quad (3.4.2)$$

The results of these averaging procedures for the given paths to fracture are also plotted in Figure 36. Two averaging equations were applied. The first one is the standard linear averaging equation 3.4.2, given as red circles in Figure 36. The second one is a quadratic averaging procedure, meaning $n=2$ in equation 3.4.1, indicated as red crosses in Figure 36. Since the quadratic procedure weighs later stress states more than earlier ones, the quadratic average always lays

between the linear averaging result and the final stress state for each experiment.

A typical way to characterize the stress state under which a certain type of fracture experiment leads to fracture is to illustrate the experiment's $\bar{\theta}_{av}$ and η_{av} in the two dimensional space of $\bar{\theta}$ and η . Figure 37 gives this plot for the experiments TO1-TO4 and TE1-TE3. Both linear and quadratic average values are given for the experiments. The figure also indicates the location of possible plane stress states (equation 2.5.7), axially symmetric states under tension, axially symmetric states under compression and plane strain states.

Since round bars are used as tensile specimens and the critical particle is located on the bar's central axis, the stress states are axially symmetric states under tension. For torsion experiments, the critical particle is located on the specimen's surface. For that reason these states are located on the trajectory of all plane stress states.

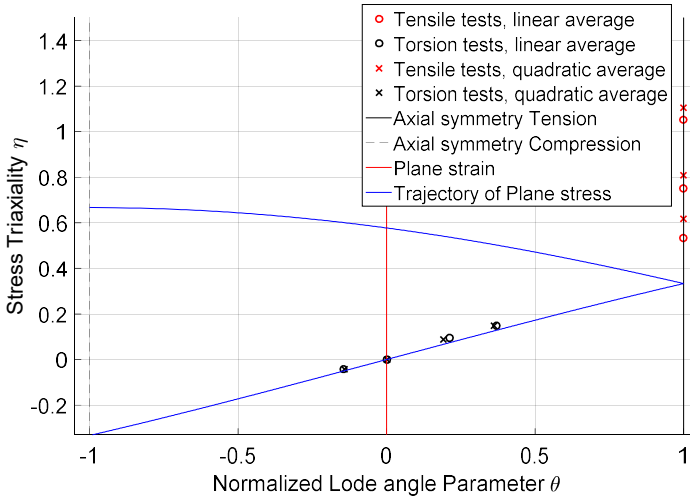


Figure 37: Averaged stress states of tension and torsion experiments

Table 5 sums up the averaged results for all experiments. They will be used for the parameter identification of all fracture models.

Experimental Code	ϵ_f [-]	Linear averages		Quadratic averages	
		$\eta_{av,lin}$ [-]	$\theta_{av,lin}$ [-]	$\eta_{av,quad}$ [-]	$\theta_{av,quad}$ [-]
TO1	208%	-0.0438	-0.1452	-0.043	-0.1406
TO2	158%	0	0	0	0
TO3	119%	0.0857	0.208	0.0807	0.188
TO4	124%	0.1278	0.338	0.128	0.331
TO5	155%	0	0	0	0
TO6	141%	0	0	0	0
TO7	97%	0	0	0	0
TO8	469%	0	0	0	0
TO9	148%	0	0	0	0
TO10	154%	0	0	0	0
TE1	101%	0.5265	1	0.608	1
TE2	79%	0.752	1	0.810	1
TE3	61.5%	1.041	1	1.097	1

Table 5: Fracture strains and averaged stress states of all tension and torsion experiments

3.4.5 Temperature- and strain rate dependency

While the experiments TO1- TO4 and TE1- TE3 investigate the stress state dependency of the fracture behavior keeping temperature and strain rate constant, experiments TO5- TO10 investigate the fracture behavior's strain rate- and temperature dependency while keeping the stress state constant. Figure 38 left gives the experimentally observed fracture strains under pure torsion as a function of temperature. Figure 38 right gives the fracture strains in function of strain rate.

The strain rate dependency does not show a clear trend in the investigated range of strain rates. The dependency on temperature, on the other hand shows a decrease of fracture strains for the experiments performed at 300°C, followed by a sharp increase at 400°C, while being more or less constant between room temperature and 250°C.

The found decrease in ductility with a local minimum around 300°C is a typical phenomenon for low alloyed carbon steels known as blue brittleness (Lange, 1988). The ductility minimum is dependent on the strain rate and shifts to higher temperatures the higher the strain rate. Since cross rolling processes typically happen under very high strain rate, the minimum in ductility is expected to be at rather higher temperatures. In (Lange, 1988) the minimum in ductility for a C15 steel is reported at 350°C at a strain rate of 0.7/s.

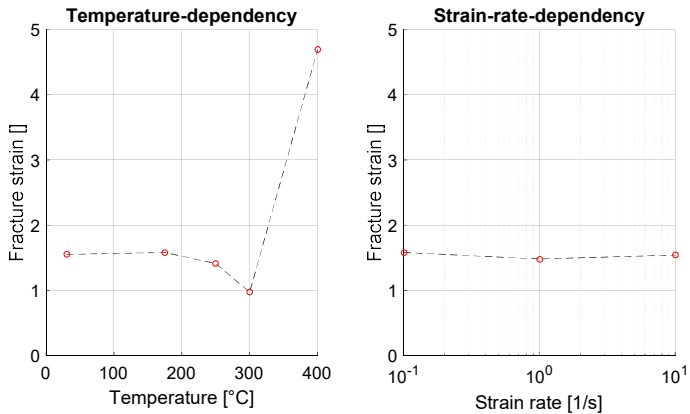


Figure 38: Temperature- and strain rate dependency of fracture behavior of 20MnB4 under pure torsion

As the results from Figure 38 show and in agreement with literature on blue brittleness, the temperature dependence of the material's fracture behavior is negligible up to 250°C. The strain rate sensitivity of ductility is negligible in the whole investigated range of strain rates. For this reason both effects will not be incorporated in the fracture model. This constraints the validity of the proposed fracture model to temperatures from 20°C to 250°C, which is given in most cooled cold cross rolling processes.

3.4.6 Repeatability

The discrete fracture values given in the previous chapters correspond to the material's average behavior that was investigated by performing each experiment several times. When repeatability of results was good, it was performed three times, otherwise up to five times. Figure 39 illustrates the scattering of resulting fracture strains with respect to the experiments' linear stress averages making use of error bars for all tension and torsion experiments.

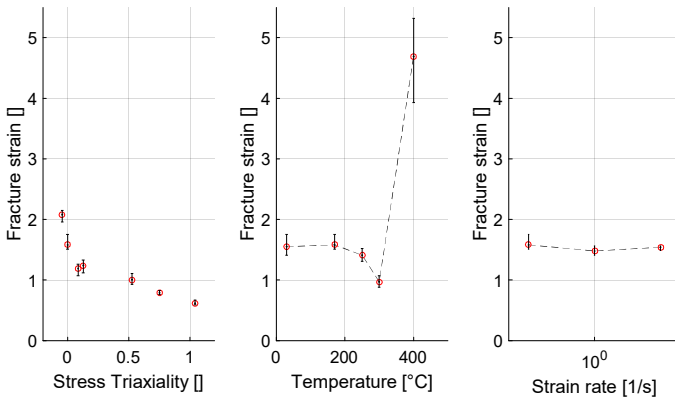


Figure 39: Scattering of tension and torsion experimental results

The overall scattering of results is low. The only experiment that shows a higher scattering is the torsion experiment at 400°C, above the temperature range of blue brittleness. One possible explanation for this is that above the blue brittle temperature range the ductility is very sensitive to slight changes in temperature. When the torsion specimen is positioned in the heating coil, temperature will vary slightly with position. Since the proposed fracture model will be valid in the range of room temperature to 250°C, the scattering of the results at 400°C is negligible. The overall repeatability of experimental results is very good.

3.5 Mathematical approximations to predict fracture

In this section, different fracture criteria will be calibrated to the experimental data from the previous subchapter in order to extrapolate the fracture behavior over the full range of possible stress states. Both the linear and quadratic averages will be used for calibration purposes. From the abundance of ductile fracture criteria the following were chosen for closer investigation:

- Johnson Cook (JC) fracture criterion
- Mohr Coulomb (MC) fracture criterion
- Hosford Coulomb (HC) fracture criterion

The Johnson Cook fracture criterion was chosen because it is a simple frequently used criterion that has revealed good performance in some processes (Wesner, 2017). The Mohr-Coulomb criterion is a standard fracture criterion in geo-physics and recent literature (Dunand & Mohr, 2014) has proposed that it is also very suitable to predict ductile fracture. The Hosford Coulomb criterion is a very recently proposed criterion that is based on the MC criterion and is reported to reveal even better performance than the MC criterion for some materials (Mohr & Marcadet, 2015).

These criteria are first calibrated from all tension and torsion experiments. Then the robustness of the criteria is evaluated by recalibrating them using only a limited number of experiments. Varying the choice of experiments used for calibration will help evaluating the criteria's robustness. Finally, the fracture criteria's accuracy in predicting fracture of tension and torsion tests will be evaluated.

As explained in chapter 3.4.4 the criteria are modeled as independent of temperature and strain rate. In the range of working conditions of the modeled cross rolling processes this assumption is justified.

3.5.1 Parameter identification

The criteria were fitted to the given experimental data by minimizing the sum of squared errors with respect to predicted fracture strains (equation 3.5.1), where n is the number of experiments used for calibration. In this section, all experiments with varying stress state, TO1-TO4 and TE1-TE3, were used for parameter identification, which means n equals seven.

$$\min \left\{ \sum_{i=1}^n (\varepsilon_{fit}^i - \varepsilon_{meas}^i)^2 \right\} \quad (3.5.1)$$

3.5.1.1 Johnson Cook fracture criterion

The Johnson Cook criterion calibrated from the experimental data is given in Figure 40. It was calibrated once using the experiments averaged linearly and once the experiments averaged quadratically. The two resulting fracture surfaces are very close to each other, so that they cannot be distinguished in the figure. The criterion, by nature of its formulation is independent of the normalized Lode angle parameter. Table 6 gives the resulting parameters of the criterion.

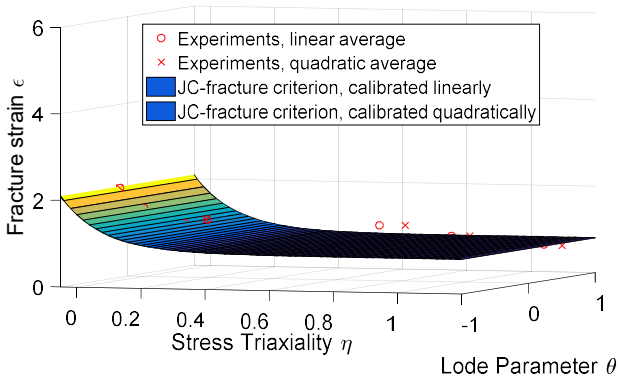


Figure 40: Shape of the JC fracture criterion for 20MnB4 in mixed stress-strain space

Data used for calibration	C1	C2	C3
TO1-TO4, TE1-TE3 linear averages	0.7993	0.8758	-7.503
TO1-TO4, TE1-TE3 quadratic averages	0.809	0.8606	-7.994

Table 6: Parameters of the JC fracture criterion for 20MnB4

3.5.1.2 Mohr Coulomb fracture criterion

Secondly, the MC criterion was calibrated from the experimental data, using first linear averages, then quadratic averages. Because it was found that temperature- and strain rate dependency of the fracture behaviour are negligible, it is convenient to perform the parameter identification in the mixed stress strain space formulation of the MC criterion (equation 3.5.2). If the identification was performed in a pure stress space, the equivalent fracture stress would have to be modelled as dependent on temperature and strain rate. This would make the model more complicated.

The mapping from the stress to the strain space has to be performed by the inverse of the Hensel Spittel hardening curve. Neglecting the $e^{\frac{c_2}{\varepsilon}}$ term in the Hensel Spittel hardening approximation, which does only have an influence for very small strains, there is a closed form analytical formulation of the Mohr-Coulomb fracture criterion in the mixed stress strain space:

$$\varepsilon_f = \left(\frac{Ae^{m_1 T} \frac{1}{|\dot{\varepsilon}|} (\dot{\varepsilon}[s])^{m_2}}{c_2} \left[\sqrt{\frac{1+c_1^2}{3}} \cos\left(\frac{\bar{\theta}\pi}{6}\right) + c_1 \left[\eta + \frac{1}{3} \sin\left(\frac{\bar{\theta}\pi}{6}\right) \right] \right] \right)^{\frac{1}{n}} \quad (3.5.2)$$

Assuming independency of temperature and strain rate the mapping can be performed for one temperature at one strain rate. In this case 160°C and 0.1/s are chosen. Inserting the Hensel Spittel flow curve parameters derived in section 3.3.3, the MC fracture criterion becomes

independent of temperature and strain rate and can be analytically expressed as:

$$\varepsilon_f = \left(\frac{721.71 \text{MPa}}{c_2} \left[\sqrt{\frac{1+c_1^2}{3}} \cos\left(\frac{\bar{\theta}\pi}{6}\right) + c_1 \left[\eta + \frac{1}{3} \sin\left(\frac{\bar{\theta}\pi}{6}\right) \right] \right] \right)^{\frac{-1}{0.0944}} \quad (3.5.3)$$

Figure 41 gives the shapes of the MC criterion in the mixed stress-strain space. Again the shape of the criteria calibrated from the linear averages and the quadratic averages can barely be distinguished. Table 7 gives the corresponding model parameters.

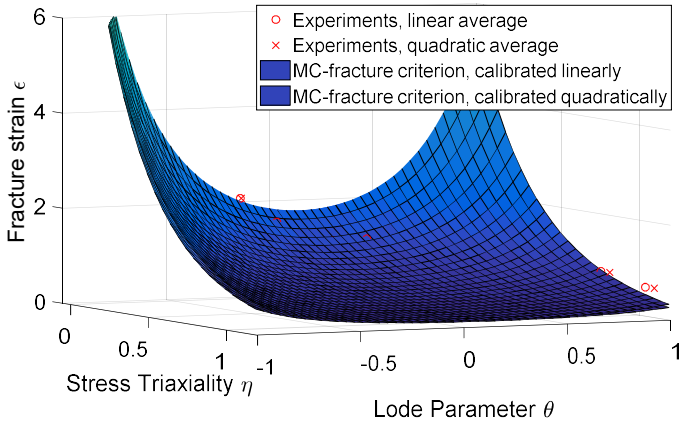


Figure 41: Shape of the MC fracture criterion for 20MnB4 in mixed stress-strain space

Data used for calibration	c1	c2
TO1-TO4, TE1-TE3 linear averages	0.1382	440.27 MPa
TO1-TO4, TE1-TE3 quadratic averages	0.1268	439.66 MPa

Table 7: Parameters of the MC fracture criterion for 20MnB4

3.5.1.3 Hosford Coulomb fracture criterion

Like for the MC criterion, the parameter identification was performed in the mixed stress strain space, assumed as independent of temperature- and strain rate effects. For an exact formulation of the Hosford Coulomb criterion in the mixed stress strain space the reader is referred to (Mohr & Marcadet, 2015). The resulting fracture criterion using the quadratic averages was similar to the MC criterion (see parameters in Table 8). The shape of the criteria calibrated from linear and quadratic averages are given in Figure 42. For this criterion, a small difference between these two criteria's surfaces is visible.

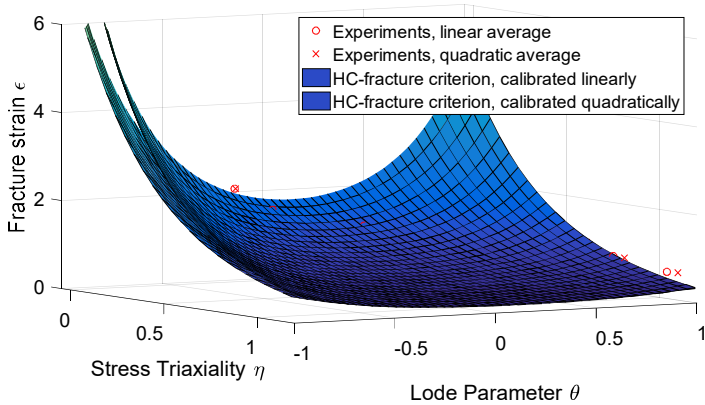


Figure 42: Shape of the HC fracture criterion for 20MnB4 in mixed stress-strain space

Data used for calibration	a	c1	c2
TO1-TO4, TE1-TE3 linear averages	1.137	0.1081	423.77MPa
TO1-TO4, TE1-TE3 quadratic averages	1.039	0.118	436.64MPa

Table 8: Parameter of the HC fracture criterion of 20MnB4

3.5.2 Evaluation

In order to verify the parameter identification and the capabilities of the fracture models, the absolute errors AE_i for each experiment R_i and the mean absolute error MAE over all rolling experiments defined by equation 3.5.4 were calculated. The measured fracture strains $\varepsilon_{f,meas,i}$ for each experiment are the ones given in Table 5. This was done for each fracture criterion calibrated from all experimental data. Both linear and quadratic averaging procedures were evaluated. Figure 43 gives the results.

$$MAE = \sum_{Ri=R1}^{R7} \frac{AE_i}{7} \quad (3.5.4)$$

$$AE_i = |\varepsilon_{f,meas,i} - \varepsilon_{f,fit,i}| \quad (3.5.5)$$

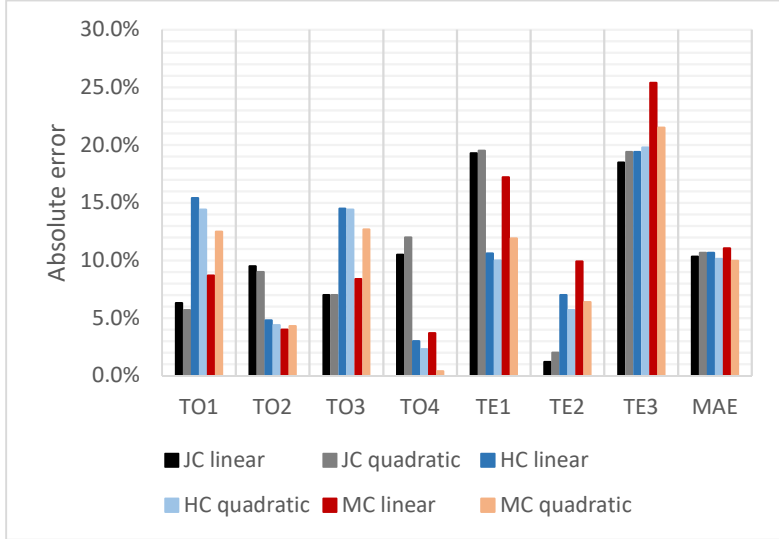


Figure 43: Absolute errors of fracture criteria calibrated from all experiments

3.5.3 Interpretation

The MAE is between 9.9% and 11.0% for all the criteria when using all data for calibration (see Figure 43), making them all an apparently good choice for the modelling of the ductile fracture behavior. This holds for both linear and quadratic averaging procedures. Since all fracture criteria are able to model the experimental results with similar absolute errors, it is barely possible to judge which of the criteria is most accurate and it is not clear, which criterion is most suitable to predict ductile fracture in cross rolling operations.

When comparing the shapes of the different criteria (Figure 40, Figure 41, Figure 42), one can see that in the extrapolated regions the fracture criteria vary significantly, although they all approximate the experimental data points used for calibration rather well. Since stress states in the workpiece core during cross rolling are in these extrapolated regions (see chapter 5.2), it can be expected that fracture prediction in cross rolling operations will vary significantly depending on the used fracture criterion.

For these two reasons, a process-near evaluation of the fracture criteria for cross rolling applications is needed. This will be given in chapters 4 and 5. First, the robustness of the different criteria will be assessed.

3.5.4 Analysis of robustness

To keep calibration efforts and costs low, it is of major interest, how robust the fracture criteria behave when reducing the number of experiments used for calibration. This is investigated here.

3.5.4.1 Procedure

In the given experimental program, there are seven fracture experiments with varying stress state (TO1-TO4 and TE1-TE3). To investigate the robustness of the calibration of the criteria the following procedure was employed:

- fracture criteria were re-calibrated with a reduced number of experiments instead of seven.
- The choice of the experiments used for re-calibration was varied.
- Only linear averages of stress states were used here.

The resulting shapes of the fracture criteria were then compared to identify the robustness of the criteria. The choice of experiments used for calibration was done under the following constraints:

- For each fracture criterion the number of experiments used for each calibration is set to four.
- To achieve meaningful results, the calibration experiments were chosen such that in each combination of experiments used at least one experiment was taken from torsion and at least one from tensile experiments.

Under these constraints the total number j of possible choices of experiments for re-calibration of the criteria is:

$$\binom{4}{2}\binom{3}{2} + \binom{4}{1}\binom{3}{3} + \binom{4}{3}\binom{3}{1} = 34 \text{ Combinations} = j \quad (3.5.6)$$

3.5.4.2 Evaluation

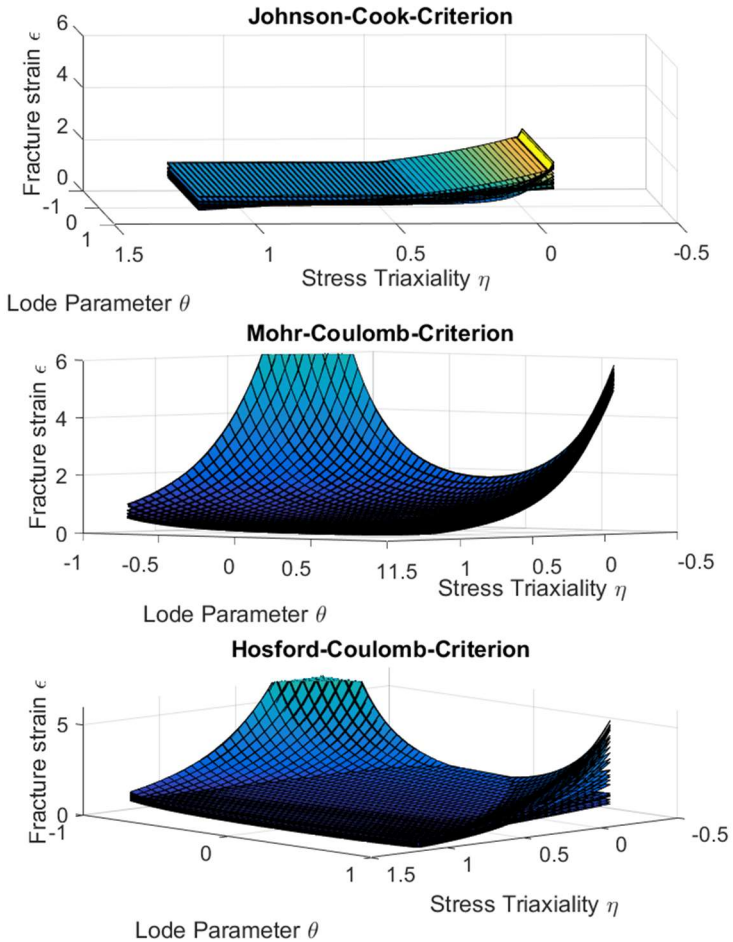


Figure 44: Illustration of robustness of the Johnson-Cook, Mohr-Coulomb and Hosford-Coulomb fracture criteria

For the robustness analysis of the various criteria $j=34$ combinations of choices of experiments were used to calibrate each fracture criterion according to equation 3.5.1 (minimizing square error sum) where n equals four. All 34 resulting shapes of each fracture criterion are plotted in Figure 44 for optical comparison.

It was found that the JC criterion's shape depends on the choice of experimental data points in a remarkable way (see in Figure 44 on top). This shows the limited robustness of the criterion and may be partially contributed to its purely phenomenological nature. For the given experimental data set, more than four experiments should be used for the calibration of this criterion.

The MC fracture criterion's 34 shapes in the mixed stress strain space are all plotted in in Figure 44 (middle). It was found that maybe due to its physically motivated nature and the shape given implicitly through the flow curve formulation, this criterion is very robust with respect to the choice of experiments for calibration. This can be seen from the fact that all 34 fracture surfaces have a very similar shape.

The HC criterion in contrast changes its shape remarkably when varying the choice of data points used for calibration (see in Figure 44 bottom). For the given experimental data set, more than four experiments should be used for calibration to obtain reliable results.

In order to quantify the robustness of the fracture criteria, the maximum absolute error for each experiment i $\max(AE_i)$ was calculated when only using a limited number of four experiments for calibration. It was determined as the maximum deviation from all the 34 identified fracture surfaces per fracture criterion to each experiment. This maximum absolute error is given in equation 3.5.7, where the measured fracture strains $\epsilon_{meas,i}$ for each experiment are the ones given in Table 5. The mean maximum absolute error $M\max(AE)$ was then calculated over all experiments with equation 3.5.8. The calculated errors are illustrated in Figure 45 for all experiments.

$$\max(AE_i) = \max_{1 < k < j} \{|\varepsilon_{meas,i} - \varepsilon_{fit,i,k}|\} \quad (3.5.7)$$

$$Mmax(AE) = \sum_{Ri=R1}^{R7} \frac{\max(AE_i)}{7} \quad (3.5.8)$$

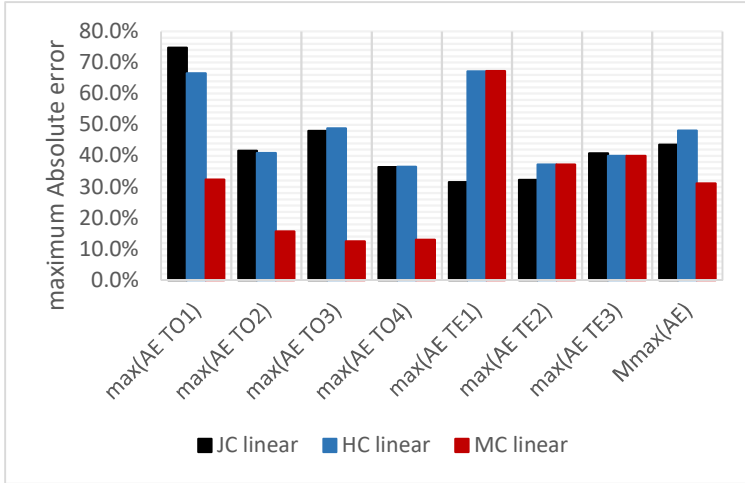


Figure 45: Maximum absolute errors of fracture criteria calibrated from reduced number of experiments

Although the MC fracture criterion has the lowest number of parameters to be calibrated it shows the lowest maximum deviations (31.1% on average). This indicates that the model is more robust than the other two to a calibration under limited number of experiments, which is in accordance with the optical appearance of the robustness analysis given in in Figure 44.

With 43.6% and 48.1% respectively the JC and HC show higher maximum deviations on average. These models can only model the experimental fracture behavior with a similar robustness when increasing the number of experimental data points used for calibration. This makes them less robust than the MC criterion and indicates that a higher experimental effort and costs have to be accepted for reliable calibration results of these criteria.

4 Analysis of core cracking in cross rolling experiments

In the previous chapter the calibration of fracture criteria from tension and torsion experiments was described in detail. It was found that the various fracture criteria are able to describe the experimental fracture behavior with a very similar mean absolute error although the shape of the criteria is significantly different for the extrapolated regions of stress states. From these standard tension and torsion tests it is therefore not possible to assess which fracture criterion is most accurate in predicting core crack initiation in rolling operations. For this reason, in this chapter, an experimental profile cross rolling procedure is described in detail to investigate core crack initiation in the actual rolling process.

This experimental method leads to core cracks under varying process parameters. The dependency of the crack initiation on tool-dependent process parameters (roller geometry) and on process dependent parameters (ratio of revolutions per diameter reduction) will be investigated. A methodology for the investigation of internal core cracks is introduced as given in (Komischke et al., 2018) and (Komischke, Hora, & Domani, 2018). A simplified machine stiffness model and a procedure to account for machine elasticity effects in the planning of the experimental program are also given. The results of fracture investigation for all cross rolling experiments are presented. This will be the basis for a numerical assessment of the criteria's accuracy in cross rolling operations in the next chapter 5. Finally, general remarks on the process stability and repeatability are given.

4.1 Raw material preforming

The raw material used in this work is a hot-rolled wire (see chapter 3.1). It is delivered in coils (Figure 46 left). As visible, the wire is bent repeatedly over multiple axes. For the planned rolling experiments a straight workpiece shape is essential in order to guarantee process stability. For this reason the raw material is wiredrawn (see Figure 46 middle) and cut into pieces with a length of 200mm before the rolling process (see Figure 46 right).



Figure 46: Left: Raw material delivered as wire coils before preparation, Middle: Wiredrawing, Right: Wiredrawn billets after preparation

Deformations and damage from wiredrawing should be small compared to the deformations induced by rolling, in order to investigate the fracture behavior under rolling conditions, which is the goal of this study. For this reason the initial wire diameter was chosen to be 11mm, which is then drawn down to a diameter of 10.5mm. This diameter reduction induces a strain that can be analytically estimated according to equation 4.1.1 as 9.3%, which is small compared to the deformations from the following cross rolling processes. The used drawing die was a AK30-75-10,50-18 according to (DIN1547, 1969-07). Its technical drawing is given in Appendix 5.

$$\varepsilon_{drawing} = \ln\left(\frac{d^2}{d_o^2}\right) \quad (4.1.1)$$

4.2 Tool geometry and experimental setup

Cross rolling experiments have been performed on a PWZ40 CNC/AC machine produced by Profiroll Technologies GmbH, Bad Dübén Germany. The machine is a cross rolling machine that uses round roller geometries and deforms the workpiece by an adjustable axial feeding speed. The machine offers a process cooling by an emulsion rinsing the deformation zone to avoid overheating of the workpiece. Further machine data are given in Table 9 (Profiroll-Technologies-GmbH, 2000).

Machine Parameter	Unit	Value
Possible Workpiece diameters	mm	5-100
Possible Roller diameters	mm	160-235
Maximum Normal Force	kN	400
Maximum Roller Torque	Nm	5000
Angular velocity of rollers	Rpm	0-150
Mass	kg	9000
Size	m ³	2.25 x 2.05 x 2.7

Table 9: Machine data of profile rolling machine PWZ40 CNC/AC

With this machine, notches of varying widths of 5mm, 7.5mm, 10mm, 15mm and 20mm have been rolled into the prepared billets of 20MnB4 using roller segments of corresponding widths (see Figure 47). A full technical drawing of all roller segment variants is given in Appendix 6 and Appendix 7. The roller geometries were specifically designed in a way to cause core cracks under different stress- and strain states (see chapter 5.2.4). The overall diameter of the roller segments was 205mm for all rollers. These segments were sand blasted in order to achieve a roughness that avoids slippage and guarantees a stable rolling process. Roughness measurements on similar tools, sandblasted under the same conditions gave $R_a=4.6\mu\text{m}$ and $R_p=14.2\mu\text{m}$ on average (John, 2018). The initial workpiece bar diameter was 10.5mm.

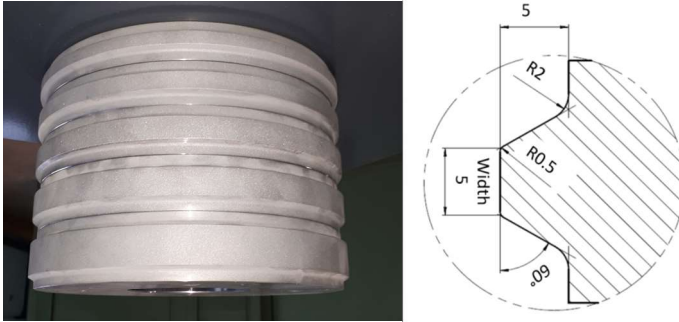


Figure 47: Left: Rollers of different widths, Right: Exemplary roller geometry of width 5mm (full drawing in Appendix 6 and Appendix 7)

The experimental setup is shown in Figure 48 left. The workpiece bar was held in position during the process by two bushes, one on each side of the bar, in order to guarantee a stable process. Using only one bush, the process became unstable and the workpiece bent out of the roll gap. The process was cooled by an oil-water emulsion to avoid workpiece overheating. Figure 48 right shows bars with rolled notches of different widths.

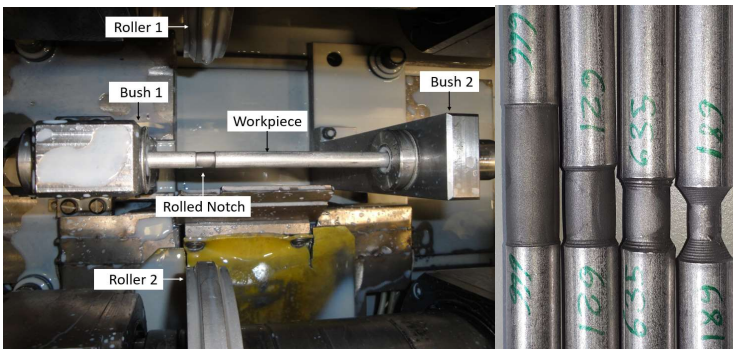


Figure 48: Left: Experimental cross rolling setup, Right: Rolled workpieces with notches of different widths

4.3 Experimental methodology

By nature of an internal crack it cannot be seen optically from the outside. This poses two main challenges in the framework of experiments.

1. Execution of experiments: During the experiments it is not visible whether the workpiece's core has already cracked. It remains unclear how far to reduce the diameter to achieve the core crack.
2. Experimental evaluation: Each rolled workpiece has to be investigated for internal cracks after the rolling process.

In order to overcome the first challenge, for each parameter configuration, workpieces were rolled down to several different diameters (See Figure 49 for an illustration). Each experiment was repeated between 3 and 10 times. Later, all samples were investigated for cracks. The crack initiation diameter (9.95mm in Figure 49) was defined as the average between the first diameter at which the majority of the samples were cracked (9.9mm in Figure 49) and the last diameter for which the majority of the samples were uncracked (10.0mm in Figure 49). If for one diameter just 50% of the samples was cracked, this diameter was defined as crack initiation diameter.

$$D_{crack\ initiation} = \frac{D_{first\ cracked} + D_{last\ uncracked}}{2} \quad (4.3.1)$$

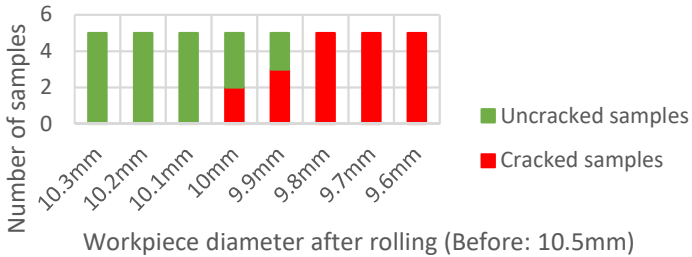


Figure 49: Illustration of crack investigation methodology

To overcome the second challenge (crack investigation) different procedures were evaluated:

- 3D computed tomography
- 2D X-Ray Scanning
- Cutting, embedding and polishing

A total of 100 samples were investigated for cracks by 2D X-Ray Scanning and the results were compared to results obtained from the cutting and polishing crack investigation procedure. Appendix 8 gives details on the parameters of the X-Ray analysis. It was found that good results were achieved with the cheap and fast cutting and polishing procedure and all cracks visible in the X-Ray investigations were also visible after cutting and polishing. This cutting and polishing method was applied for the vast majority of the samples. To do so, the rolled samples were cut in the middle, then embedded into a body of synthetic material (see Figure 50 left) and then ground and polished with decreasing SiC abrasive grain size of minimum $5\mu\text{m}$. This procedure resulted in a mirror finish (see Figure 50 left) that made it possible to see even very small cracks.

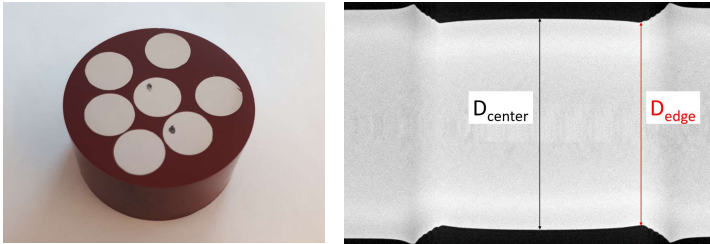


Figure 50: Left: Embedded and polished samples. Right: 3D-CT Scan of a notch

Both in CT-Scans and by measuring the notch dimensions it was found that the resulting diameter was not equal over the length of the notch, which is illustrated in Figure 50 right. The diameter at the edge of the notch D_{edge} was always smaller than the diameter in the center D_{center} . The edge diameter D_{edge} is representative of the roller movements because it represents the smallest diameter the workpiece

was compressed to. For this reason all upcoming workpiece diameter measurements are edge diameter values.

A crack classification methodology was developed, classifying the cracks from class 0 to class 4. This made it possible to assess crack growth over the process, as it will be shown in chapter 4.8. To classify the cracks, the maximum width of the crack in a plane with normal vector parallel to the workpiece axis was estimated or measured and categorized. To avoid measuring every single crack, crack sizes were estimated for the majority of the samples. Figure 51 shows the classification criteria as well as images received from different crack investigation procedures for each class of cracks.


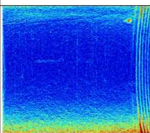
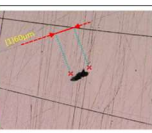

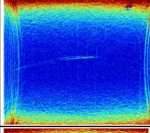
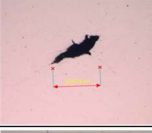
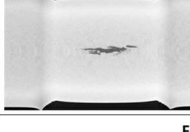
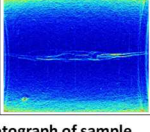
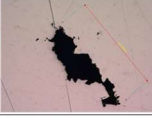




Crack Classification	Description	Max. crack-width [mm]	3D-CT-Scan	2D-X-Ray-Scan	Cut and polished sample
0	No Crack	0			
1	Several hairline cracks	< 0.1mm			
2	Well recognizable crack	0.1mm - 1mm			
3	Advanced crack	> 1mm			
4	Workpiece destroyed	Whole Workpiece	Photograph of sample		
					

Figure 51: Crack classification scheme

4.4 Experimental program

To understand, under which circumstances core cracks favorably occur in cross rolling processes, the rolling processes were performed under the variation of two main parameters essential to the process:

- The width of the rolled notch
- The ratio X defined as:

$$X = \frac{\text{Number of workpiece revolutions}}{\text{Workpiece diameter reduction}} = \frac{N}{\Delta D} \quad (4.4.1)$$

While the first parameter is predefined by the tool geometry used, the second one can be varied through the machine input. Another machine input parameter that had to be varied to limit the maximum workpiece temperature is the rotational speed of the rollers Ω . With a given diameter reduction ΔD to achieve and a given ratio of X , the rotational speed of the rollers determines the overall process duration. In this way it determines the overall strain rate in the workpiece $\dot{\epsilon}$. Assuming a constant cooling rate of the emulsion \dot{Q} and taking heat conduction into account, Ω also determines the temperature reached on the surface of the workpiece and the temperature gradient over the workpiece diameter. In the framework of this work, Ω is chosen such that the workpiece does not overheat to more than 250°C in order to avoid effects of blue brittleness, that were experimentally observed in chapter 3.4.4. Table 10 shows the experimental program derived under these considerations.

Experimental Code	Roller width	Rotational speed of rollers Ω	X_{Real}
R1	20mm	15 Rpm	6 Rev./mm
R2	15mm	15 Rpm	6 Rev./mm
R3	10mm	15 Rpm	6 Rev./mm
R4	7.5mm	15 Rpm	6 Rev./mm
R5	7.5mm	5 Rpm	2 Rev./mm
R6	5mm	10 Rpm	4 Rev./mm
R7	5mm	5 Rpm	2 Rev./mm

Table 10: Experimental program of cross rolling experiments

4.5 Linear one-dimensional machine stiffness model

Measuring the obtained workpiece diameters it had to be noticed that the target diameter reduction entered into the CNC machine control has never been fully reached. While for the 5mm wide roller 87% of the diameter reduction entered to the machine were realized at the workpiece, for the 20mm wide roller this ratio was as low as 38%. This makes the understanding of the phenomenon fundamental to a correct execution of the experimental program and to a correct virtual representation of the process.

It was found that the higher the normal force acting on the workpiece, the bigger the diameter gap. Figure 52 shows the diameter gaps as a function of the acting normal force on the workpiece. The measured data only deviates slightly from a linear relationship. For this reason this phenomenon is assumed to be the superposition of a linear stiffness phenomenon with an offset phenomenon. The line in Figure 52 is equivalent to a machine stiffness of $K_{\text{Mach}}=196\text{kN/mm}$ superimposed with an offset of the contact point of 0.412mm.

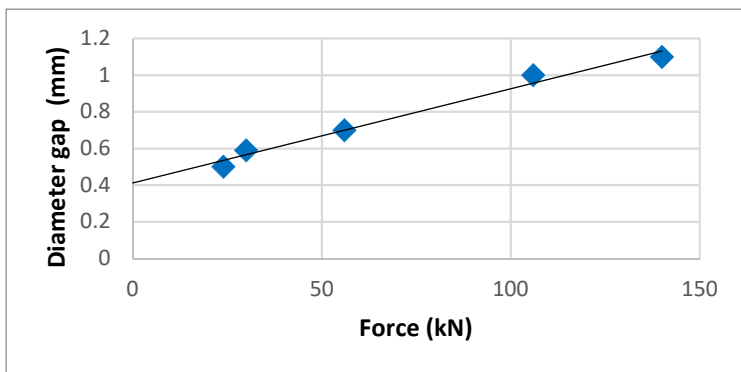


Figure 52: Linear one-dimensional machine stiffness model

4.6 Derivation of machine control inputs

Although the PWZ40 CNC/AC machine shows some significant elastic opening as shown in the previous subchapter, the precise experimental program from chapter 4.4. is to be executed. This subchapter will derive the stiffness-corrected CNC input parameters compensated for machine elasticity. Due to generally very high forces in cold cross rolling processes and high but limited machine stiffness this concept of stiffness compensation is expected to be transferrable and relevant for the experimental planning of many rolling processes.

In the experimental program performed the ratios from equation 4.6.1 and 4.6.2 between realized experimental results and CNC entered machine input values was valid, showing that without the shown machine input correction, the machine output is unpredictable and deviates significantly from the desired process. With the proposed correction, it was possible to achieve the desired planned diameter with an accuracy of $\pm 0.05\text{mm}$.

$$\frac{\Delta D_{Mach}}{\Delta D_{real}} \leq 2.5 \quad (4.6.1)$$

$$\frac{N_{Mach}}{N_{real}} \leq 2.4 \quad (4.6.2)$$

The given cross rolling machine is controlled by entering a path in the 2-dimensional space of workpiece diameter reduction ΔD over number of workpiece revolutions N . The solid black line in Figure 53 gives an illustration of an exemplary machine input, where the blue dashed line shows a resulting corresponding normal force measurement. In order to achieve the desired diameter reduction ΔD_{real} , the correct X_{real} and the correct N_{real} as postulated in subchapter 4.4, the entered machine control values were corrected for machine stiffness effects and offsets. The corrected values entered into the machine control are referred to as ΔD_{Mach} and N_{Mach} .

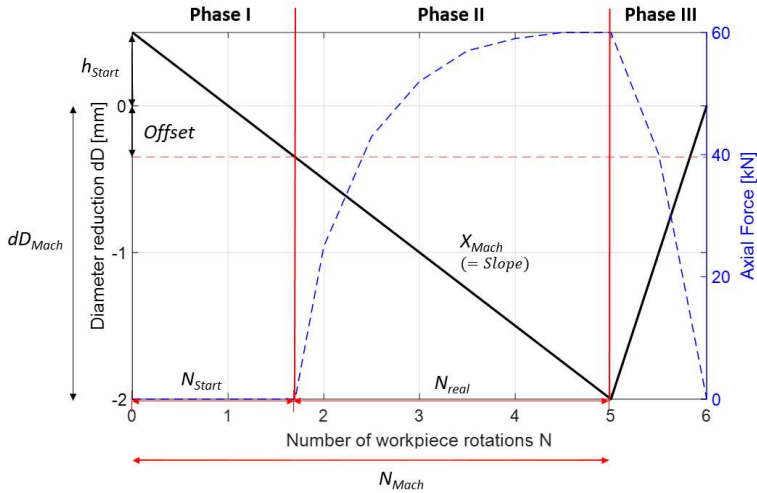


Figure 53: Illustration of machine input. Phase I: Approach of rollers, Phase II: Deformation, Phase III: Pull-Back of rollers

In Figure 53 the value h_{start} represents the distance of the rollers at the start of the process from the theoretical point of contact between rollers and workpiece ($\Delta D = 0$), which is a machine input variable. The Offset-value in Figure 53 is given through the difference of $\Delta D = 0$ (theoretical start of contact between roller and workpiece) and the ΔD -value at which the normal force starts increasing (true start of contact). The offset is the same that was already determined in a different way as 0.412mm in the previous subchapter.

Equations 4.6.3 – 4.6.9 are used to calculate ΔD_{Mach} and N_{Mach} from the above mentioned values, derived from simple considerations on Figure 53. The correction of the diameter reduction ΔD_{Mach} is straightforward:

$$\Delta D_{Mach} = \Delta D_{real} + \frac{F_{Max}}{k_{Mach}} + Offset \quad (4.6.3)$$

The number of real workpiece revolutions for workpiece deformation N_{real} can be expressed in two different ways, which gives an expression for X_{Mach} .

$$N_{\text{real}} = X_{\text{real}} \Delta D_{\text{real}} \quad (4.6.4)$$

$$N_{\text{real}} = X_{\text{Mach}} (\Delta D_{\text{Mach}} - \text{Offset}) \quad (4.6.5)$$

$$X_{\text{Mach}} = \frac{X_{\text{real}} \Delta D_{\text{real}}}{(\Delta D_{\text{Mach}} - \text{Offset})} \quad (4.6.6)$$

The number of workpiece revolutions until contact between roller and workpiece N_{Start} can be expressed as:

$$N_{\text{Start}} = (h_{\text{Start}} + \text{Offset}) X_{\text{Mach}} \quad (4.6.7)$$

The total number of workpiece rotations to be entered into the machine interface N_{Mach} results as:

$$N_{\text{Mach}} = N_{\text{real}} + N_{\text{Start}} \quad (4.6.8)$$

$$N_{\text{Mach}} = X_{\text{real}} \Delta D_{\text{real}} + (h_{\text{Start}} + \text{Offset}) \frac{X_{\text{real}} \Delta D_{\text{real}}}{(\Delta D_{\text{Mach}} - \text{Offset})} \quad (4.6.9)$$

For the machine used in this work the following constants from Table 11 are valid. All other values needed to determine the machine input values using equation 4.6.3 and 4.6.9 are given by the experimental program from chapter 4.4.

K_{Mach}	Offset	h_{Start}
196kN/mm	0.412mm	0.5mm

Table 11: Constants used for machine input correction of stiffness effects

4.7 Cooling effect of the emulsion

During cross rolling the workpiece is rinsed over by an emulsion. This prevents the workpiece from overheating, so that temperature induced fracture phenomena (e.g. blue brittleness) can be avoided. In order to quantify the cooling effect of the emulsion, temperature evolutions over the rolling processes have been measured with a Testo 885 infrared camera. Before, the workpiece's emission coefficient ϵ had to be determined. To do so, a previously rolled workpiece has been heated up to 200°C in an oven. By using a rolled workpiece, a similar surface quality and roughness like in the actual rolling process could be guaranteed. Then a comparison of the workpiece's actual temperature measured with a thermocouple and the one measured by infrared camera has been performed. The emission coefficient of the infrared camera has been adapted until the temperature measured by the infrared camera was equal to the one measured by thermocouple. Like this, the coefficient was determined as roughly 0.5. This value is rather high for a non-oxidized metallic surface (Carvill, 1993), but reasonable since the rolled surface is very rough and the emulsion on the surface additionally increases the emissivity.

In a next step, temperature evolutions of the workpiece in a cross rolling process R3 were measured by the infrared camera, once with emulsion cooling, once without. In case of rolling with emulsion cooling, the measured temperature values are only valid after the emulsion cooling was turned off, which was done right after rolling was finished. The results are given in Figure 54. The cooling effect of the emulsion can be seen to be significant, which is reasonable since the emulsion evaporates on the hot workpiece.

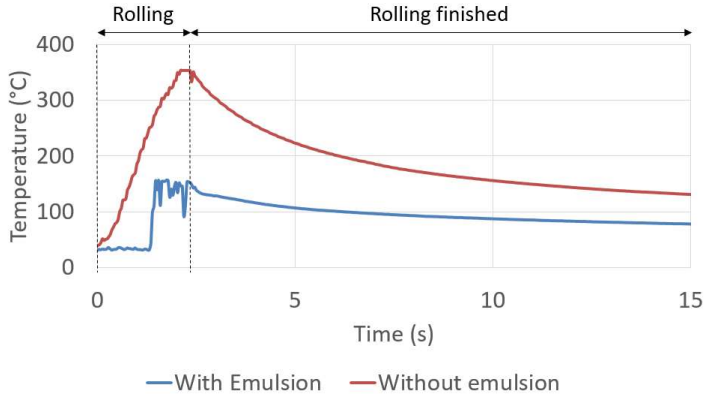


Figure 54: Temperature evolution over a rolling process with and without emulsion cooling

4.8 Experimental fracture results

In this subchapter, the results from fracture investigation are presented for all cross rolling experiments listed in the experimental program. Table 12 gives the smallest ΔD at which the majority of the samples were cracked, the highest ΔD for which the majority of the samples were uncracked, as well as the ΔD of crack initiation calculated according to equation 4.3.1 for each experimental parameter set.

The results show that the width of the rolled notch has a significant influence on the possible ΔD to fracture. For a 20mm wide notch it is as low as 0.325mm, while for the 5mm notch it is close to 4mm. Also the ratio X shows an influence on the diameter reduction to fracture, even though it is not as significant as the one of the roller width. The smaller X , (less rotations per diameter reduction), the higher the possible ΔD to fracture. At an X equal 2Rev./mm the 5mm notch shows a ΔD to fracture of 4.325 while it decreases to $\Delta D = 3.825$ mm for $X = 4$ Rev./mm.

Experimental Code	ΔD cracked	ΔD uncracked	ΔD crack initiation	N at crack
R1	0.35mm	0.30mm	0.325mm	2
R2	0.5mm	0.40mm	0.45mm	2.7
R3	0.92mm	0.88mm	0.9mm	5.4
R4	1.7mm	1.6mm	1.65mm	9.9
R5	2.25mm	2.2mm	2.225mm	4.5
R6	3.95mm	3.7mm	3.825mm	15.3
R7	4.45mm	4.2mm	4.325mm	8.65

Table 12: Core crack initiation diameters for all rolling experiments

After the core crack has initiated, it was found that it grows in size at a variable velocity. When using a wide roller the core crack grew rapidly. For experiment R1, the core crack had reached the surface of the sample (crack class 4) already after an additional 0.4mm of diameter reduction after crack initiation. For the narrow roller R4 in contrast, even after an additional 1.4mm of diameter reduction after crack initiation, the core crack was not visible from the outside of the workpiece. Appendix 9 and Appendix 10 give the detailed investigation results for each experimental parameter set, each diameter reduction as well as the total number of rolled samples.

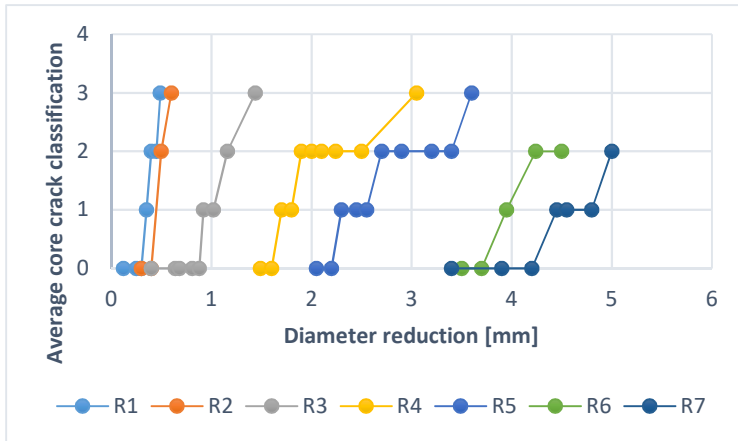


Figure 55: Variable velocities of core crack growth for different rolling experiments

4.9 Repeatability and stability

In this subchapter, the repeatability and stability of the experimental process is discussed. First, the general process repeatability and stability is discussed, followed by an assessment of repeatability of core crack initiation.

4.9.1 Process repeatability and stability

In most cases, for the same machine input, the same ΔD ($\pm 0.02\text{mm}$) was reached in a well reproducible way. Also from one experimental time slot to another on different days and several changeovers of tools and products no evident differences in rolling results could be observed. In rare cases the process lead to noise emission (clicking noises). In case of noise emission, the process was not well repeatable anymore, both with respect to the resulting ΔD and the acting process forces. It was found that this instability was caused by slippage between roller and workpiece. Figure 56 gives possible workpiece surfaces after slippage. While in the left image the surface does not directly indicate that slippage occurred, the shiny workpiece surface in the right image indicates slippage obviously. In general, this phenomenon was observable after having conducted several experiments with the same roller due to wear (loss of roughness of the rollers). It could be eliminated by exchanging or re-sandblasting of the rollers.



Figure 56: Misformed workpiece surfaces due to slippage

The roller segments were produced in a way that several segments can be mounted together and several notches could be rolled into one workpiece in the same process. Since for these combined rollers the material cannot easily flow off axially due to increasing axial compressive stresses over the process, these kind of processes tended to buckle very easily. They were poorly repeatable and unstable and for this reason not evaluated in this study.

4.9.2 Core crack-repeatability

As explained in chapter 4.3 workpieces were rolled down to several different diameters. The crack initiation diameter was determined as in equation 4.3.1. Figure 57 shows the ΔD of core crack initiation, as well as the ΔD for which the very first core crack was observed and the ΔD at which the last uncracked workpiece could be found as red error bars for each experimental code. The core crack occurrence appears well reproducible in general. Also the range of diameter reductions investigated for each parameter set is indicated as black error bars.

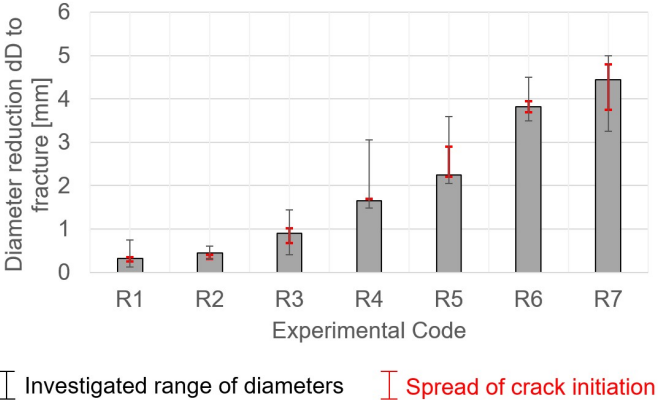


Figure 57: Repeatability of diameter reductions at core crack initiation

5 Simulative analysis of cross rolling experiments

Finite Element Simulations are used in this chapter to approximate the stress- and strain states in the workpiece core for all experiments performed as described in the previous chapter 4. In this chapter five, first the general simulative setup is described (subchapter 5.1), then simulated stress- and strain results are presented (subchapter 5.2), followed by an evaluation of the predictive capabilities of the different fracture criteria in predicting core cracks in cross rolling (subchapter 5.3), and finally the numerical robustness of results is investigated (subchapter 5.4).

The overall goal of this section is to assess, which of the ductile fracture criteria predicts fracture in cross rolling operations best, in the case that they are suitable for this cyclic process.

5.1 Simulative setup and preparation

In this subchapter 5.1. the simulative cross rolling setup is described. This includes the used FE software and calculation procedures, assumed material properties, the used element meshes, and the simulative setup, such as workpiece stabilization and simulative kinematics. Also the simulative workpiece preparation, which is the simulation of the wiredrawing process, will be given.

5.1.1 Basics on simulative procedure

A correct process simulation is necessary to obtain reliable results for the strains and stresses in cross rolling until fracture. These data is the basis for all upcoming evaluations of fracture criteria, which makes a precise simulative setup essential. All simulations have been performed in the commercial Finite element software Simufact.forming v14.0 with implicit time integration. A multistep simulation strategy was employed to also incorporate the effect of the wiredrawing process. This process has been simulated and evaluated first. The output of the wiredrawing simulation (including stress- and strain distribution) was then used as input for all cross rolling simulations.

The tool geometries were constructed in the Commercial CAD software Siemens NX 7.5 and imported into Simufact.forming.

As explained in chapter 2.3.2 an isotropic von Mises yield locus was used. The derived Hensel Spittel flow curve formulation from chapter 3.3.3 served as hardening approximation. Further material properties were taken from the simufact material library (simufact-engineering-GmbH, 2016) of the material 19MnB4 in normalized state and should deviate only slightly from the properties of 20MnB4 in normalized state used in this work. While all of them except density and poisson's ratio are modeled as slightly temperature dependent in the simufact material library, in Table 13 only their values at room temperature are given for informative purposes.

Young's Modulus	Poisson's ratio	Density	Thermal expansion coeff.	Thermal conductivity	Specific heat capacity
213 [GPa]	0.283	7836 [kg/m ³]	$1.12 \cdot 10^{-5}$ [1/K]	46.6 [W/mK]	478 [J/kgK]

Table 13. Material properties of 19MnB4 at room temperature from (simufact-engineering-GmbH, 2016)

5.1.2 Details on cross rolling simulative setup

The cross rolling simulations were set up as 3D simulations in order to be able to model the axial material flow. The workpieces have been meshed with eight-node isoparametric hexahedral brick elements of first order with trilinear interpolation functions. The elements' edge sizes were 0.2mm in the deformed workpiece core (“core mesh”), 0.4mm in the rest of the deformed region (“outer mesh”) and 1.6 mm otherwise. The axial length of the deformed region was defined as the width of the used roller plus 2 mm in each axial direction. Figure 58 shows a cut section of the initial mesh. By increasing the element size outside the deformed region, computational time can be reduced.

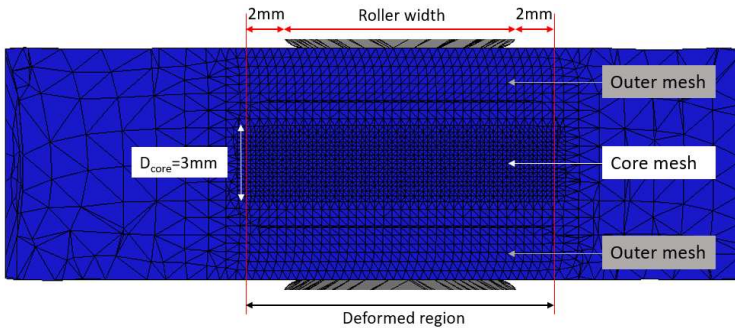


Figure 58: Cut section through the initial workpiece mesh

The “large strain-feature” of the Marc-Solver was used, which in combination with the used element type and a von Mises yield function leads to an updated Lagrangian approach (MSC-Software, 2015). All simulations were set up as elastic-plastic, meaning that although plastic strain are far higher, the elastic deformation is taken into account as well.

The workpiece was remeshed after each 40% increase of plastic strain. Without remeshing, the extreme deformations would have caused heavily distorted elements, falsifying results. Both domain decomposition and shared-memory parallelization were enabled in

order to reduce computational time. In general the simulations were performed at 6 cores. Simulations were executed thermomechanically with a weak thermomechanical coupling. This should be sufficient since no extreme gradients are to be expected. Tools were modeled as rigid without heat conduction.

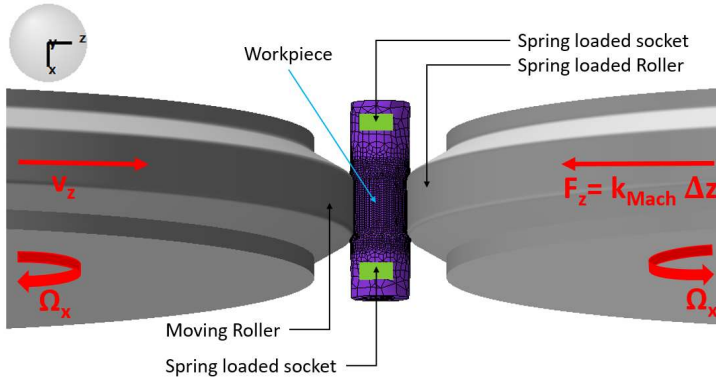


Figure 59: Simulative Cross rolling setup

Figure 59 gives an illustration of the simulative setup. The workpiece is held in position through four spring-loaded sockets with each spring having a stiffness of 20kN/mm, blocking the workpiece's movement in y-direction. In Chapter 4.5 it was observed that the used rolling machine's spring back cannot be neglected. This stiffness of 196kN/mm is incorporated in the simulation through a spring attached to one of the rollers. The cooling effect of the emulsion had to be quantified as well. To do so, the rolling process has been simulated. The heat transfer coefficient to the environment has been adapted in the simulation until the temperature at the end of the simulation was equal to the measured one (see chapter 4.7). The heat transfer coefficient has been found to be roughly 25kW/m²K. This is a fairly high value but reasonable due to the evaporating emulsion rinsing the hot workpiece surface. Coulomb friction coefficient has been assumed to be 0.4 due to sand blasted roller surfaces. The temperature of all tools, workpiece and surroundings at the beginning of the process was set to 20°C.

5.1.3 Simulation of preforming operation

In order to have a correct description of stress- and strain states in the workpiece at the beginning of the cross rolling operation, the wiredrawing process was simulated and the output was taken as input for the rolling simulations. Also there is a certain amount of pre-damage from wiredrawing, which is why the simulation of this process has to be performed.

The drawing process was simulated as a 2D axisymmetric problem without remeshing. The workpiece was meshed with a Quad-Element formulation and an edge size of 0.15mm. Due to a polished drawing die surface, its Coulomb friction coefficient was assumed to be $\mu=0.05$.

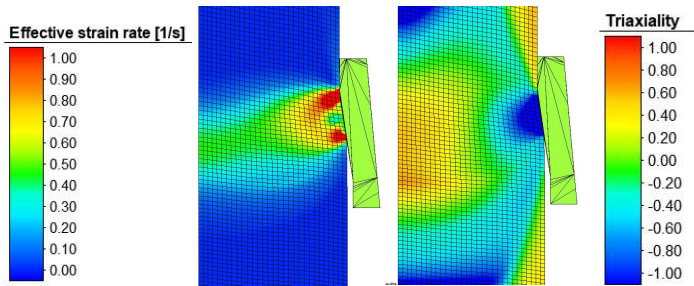


Figure 60 Left: Strain rate distribution at a drawing speed of 10mm/s, Right: Stress triaxiality distribution during drawing

Figure 60 shows the strain rate distribution and stress triaxiality distribution during the forming process. It was found that the deformation in the workpiece core happens at an almost constant stress triaxiality η of 0.54 for the used drawing die and workpiece dimensions. Since the deformation in the core happens under axisymmetric conditions with one principal stress being larger than the two others, the corresponding normalized Lode angle parameter in the core's zone of deformation is $\bar{\theta} = +1$.

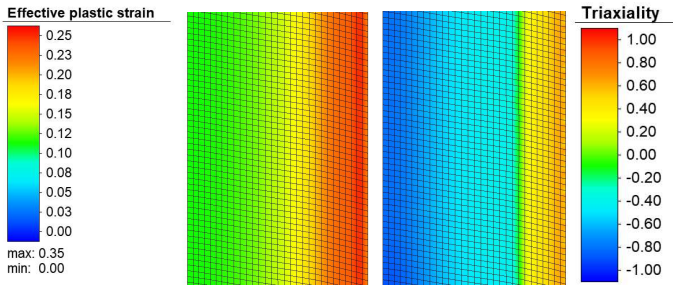


Figure 61: Left: Plastic strain distribution after drawing. Right: Stress triaxiality distribution after drawing

Figure 61 shows strain- and stress triaxiality distribution after the drawing process. It is obvious that the workpiece experiences multiaxial compressive residual stresses in its core ($\eta \cong -0.8$) after drawing. Since the stress state is axisymmetric with one principal stress being smaller than the two others the normalized Lode angle parameter changes its sign with respect to the zone of deformation: $\bar{\theta} = -1$. The resulting core strain after drawing equals 11.1%. This strain is small compared to the ones caused by the subsequent cross rolling.

The resulting output of the drawing simulations as visible in Figure 61 was rotated around its axis to obtain a 3D workpiece for the following cross rolling simulations. The temperature data was deleted in order to restart the cross rolling process at room temperature.

5.2 Simulated process variables

In this subchapter, all relevant simulated results except damage are presented. This includes a comparison between force and torque evolutions from experiment and simulation, simulated stress and strain distribution over the workpiece and at the critical particle, as well as their dependency on the variable parameters roller width and ratio X. Also the simulated temperature evolutions will be given. On the basis of this data, in the next subchapter 5.3. the calibrated fracture criteria will be evaluated in cross rolling operations.

5.2.1 Validation of used hardening model

Since the flow stress distribution over the workpiece determines the distribution of plastic material flow over the workpiece, it is important to verify the used hardening model process specifically. Furthermore, since the cross rolling process is partially cyclic it is important to validate the purely isotropic hardening model approach. One way to do this is a comparison of the experimental and the simulated evolution of force and torque over the process. These evolutions over the process are given in Figure 62 for three exemplary cross rolling processes. A very good agreement of force and torque evolutions can be seen, which justifies the further use of the von Mises yield locus in combination with the derived hardening approximation.

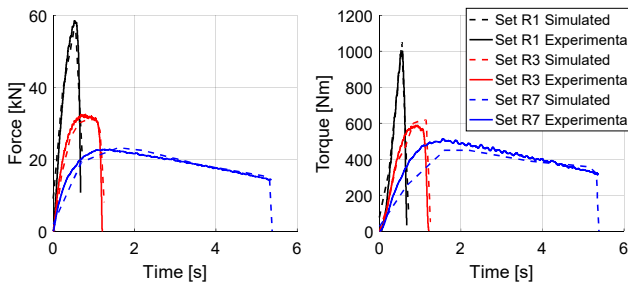


Figure 62: Simulated and experimental force and torque evolutions in cross rolling experiments

5.2.2 Analysis of stress- and strain distribution

5.2.2.1 Strain distribution

Figure 63 shows the plastic strain and strain rate distribution of a cut section of a simulation of rolling experiment R3. The analysis of material flow distribution over the workpiece shows that by far the highest strain is induced at outer radii (position P1) where the roller is in contact with the workpiece. Another local maximum of plastic strain can be found in the workpiece core in the middle of the rolled notch (position P2). Outside the rolled notch in the core (P3) no plastic strain is accumulated.

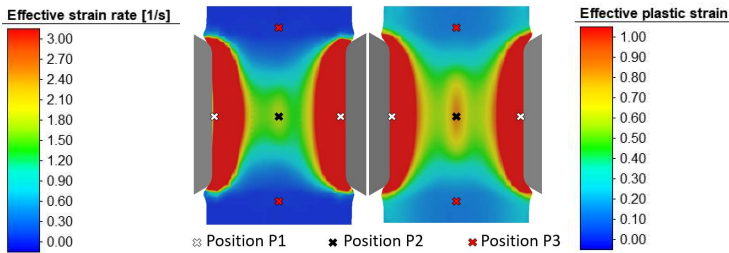


Figure 63: Plastic strain and plastic strain rate distribution in a cut section through simulation of R3 shortly before fracture

The ratio Y is defined here as plastic strain accumulated in the workpiece core (position P2) over plastic strain at the outer radius (position P1). It significantly depends on the roller width and also on the ratio X (equation 4.4.1) as shown in Figure 64. Y in Figure 64 was evaluated shortly before experimental fracture was observed. The illustration shows that the wider the roller, the more strain tends to develop in the workpiece core. Figure 64 right shows that the more revolutions the workpiece experiences to a certain diameter reduction the higher the strain at the outer radius relative to the core strain.

$$Y = \frac{\varepsilon_{core}}{\varepsilon_{outer\ radius}} \quad (5.2.1)$$

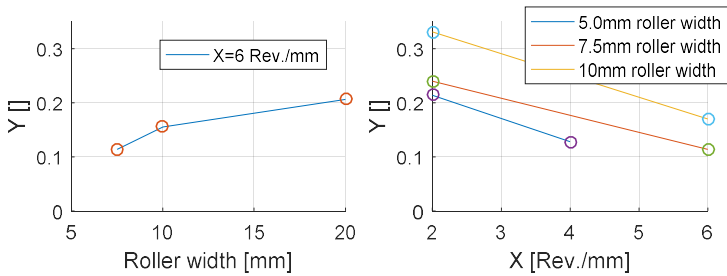


Figure 64: Ratio Y of core strain over strain at the outer diameter in function of process parameters

Remark: Simulations with other materials have shown that Y also greatly depends on the material's hardening curve, namely the higher the slope of the hardening curve the higher Y . The same finding is also presented in chapter 5.4.4.

5.2.2.2 Stress distribution

Figure 65 gives the distribution of principal stresses over a cut section of the workpiece during a simulation of the R3 rolling process shortly before fracture. It can be seen that in the contact region between roller and workpiece (P1) the workpiece experiences strong three dimensional compressive stresses. The core of the workpiece in the middle of the rolled notch (P2) experiences two tensile principal stresses and one small compressive principal stress. Outside the rolled notch on the core there are particles (P3) on the workpiece core that experience an even more intense tensile stress state with all three principal stresses being positive. In this point, since all principal stresses are similarly high and positive, according to equation 2.2.12, the equivalent stress is low and no plastic material flow occurs (see Figure 63).

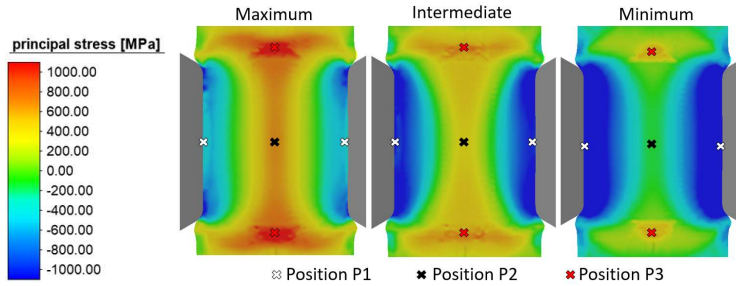


Figure 65: Distribution of principal stresses over the workpiece R3. Left: Maximum, middle: Intermediate, Right: Minimum principal stress

This distribution of principal stresses gives the stress triaxiality distribution shown in Figure 66 left with strong compressive regions near the surface (position P1), a strong tensile region outside the deformed region in the core (position P3) and an intermediate triaxiality ($\eta=0.2$ to 0.6) region on the core in the deformed region (position P2).

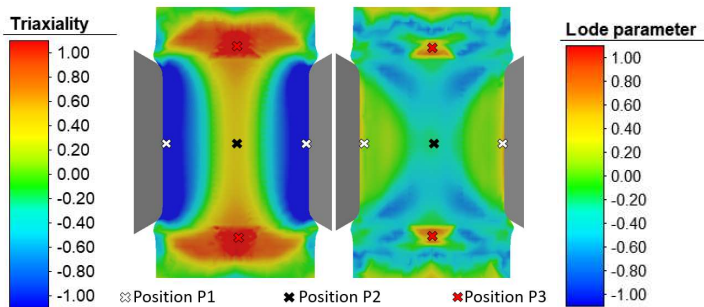


Figure 66: Left: Distribution of stress triaxiality, Right: Distribution of normalized Lode angle parameter in a cut section over the workpiece R3

5.2.3 Definition of the critical particle

It is known from radiographic measurements that the crack initiates at a position that is radially located on the workpiece core, axially in the center of the rolled notch. The location of the critical particle is shown as a red cross in Figure 67. All following analyses will be performed at this position. In the previous subchapter this position was referred to as position P2. It was already shown that at this position, there is a local maximum in strain and at the same time a positive tensile stress triaxiality. This particle's stress and strain states will be investigated more detailedly over the rolling process in the upcoming subchapters.

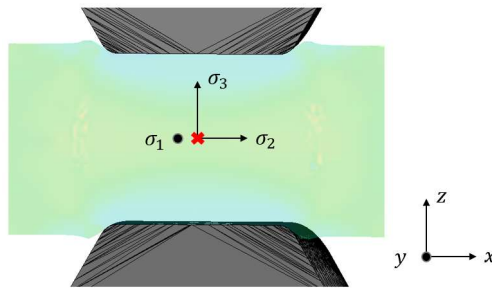


Figure 67: Position of critical particle and orientation of principal stresses

The illustration also gives the orientation of the principal stresses in the critical point with respect to a stationary coordinate system. The directions of principal stresses almost coincide with the Cartesian coordinate system with small angle deviations due to ovalisation of the workpiece. The minimum principal stress in the core is acting in a direction that only deviates slightly from the z -direction, the intermediate principal stress corresponds to the x -direction and the maximum principal stress corresponds to the y -direction.

5.2.4 Stress and strain states at the critical particle

Since the critical point is where the crack will initiate, its stress and strain states are of major importance to the prediction of crack initiation. The simulated principal stress values at the critical particle at a plastic strain of 100% are visible in Mohr's stress circles for the different roller widths and X values in Figure 68. The wider the roller the higher are all principal stresses. While for the 20mm roller there is an almost three-dimensional tensile stress state, for the narrower rollers the minimum principal stress becomes more and more compressive.

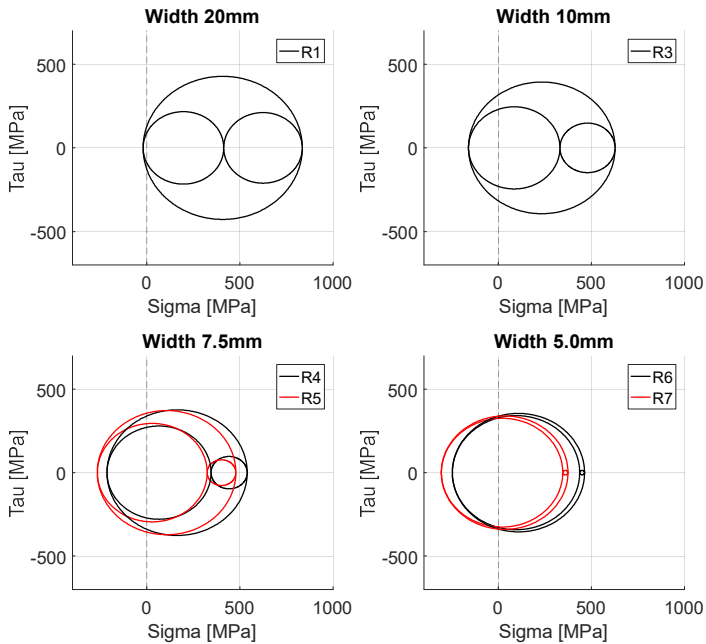


Figure 68: Mohr's stress circles at the critical particle for different experiments at a plastic strain of 100%

To predict ductile fracture not only the final state is relevant but the whole path to fracture. For this reason, the critical particle's stress state evolutions to fracture are given in a next step. In order to be able to better interpret the results in terms of ductile fracture research, the stress state previously defined by the principal stresses will from now on be defined in the mixed stress strain space $\{\bar{\epsilon}, \eta, \bar{\theta}\}$. Figure 69 shows the evolution of stress triaxiality and Normalized Lode angle parameter as a function of the plastic strain in the core until experimental fracture occurred (experimental results from Table 12). The strain from wiredrawing is subtracted here.

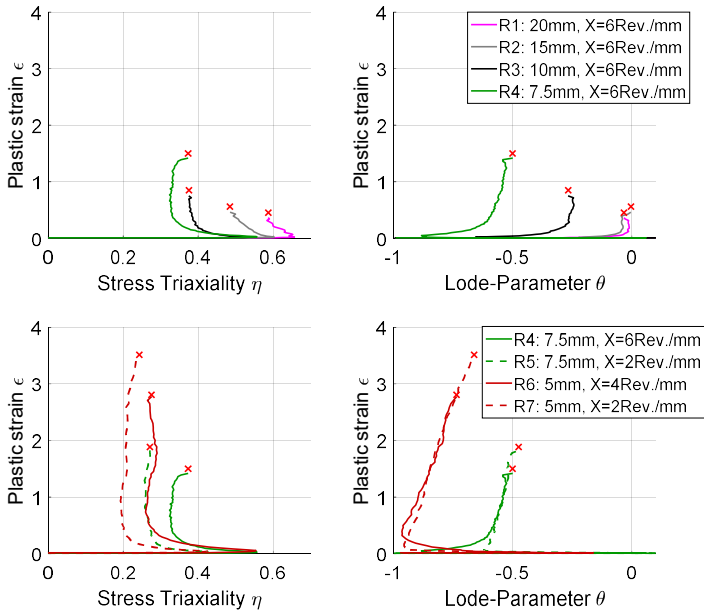


Figure 69: Evolution of stress state in the workpiece core for various cross rolling experiments

The upper row in Figure 69 shows that wider rollers lead to increasing triaxiality and decreasing norm of the Lode angle parameter in the workpiece core. Increasing the ratio X increases stress triaxiality with

minor influence on the Lode angle parameter (see bottom row in Figure 69). While most processes do not show significant variation of stress triaxiality and Lode angle parameter over the process, the ones with the narrow roller of 5.0mm show a variation in the normalized Lode angle parameter of 0.25 to 0.40. The red crosses indicate the point at which each simulation reached the diameter reduction $\Delta D_{\text{crack-init}}$ at which the experimental crack initiation was observed.

In order to be able to reduce the paths to a single data point the linear averaging equation 2.5.28 is used as it was done for the experiments from chapter 3.4. It is well known that this procedure is a simplification. In this context it is applicable because firstly the stress state doesn't change very much over the process for most experiments except the vary narrow rollers and secondly the averaged value is only for informative purposes and illustration in Figure 70. The results are given in Table 14.

Parameter set Number	ϵ_f	$\eta_{\text{Av,lin}}$	$\bar{\theta}_{\text{Av,lin}}$	$\dot{\epsilon}_{\text{Av,lin}}$
R1	45%	0.62	-0.02	0.80/s
R2	56%	0.54	-0.04	0.99/s
R3	85%	0.41	-0.33	0.75/s
R4	150%	0.34	-0.59	0.68/s
R5	188%	0.28	-0.57	0.65/s
R6	281%	0.29	-0.84	0.66/s
R7	351%	0.22	-0.78	0.57/s

Table 14: Averaged stress states and fracture strains of all cross rolling experiments processes

The simulated fracture strains are also given in Table 14. They were determined by simulating each cross rolling experiment until $\Delta D_{\text{crack-init}}$ was reached. The strain reached from wiredrawing is subtracted in these values. For the wide rollers the resulting diameter reductions to fracture are small (0.32mm). This makes it necessary to not only simulate the part of the process that actually reduces the diameter (Phase 2 in Figure 53) but also the part of the rolling process in which

the rollers are pulled out of the workpiece (Phase 3 in Figure 53) to obtain correct core strains. Due to machine inertia and the energy stored in the machine due to elasticity, the pull out process doesn't happen instantly. To do so, the simulative pull-out parameters were adapted until the measured force- and torque curves equaled the simulated ones in the pull out part of the process.

Also the average strain rate is given in the Table 14. Since the strain rate is between 0.5/s and 1/s for all experiments and since strain rate didn't show an influence on fracture behavior in torsion tests, strain rate should not influence the results with respect to fracture.

5.2.5 Comparison with standard experiments

In order to be able to compare these newly proposed experiments with the standard experiments performed in chapter 3.4 for calibration and verification, the experiments are plotted in Figure 70 in the two-dimensional space of η and $\bar{\theta}$ in comparison to standard torsion and tensile experiments. It can be seen that the cross rolling experiments' averaged stress states are located far from the standard experiments in this space, especially with respect to the normalized Lode angle parameter. For this reason the evaluation of the different fracture criteria's accuracy with respect to the new cross rolling processes is revealing.

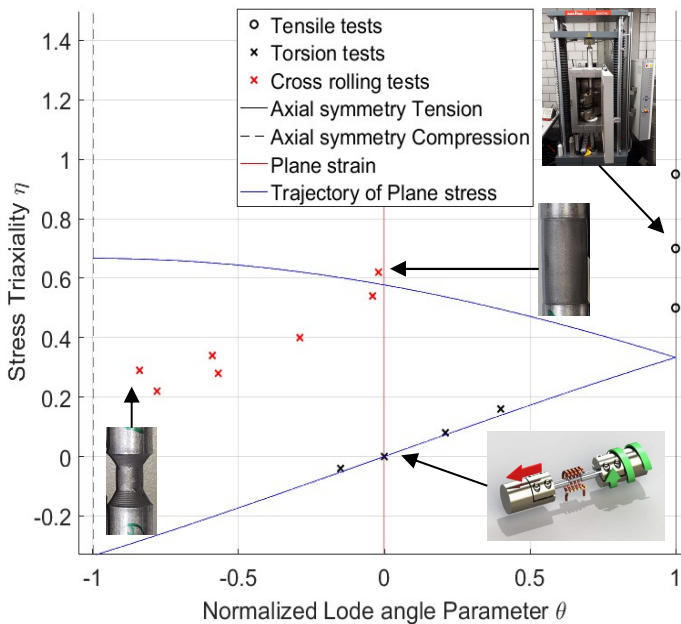


Figure 70: Comparison of averaged stress states in the workpiece core in cross rolling operations with averaged stress states in tension and torsion experiments

5.2.6 Repeatability

While Table 14 gives the fracture strains corresponding to the average crack initiation diameters, Figure 71 illustrates these strains together with the spread of fracture strains obtained from repeating the experiments several times as red error bars. The lower bar end corresponds to the fracture strain of the first observed cracked sample, while the upper bar end corresponds to the fracture strain of the last uncracked sample observed. The figure is equivalent to Figure 57, showing the simulated fracture strains instead of the diameter reductions to fracture.

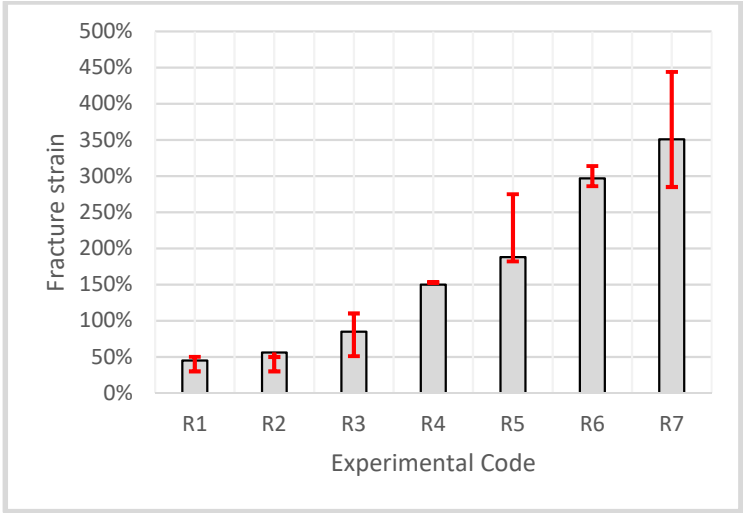


Figure 71: Scattering of fracture strain at core crack initiation

5.2.7 Analysis of workpiece temperature distribution

The temperature and its distribution over the workpiece in cross rolling operations is of interest for two reasons. Firstly, the temperature gradient over the workpiece influences the strain rate field over the workpiece. Secondly, it was found that the steel used in this study shows a blue brittle behavior for temperatures above 250°C that should be avoided in order to guarantee high ductility.

Since the processes all happen fast with strain rates around $0.5/\text{s}$ and $1/\text{s}$ in the core and even much higher at the outer diameters, the processes are far from reaching a thermal equilibrium. Instead, there are heavy temperature gradients over the workpiece. Additionally, the workpiece is cooled by emulsion from the outside, which means that all heat produced by deformation has to be conducted to the surface in order to be dissipated from the workpiece.

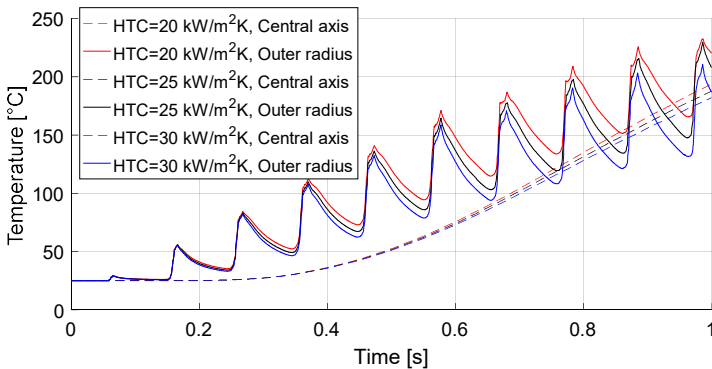


Figure 72: Simulated temperature evolution in center and outer radius for experiment R3 and varying heat transfer coefficients

Cross rolling experiment R3 was simulated with three varying heat transfer coefficients to environment (HTC). The temperature evolutions at the core (position P2 in Figure 66) and the outer radius

(position P1 in Figure 66) for the various HTC's are given in Figure 72. Simulative results show that the core's temperature is monotonically increasing. This increase is due to heat produced from plastic deformation in the core and heat conduction from the outer radii to the core. In contrast, the outer diameter's temperature is jumping up while being in contact with the roller due to a jump in plastic strain, followed by a slower decline of temperature. This decline is due to heat conduction into the workpiece and heat dissipation to the environment. While the heat dissipation depends on the HTC used and the current surface temperature, the heat conduction depends on the material's heat conductivity, and existing temperature gradients over the workpiece.

In the beginning of the process, the outer diameter always heats up faster than the central axis and the heat flux is from outer diameter to the center. Later in the process the temperature gradient can be vice-versa. This is due to the emulsion, cooling the workpiece from its surface while heat being produced in the core due to plastic deformation.

In order to exclude effects from blue brittleness on the fracture results measured, all experiments were previously simulated and the rollers' rotational velocity Ω was chosen such that the simulated temperature in the core stayed below 250°C for all experiments. Table 15 gives the simulated maximum core temperatures at the instants of fracture.

Experimental code	R1	R2	R3	R4	R5	R6	R7
T_{\max} in core [°C]	95	105	200	245	140	195	150

Table 15: Simulated maximum core temperatures in rolling experiments

To ensure that the workpieces didn't heat up to temperatures higher than 250°C during rolling, each workpiece was checked for oxide layer caused discolorations after the rolling process. In case of surface temperatures higher than 250°C the rolled carbon steel sample surface should have shown a red, blue or grey discoloration (Colpaert, 2018), which was not the case for any of the samples.

5.3 Virtual prediction of core crack initiation

Having established a virtual process model in the previous subchapter, in this section the previously calibrated ductile fracture criteria from chapter 3.5 will be applied to first wiredrawing and then cross rolling simulations. Both linear and quadratic damage accumulation assumptions are evaluated. The damage is first evaluated over the workpiece cross section and then in detail for all rolling experiments at the critical particle in the core. The robustness of the criteria in predicting core crack initiation is evaluated and finally, the prediction of crack initiation under the presence of material data scattering is discussed shortly.

In order to be able to illustrate the criteria's damage field over the workpiece, the fracture criteria have been implemented into a ueloop subroutine for the commercial finite element software Simufact.Forming and a udamag subroutine for the finite element software DEFORM-3D.

5.3.1 On the variation of stress state over the process

In order to be able to predict ductile damage in a true forming process, it is of major importance how the non-constancy of stress states over the process is incorporated in the damage model. This was previously discussed in chapter 2.5.7. Most commonly, the damage will be accumulated according to equation 2.5.29. In this study both a linear ($n=1$) and a nonlinear quadratic ($n=2$) damage accumulation assumption will be evaluated for the cross rolling experiments. D is used as a damage indicator variable, which means that there is no coupling between damage and the constitutive relations. Once the damage indicator D reaches 100%, the crack should occur.

5.3.2 Preforming operation

Since damage is accumulated over all processes, the damage accumulated during the wiredrawing process has to be calculated first. Figure 73 shows the distribution of damage, calculated according to the linear damage accumulation rule in combination with the Mohr-Coulomb failure criterion. The damage is nearly 8.9% over a wide range of radii. The maximum damage is obtained on the workpiece's central axis.

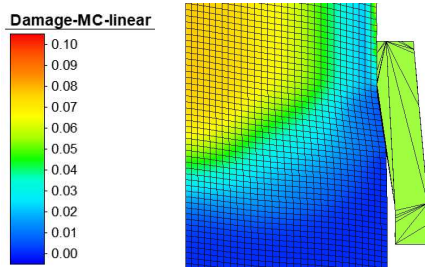


Figure 73: Damage from wiredrawing of MC criterion, accumulated linearly

Table 16 gives the calculated damage values for all fracture criteria and damage accumulation rules. All damages calculated under the assumption of nonlinear damage accumulation are significantly smaller than the linear accumulated damage values. This is in good agreement with the theory of nonlinear damage accumulation (see also Figure 18).

Linear Accumulation	Damage JC	12.80%
	Damage MC	8.90%
	Damage HC	9.56%
Quadratic Accumulation	Damage JC	1.53%
	Damage MC	0.57%
	Damage HC	0.63%

Table 16: Accumulated damage in wiredrawing (on central axis) for different fracture criteria

5.3.3 Damage distribution over the workpiece

As defined in Figure 66, mostly three positions in the workpiece are of interest for ductile fracture prediction. Position P1 shows the highest strains over the workpiece but at the same time a very low stress triaxiality. Due to the strongly compressive state, the crack doesn't initiate here. Position P3 shows a very strong multiaxial tensile state. Since no plastic strain is accumulated at this position though, the crack will not initiate at this position either. Position P2 shows a local maximum of plastic strain at an intermediate positive stress triaxiality. It is known from crack investigation that the crack will initiate at this position.

Simulating the cross rolling experiments, it was found that all fracture criteria show a local maximum of damage at position P2. For almost all simulated experiments the damage maximum at position P2 is also the global maximum over the workpiece, meaning the critical point (see Figure 74).

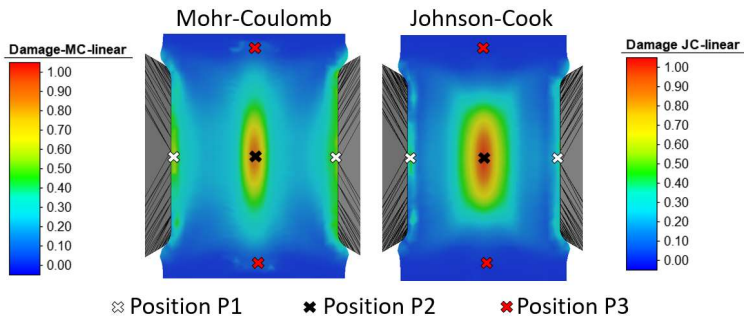


Figure 74: Damage distribution over workpiece R3 at instant of fracture

Only for selected experiments with narrow rollers (R4, R6, R7), it was found that the criteria indicate the outer diameter (P1) to be more critical, meaning a higher damage value, than at P2 (see Figure 75 left). This doesn't indicate a bad accuracy of the criteria for the

prediction of core crack initiation, though. Instead, it is an indication for a slightly underestimating extrapolation of fracture strains for very low compressive stress triaxialities. Since the criteria are calibrated from 6 positive stress state points and only one slightly negative one, this extrapolation error can occur.

One way to incorporate the steep increase of ductility for negative stress triaxiality is to make use of the concept of the cutoff stress triaxiality. It claims that below a theoretical cutoff stress triaxiality of $-1/3$ no damage is accumulated at all (Bao & Wierzbicki, 2005). Applying this concept to the damage accumulation for the cross rolling experiments, only the simulation of experiment R7 gives higher damage at P1 than at P2 (see Figure 75 right). For this reason the use of the cutoff stress triaxiality appears reasonable in damage prediction for cross rolling experiments and is applied to simulations in this study.

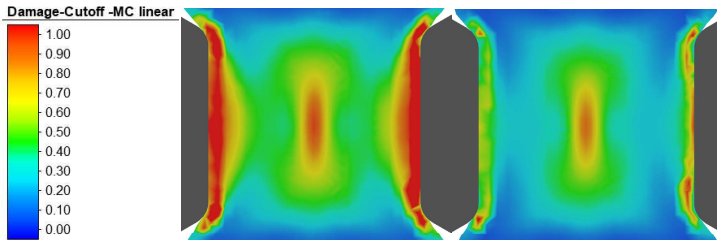


Figure 75: MC linear damage distribution over cutsection of experiment R4. Left: Without cutoff triaxiality, Right: With cutoff triaxiality

5.3.4 Fracture prediction (linear accumulation)

The different fracture criteria are evaluated at the critical particle for all different cross rolling experiments here. This subchapter is applying a linear damage accumulation. This comes with the use of the fracture criteria calibrated from the linear stress averages of tension and torsion experiments (see chapter 3.5). Each experiment has been simulated applying the different fracture criteria as subroutines and the damage values at the diameters of crack initiation were read out of the simulations. Figure 76 gives the damages at the instant of crack initiation at the critical particle.

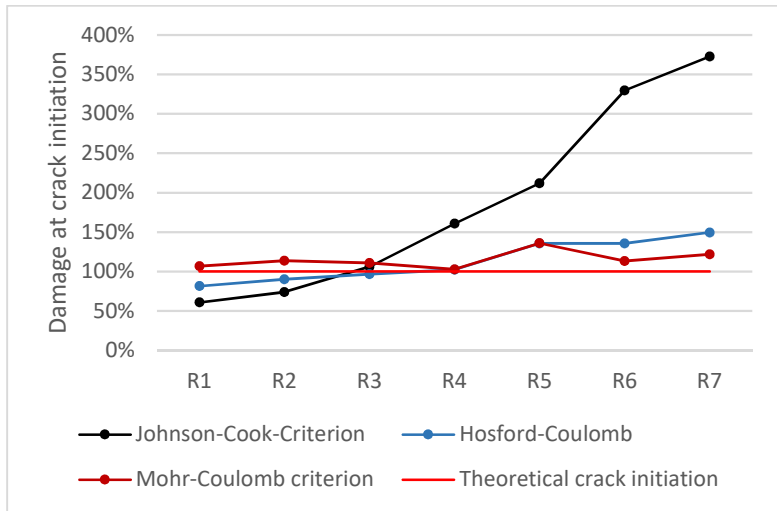


Figure 76: Linearly accumulated damage at diameter of crack initiation for all rolling experiments for the different fracture criteria

The given damage values include the damage accumulated in wiredrawing. For that reason the theoretical damage value of crack initiation is at $D_{crit}=100\%$. It is obvious that the linearly accumulated damage after the MC criterion at the instant of crack initiation meets the theoretical damage value of crack initiation (100%) very well for

most rolling experiments. The average error is only 15%. In contrast, the damage after the linear accumulated JC criterion significantly deviates from the 100%. While for the wide rollers (R1, R2) the JC damage at crack initiation is as low as only 50%, for the narrow rollers it goes up to 490%. The HC-model's accuracy is not as good as the MC's accuracy but far better than the JC's accuracy in predicting the damage at the diameter of crack initiation.

Assessing the producibility of a cross rolled product, more important than the error in accumulated damage value D at the critical particle between model and experiment is the error in predicted and experimentally observed diameter reduction to fracture. Due to a steeper gradient in damage value D towards the end of the rolling process, even for damage values that deviate significantly from 100%, the prediction of possible diameter reduction to fracture can be fairly accurate. For this reason, Figure 77 gives the experimentally observed diameter reduction to fracture in comparison to the diameter reduction at which the damage at the critical particle reached 100% including damage from wiredrawing for each criterion.

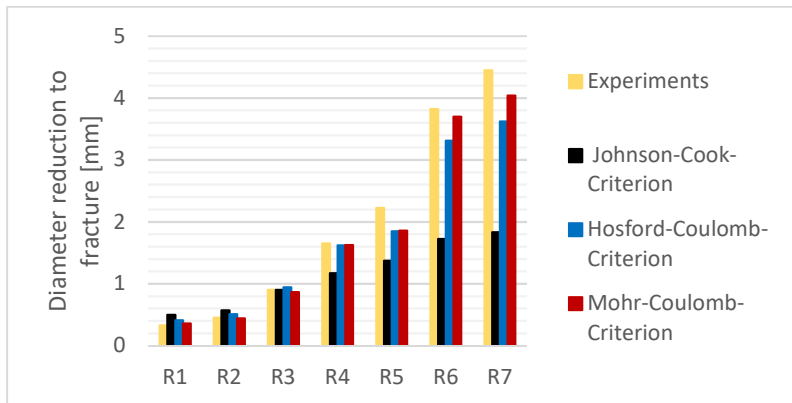


Figure 77: Predicted and experimentally observed diameter reductions to fracture

To quantify the accuracy of the predicted diameter reduction to fracture the relative error in predicted diameter reduction to fracture z is introduced and defined as given in equation 5.3.1.

$$z = \left| \frac{dD_{Fracture, Model} - dD_{Fracture, Experiment}}{dD_{Fracture, Experiment}} \right| \quad (5.3.1)$$

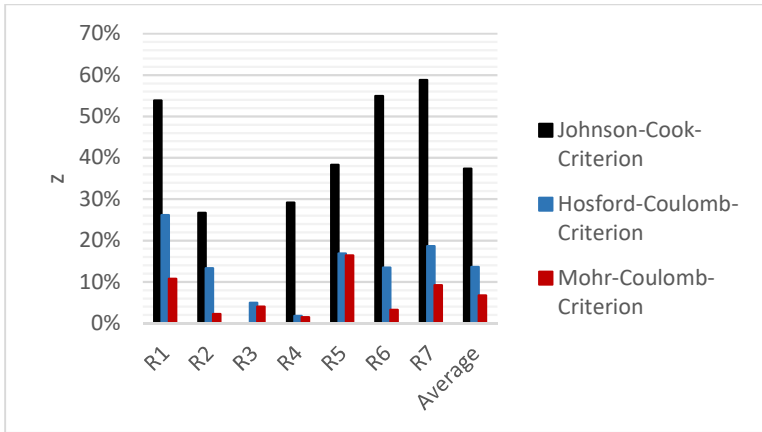


Figure 78: Relative error in prediction of diameter reduction to fracture for all criteria

While the average deviation of calculated damage from 100% was 15% in case of the MC criterion, the average deviation of predicted diameter reduction to fracture z is even lower with only 7% in case of the MC model. The JC model shows the highest deviations with an average error in predicted diameter reduction to fracture z of 37%.

5.3.5 Fracture prediction (quadratic accumulation)

Figure 79 gives the quadratically accumulated damages at the instant of crack initiation according to equation 2.5.29 with $n=2$. Comparing Figure 76 and Figure 79 it is found that the deviations from the critical damage value of 100% are far higher in case of quadratic damage accumulation for all criteria. For the MC criterion the average deviation from 100% is 21% in case of quadratic accumulation and 15% in case of linear accumulation. For the HC and JC criteria these differences are even far higher.

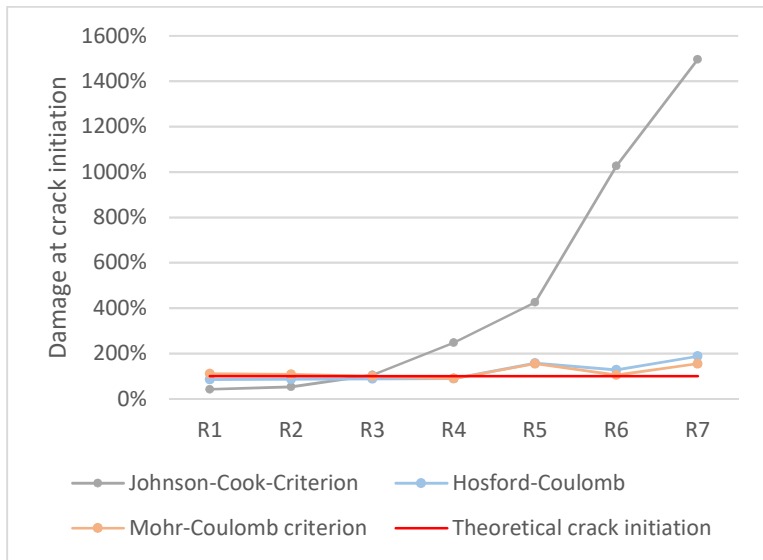


Figure 79: Quadratically accumulated damage at crack initiation for all rolling experiments for the different fracture criteria

It was investigated why the errors in damage prediction assuming some small modelling uncertainties are far higher in case of a quadratic damage accumulation instead of linear accumulation. Figure 80 illustrates how damage is accumulated with plastic strain for both linear and quadratic damage accumulation assumptions. In case of a

quadratic assumption the slope of the damage curve close to $D_{crit}=100\%$ is much steeper than in case of a linear accumulation assumption. In case of slight deviations between predicted fracture strain and actual strain at the instant of experimental fracture this leads to higher deviations in the quadratically accumulated damage from the theoretical $D_{crit}=100\%$. In case that there is a difference of 25% between observed experimental and model-predicted fracture strain, the deviation in linearly accumulated damage from 100% would be 25%, but the deviation in quadratically accumulated damage would be 44%. In that way, the nonlinear damage accumulation assumption amplifies errors in failure prediction. Although Figure 80 illustrates this only for a negative error, meaning experimental cracking before model predicted cracking, the same also hold for positive errors, meaning experimental cracking after model predicted cracking.

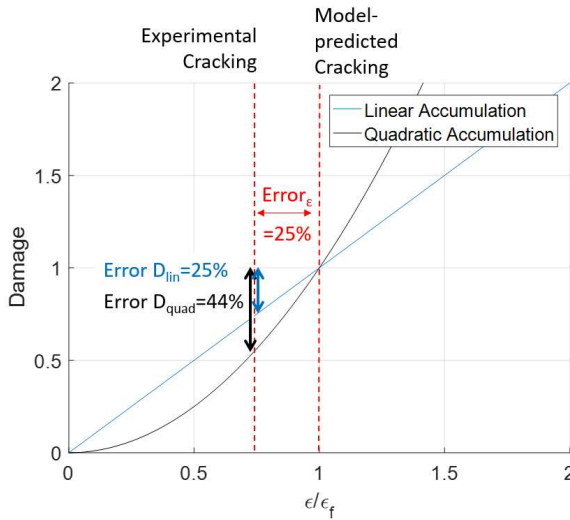


Figure 80: The error amplifying effect of nonlinear damage accumulation

Due to this amplification of modelling errors, the concept of nonlinear damage accumulation will not be followed further in this study.

5.3.6 Evaluation of robustness of fracture prediction

In this subchapter the robustness of the fracture criteria in predicting the correct fracture strains for rolling operations is investigated. This is done in a procedure analogous to the one introduced in chapter 3.5.3. The number of experiments used for calibration is reduced from seven to four. Under the constraint of taking at least one experiment from tension and one from torsion experiments this leaves 34 combinations of tension and torsion experiments for calibration. 34 parameter sets were identified for each fracture criterion as in chapter 3.5.3. For every single parameter set the absolute error in predicting the fracture strains of the seven cross rolling experiments are calculated according to equation 3.5.7. Then the maximum error of fracture strain prediction is determined for each criterion for each cross rolling experiment over all 34 parameter sets according to equation 3.5.8. The results are given in Figure 81.

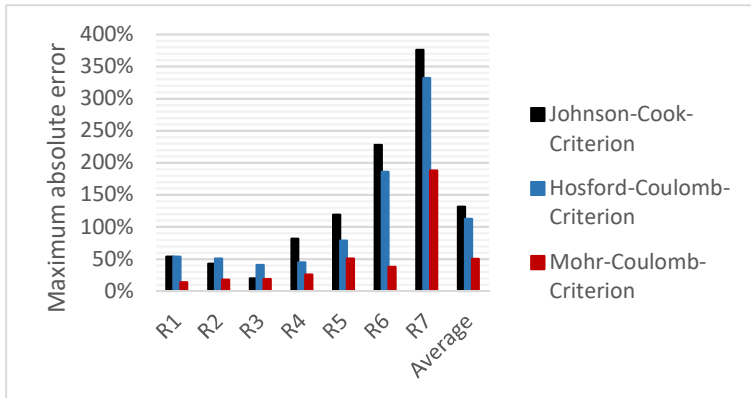


Figure 81: Maximum absolute errors in fracture strain prediction using criteria calibrated from reduced number of experiments

In accordance with the findings from chapter 3.5.3 the MC fracture criterion is found to be by far the most robust to a reduced number of experiments used for calibration due to the smallest maximum errors.

5.3.7 Incorporating material data scattering

The previous investigations were conducted under the strong assumption that failure will always occur at the same diameter reduction, when keeping all parameters unchanged. Experiments though have shown that the diameter of failure initiation shows some scattering when repeating the experiments (see Appendix 9 and Appendix 10 for detailed results), which is likely to be caused by scattering of material properties. All the previous investigations defined the diameter of crack initiation as the diameter where 50% of the workpieces were cracked. This simplification will be loosened in this section. To do this, the respective damage value according to the linearly accumulated MC criterion was determined for every single experiment and every diameter reduction. Then it was investigated what percentage of workpieces showed core cracks for a given damage value. Damage ranges were defined and the data points within each range were summed up.

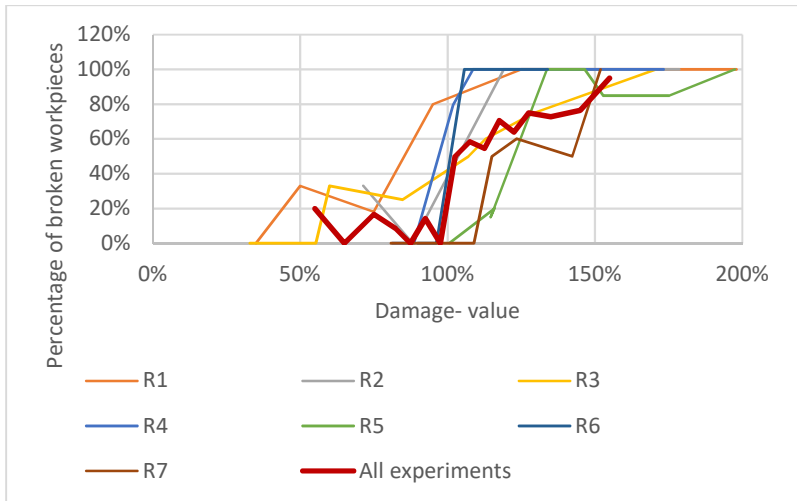


Figure 82: Scattering of crack initiation for all rolling experiments with respect to MC damage values

Figure 82 gives the percentage of broken workpieces as a function of the respective damage range for all different rolling processes. It was found that some cross rolling experiments showed less scattering, such as experiment R6 that increases from 0% directly to 100% of broken workpieces. Other experiments like R3 showed clearly more scattering. Considering all experiments performed, for damage values smaller than 1, the number of broken workpieces is between 0% and 20%, then it clearly jumps up to 50% at $D=1$, then increases and approaches 100% at $D=1.6$.

This figure illustrates the partially probabilistic nature of the damage initiation. To be able to reduce the probability of workpiece defects, in actual production process design a certain safety factor should be employed. The question of how to choose it cannot be answered in this thesis since it depends on too many individual factors, such as the producing company's quality promises and consequences of workpiece failure. From the data in Figure 82 it appears that increasing the safety factor doesn't reduce the probability of core cracks in the range of $D= 0.5$ to 0.95 . This is probably due to the limited number of samples used for generation of the graph ($n=225$). It is likely that the shape of the graph would appear more smoothly when increasing the number of samples. For this reason the following failure criterion is proposed for an actual production process design, where S_f is the safety factor.

$$D_{crit, safe} = \frac{100\%}{S_f} \quad (5.3.2)$$

This approach is equivalent to an down-shifting of the failure surface $\varepsilon_f = f(\eta, \theta)$ in the mixed stress strain space.

5.3.8 Summary on core crack prediction

An accurate virtual fracture prediction with modern ductile fracture criteria could be achieved. Like this, it was possible to predict the diameter reduction to fracture with an average error of 7% under varying cross rolling process parameters. While all investigated criteria were able to predict the workpiece core as critical for most rolling test cases, the rather easy and physically reasonable MC fracture criterion was able to predict the onset of ductile core cracking with the lowest forecasting errors. Although the HC criterion is meant to be an extension of the MC criterion, for the application investigated in this study, it didn't achieve better accuracy. It was also found to deliver less robust results under a reduced number of experiments used for calibration. The worst forecast quality for the investigated process was found for the Lode parameter independent JC criterion.

A linear damage accumulation rule achieved good accuracy in fracture prediction, while the quadratic damage accumulation approach amplifies modelling errors, leading to high deviations of accumulated damage at the instant of core crack initiation from the theoretical critical damage of 100%. For this reason a linear damage accumulation approach is recommended.

To incorporate scattering of material and process parameters, the use of a safety factor is recommended in industrial application of the derived criterion.

5.4 Analysis of robustness of numerical results

The evolutions of stress- and strain states over the cross rolling processes were obtained from numerical simulations. It is essential for the correctness of the fracture prediction that the results from numerical simulations are as precise as possible. There are numerous possible reasons for deviations between cross rolling simulations and real experiments. Only the most relevant ones are listed here:

- Machine elasticity
- Incorrect friction modelling
- Incorrect modelling of the workpiece cooling
- Discretization error due to workpiece discretization
- Incorrect extrapolation of the hardening curve
- Etc.

While the machine elasticity's effect has been incorporated in the simulations as shown in chapter 5.1, the other factors' influence on the results of the numerical simulation are investigated in this section. To do so, relevant process variables were varied and the process R3 was re-simulated under these varying parameters until $D_{\text{crack-init}}$ was reached in simulation in order to investigate the sensitivity of the numerical results on each process variable. This will give an understanding of which effects have a great influence on the outcome of the numerical cross rolling simulations. This knowledge will allow assessing the reliability of the simulated results. Figure 83 gives a summary of the simulated results under varying parameters. In the following section each influencing parameter's effect will be briefly discussed and details will be given.

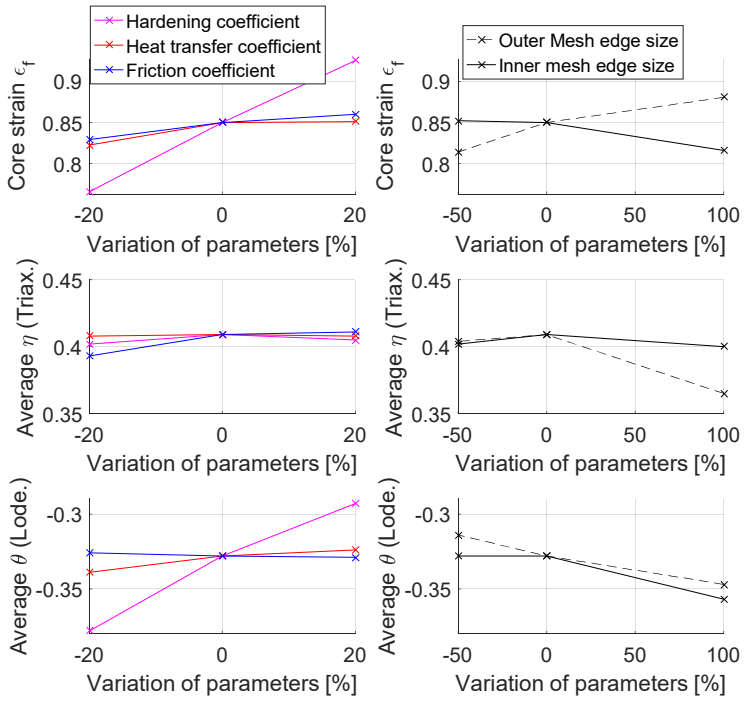


Figure 83: Sensitivity of results of cross rolling simulation R3 to varying simulative parameters

5.4.1 Modelling of friction

Since there will always be variations in the actual friction coefficient of the roller because its surface is sandblasted manually it is important to understand how varying friction coefficients influence the simulative cross rolling results.

(John, 2018) investigated the friction coefficient μ in a cross rolling process for the same workpiece material and the same sandblasted roller surface condition given in this study. He did this in a rolling process with a high speed camera by determining the starting point of workpiece slippage. With this procedure he determined the friction coefficient μ to be in a range from 0.3 to 0.4 under the given conditions. (Dong et al., 2000) came to a similar conclusion for a given cross wedge rolling application, stating that the critical friction coefficient at which slippage occurs is $\mu=0.3$. Based on these two findings and to ensure that no slippage occurs the standard friction coefficient μ was chosen to be 0.4 for the simulations in chapters 5.1 to 5.3.

To investigate the friction's influence on simulated results in the core, the same rolling process R3 has been simulated with friction coefficients of $\mu_1=0.32$, $\mu_2=0.40$ and $\mu_3=0.48$. Figure 83 gives the results. It can be seen that the core strain increases slightly under increasing friction. This is reasonable since the material is avoided from flowing in the workpiece contact zone leading to a slightly increased core strain. An increased friction coefficient also slightly increases core triaxiality while decreasing the normalized Lode angle parameter. Although there are some effects of this parameter, the effects on the simulative results are very small.

5.4.2 Modeling of heat transfer

The emulsion cooling of the workpiece is incorporated in the simulation through the increased heat transfer coefficient to the environment of $25\text{W/m}^2\text{K}$. This value has been obtained by measurements of the workpiece temperature in the end of the process with an infrared camera (see chapter 4.7) and comparing simulative results with varying HTC.

This procedure requires turning off the emulsion cooling in the end of the process, which takes a certain time in which the temperature distribution over the workpiece changes. Also the resolution of the infrared camera is limited both with respect to time and space. Furthermore, the temperature on the workpiece surface is inhomogenous and non-constant. The emission coefficient ε used by the infrared camera could only be measured with a certain uncertainty and the distribution of remaining emulsion drops on the workpiece can cause slight changes in ε . All these influences lead to uncertainties in the determined HTC. To investigate the influence of these uncertainties on the simulative results, again a sensitivity analysis is performed by simulating the same process R3 varying only the HTC by $\pm 20\%$.

Evaluating the results from Figure 83 it was found that the HTC varied by 20% has barely any influence on the triaxiality, while increasing the HTC slightly increases the normalized Lode angle parameter. It also shows a small influence on the resulting core strains. This effect is likely caused by the temperature dependence of the flow curve: The smaller the HTC (less cooling) the higher the temperature on the workpiece surface. This causes a reduced yield stress near the workpiece surface compared to the core that is still at a lower temperature. The reduced yield stress causes more plastic material flow on the outer radii in comparison to the workpiece core, in other words a smaller core strain. The overall influence of the heat transfer coefficient is also small though.

5.4.3 Discretization error

To investigate the sensitivity of the numerical results on the mesh size, simulations were performed under varying mesh sizes. First, the influence of the core mesh size (see Figure 58) was investigated, keeping the outer mesh constant. Secondly, the influence of the outer mesh was investigated, keeping the core mesh constant. This uncoupled investigation makes it possible to assess whether the resolution of the rolling contact and strain gradients at the outer radii (outer mesh) or the resolution of strain gradients in the core (core mesh) are of major numerical importance. The reference configuration has a core mesh size of 0.2mm and a surrounding mesh size of 0.4mm. This is equivalent to 1.9% and 3.7% of the initial bar diameter.

5.4.3.1 Core Mesh

The core mesh was set to 0.1mm and 0.4mm (1% and 3.8% of the initial bar diameter) respectively, keeping the outer mesh constant (see Figure 84). It was found that for the varying core mesh sizes both stress- and strain states in the core are nearly fully equal when further reducing the mesh size, while a further increase of mesh size changes both stress and strain states. For this reason, the chosen core mesh size in the standard configuration (0.2mm edge size) is adequate.

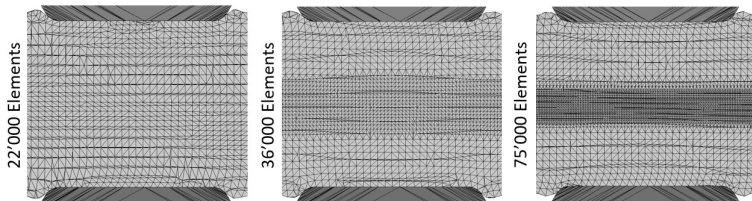


Figure 84: Variation of the core mesh size

5.4.3.2 Outer Mesh

The outer mesh size was set to 0.2mm and 0.8mm (1.9% and 7% of the initial bar diameter), respectively, keeping the core mesh constant (see Figure 85).

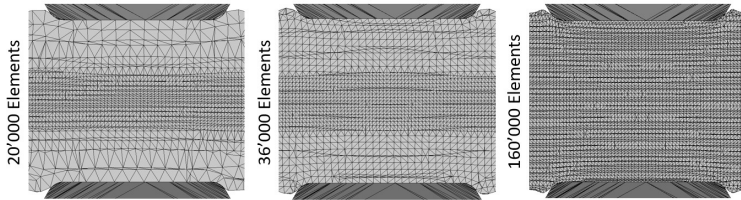


Figure 85: Variation of the outer mesh size

Simulations with an increased mesh size of the outer mesh gave higher core strains, lower triaxiality and lower Lode angle parameters (see Figure 83). This may be because the large elements will not be able to model the nearly line contact that is prevailing in cross rolling processes correctly. Instead, they will enlarge the acting contact surface falsifying reality. Additionally, the large elements are not able to reproduce the high strain and stress gradients near the contact zone correctly. These effects can then lead to slightly overestimated core strains.

These results indicate that computations with a finer outer mesh would be even a bit more accurate. On the other hand a decrease of the outer mesh size significantly increases the number of elements (up to 160000 for edge size 0.2mm) and as a result the duration of the numerical analysis (up to 70 hours on 6 cores for R3). For simulations of experiments with the narrow rollers, that reduce the workpiece diameter much further, the computational duration was found to be even higher. The limited additional accuracy in case of the very fine mesh size would not justify the significant decrease of computational efficiency, which is why the default outer mesh size of 0.4mm is considered a reasonable choice.

5.4.4 Modeling of material hardening

The material hardening behavior affects the predicted diameter reduction of crack initiation in two ways. First, it affects the ratio Y (equation 5.2.1) or in other words the resulting core strain in the simulation at a given workpiece diameter reduction. Secondly, a varying hardening curve changes the shape of the MC fracture criterion especially in the high strain regime. These two effects are investigated more in detail here.

5.4.4.1 Simulated core strains and stresses

Increasing the slope of the hardening curve caused increased simulated core strains at increased Lode angle parameters, with only minor changes in triaxiality as illustrated in Figure 83. It is intuitive that the higher the difference in flow stress between the heavily deformed outer radius of the sample and the less deformed core of the sample, in other words the steeper the flow curve, the more the material will tend to flow in the core. The overall influence of the hardening coefficient on the simulated strain and stress results in the workpiece core is significant.

5.4.4.2 Shape of the MC fracture criterion

Since the Mohr Coulomb fracture criterion in the mixed stress strain space $\{\bar{\epsilon}, \eta, \bar{\theta}\}$ representation is derived from its representation in the modified Haigh Westergaard space $\{\bar{\sigma}, \eta, \bar{\theta}\}$ through the material's hardening curve, the common representation of the MC criterion implicitly contains the used hardening curve as described in (Komischke & Hora, 2018). In this section, the sensitivity of the shape of the fracture criterion on the used hardening formulation is investigated.

To do so, the material's hardening curve (chapter 3.3) has been manipulated. In particular, the material's hardening exponent n has been set to specific values from 0.04 to 0.2, while the others parameters of the hardening curve were identified according to the least square method (equation 3.3.4). The constraint from equation 3.3.5 was not enforced. The obtained hardening curve approximations were then inserted into the formulation of the MC criterion in the mixed stress strain space (equation 2.5.26). The MC criterion's parameters have finally been identified in accordance with chapter 3.5 for each hardening curve approximation, given the experimental fracture results from chapter 3.4. The shape of the MC criterion has also been identified assuming the Hockett-Sherby hardening curve approximation identified in chapter 3.3. It can be seen as a limiting case since this flow curve approach is saturating, meaning the slope of the hardening curve approaches zero for $\bar{\epsilon} \rightarrow \infty$.

The results are given in Figure 86. The criterion changes its shape most significantly in the regime of high strain values since a varying extrapolation of the hardening curve mostly affects the stress strain relation for high strain values. For the Hockett Sherby hardening curve approximation, the Mohr Coulomb fracture criterion approaches infinite fracture strains for certain stress states $\{\eta, \bar{\theta}\}$ meaning that the equivalent stress at which fracture occurs will never be reached. The steeper the slope of the hardening curve (increasing n), the lower the fracture strains at which the respective effective stress of fracture is reached. The effect of these manipulations is the highest for the fracture strains predicted for rolling experiments R6 and R7 since these two experiments showed the highest fracture strains.

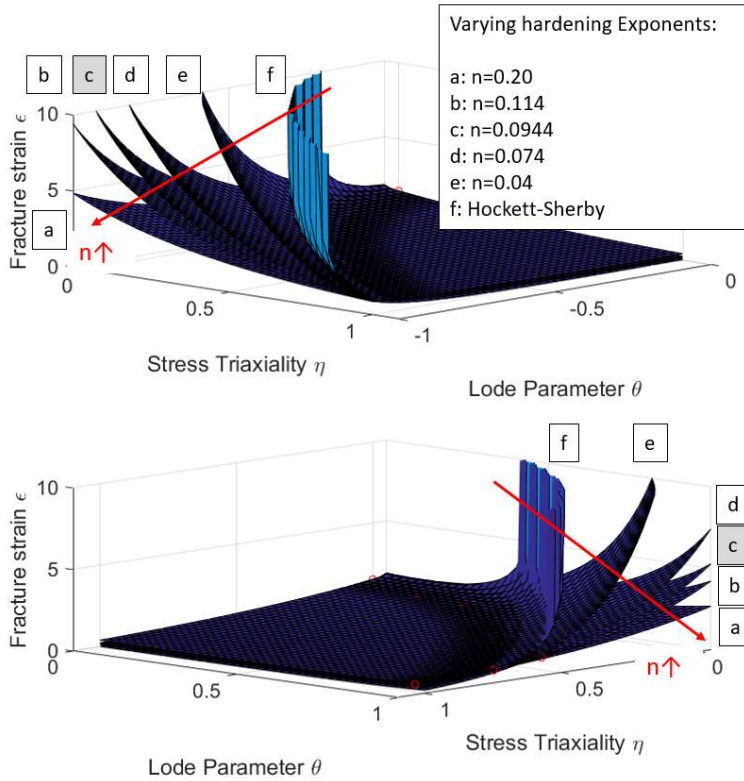


Figure 86: Sensitivity of the Mohr-Coulomb fracture criterion to the slope of the hardening curve. Top: Negative Lode Parameter Regime, Bottom: Positive Lode Parameter Regime

5.4.4.3 Combined effect

To quantify these qualitative insights, the effect of these manipulations on the predicted fracture strains will be quantified for the two n-values that vary by only $\pm 21\%$ (see letters b and d in Figure 86) from the reference n-value (see letter c in Figure 86) identified in chapter 3.3. Since the effects of this manipulation are the highest for rolling experiments R6 and R7, these two experiments have been re-simulated under the use of the modified hardening curves and modified MC criteria (letters b and d in Figure 86). The accumulated damages at the diameters of crack initiation are given in Figure 87.

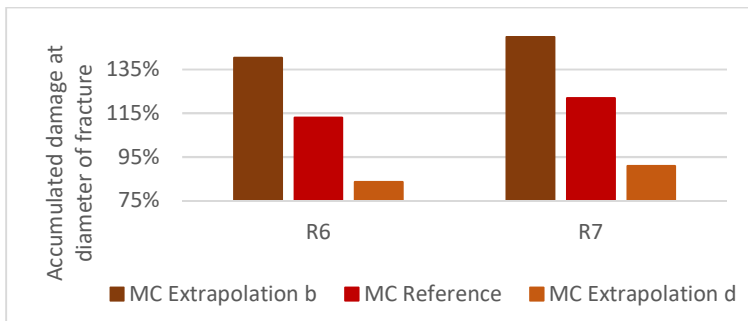


Figure 87: Effect of hardening curve extrapolation on damage for R6 and R7

It is apparent that an n-value decreased by 21% (extrapolation d in Figure 86) significantly decreases damage at instant of fracture for R6 and R7. This is because a decreased hardening exponent n decreases the simulated core strains for R6 and R7 at a given diameter reduction, while at the same time a decreased n increases the MC-predicted fracture strains for R6 and R7 remarkably. Both effects together then result in a decreased damage. This shows that the correct determination and extrapolation of the hardening curve is essential for the correct core crack prediction in cross rolling experiments using the MC fracture criterion.

5.4.5 Summary on numerical robustness

The overall robustness and reliability of simulated numerical results in the workpiece core is good. While effects like the friction and the modelling of the heat transfer to the environment through emulsion cooling proved to have minor influence on results, other influences are of higher importance.

The mesh size did show an influence on results. While a further decrease of the inner mesh size didn't change results anymore, a decrease of the outer mesh size showed an influence on results. Since the difference in computational results was small compared to the reference configuration (3% with respect to fracture strains) and a decrease of the outer mesh size increases computational effort significantly, the chosen reference mesh (see Figure 58) is a reasonable choice.

The extrapolation of the hardening curve for high strain values showed the most significant influence on results. This extrapolation influences the damage in the workpiece core in two ways. First, it changes the numerically obtained strains and stresses in the workpiece core. Secondly, it changes the shape of the MC fracture criterion in its mixed stress strain formulation. In this study, nevertheless, this sensitivity doesn't question the obtained results, since the hardening curve's extrapolation to high strains was verified carefully by both torsion tests and hardness measurements on cross rolled samples.

6 Summary and conclusions

An experimental method to investigate the core crack occurrence in cross rolling operations making use of specifically designed rollers of varying width was developed. The experimental procedure delivers well repeatable and controllable results with respect to core crack initiation on the investigated material 20MnB4. A simplified one dimensional machine stiffness model for rolling processes was developed and a method to implement it into the planning of the experimental program is given. A method for the determination of the instant of internal core crack initiation was developed. A comparison between different methods for crack investigation showed that a cheap cutting and polishing procedure delivers good results and expensive non-destructive X-Ray methods are not necessary for precise crack investigation. The fracture results are showing that the width of a notch rolled into the workpiece has enormous influence on the initiation of core cracks. Also the number of workpiece revolutions to a certain diameter reduction shows an influence.

In order to be able to virtually model the cross rolling process, the material's hardening behavior and the material's fracture behavior have to be modelled. To model the material's hardening behavior, dilatometer compression tests are an adequate choice. A methodology to correct the results for friction effects is applied. Identifying the mathematical hardening description's parameters was performed in a way that is especially focusing on an accurate extrapolation. Two approaches to verify the large strain hardening behavior are applied. The first one makes use of torque curves from torsion experiments, while the second one approximates the yield stress of previously rolled samples from hardness measurements, while it determines the corresponding strains through simulations. Both approaches indicate that the non-saturating Hensel Spittel flow curve approximation is most accurate for the investigated material.

To model the material's fracture behavior, tensile tests and torsion tests with superimposed tension or compression are performed to

investigate the material's stress state dependency of fracture behavior. Also the material's temperature and strain rate behavior was investigated in order to derive the fracture model's constraints with respect to temperature and strain rate. A Johnson-Cook, a Hosford-Coulomb and a Mohr-Coulomb ductile fracture model were fitted to the experimental fracture data. Since all these models are able to model the fracture behavior of tensile and torsion tests with a similar accuracy, a process near investigation of the fracture behavior in cross rolling operations is needed.

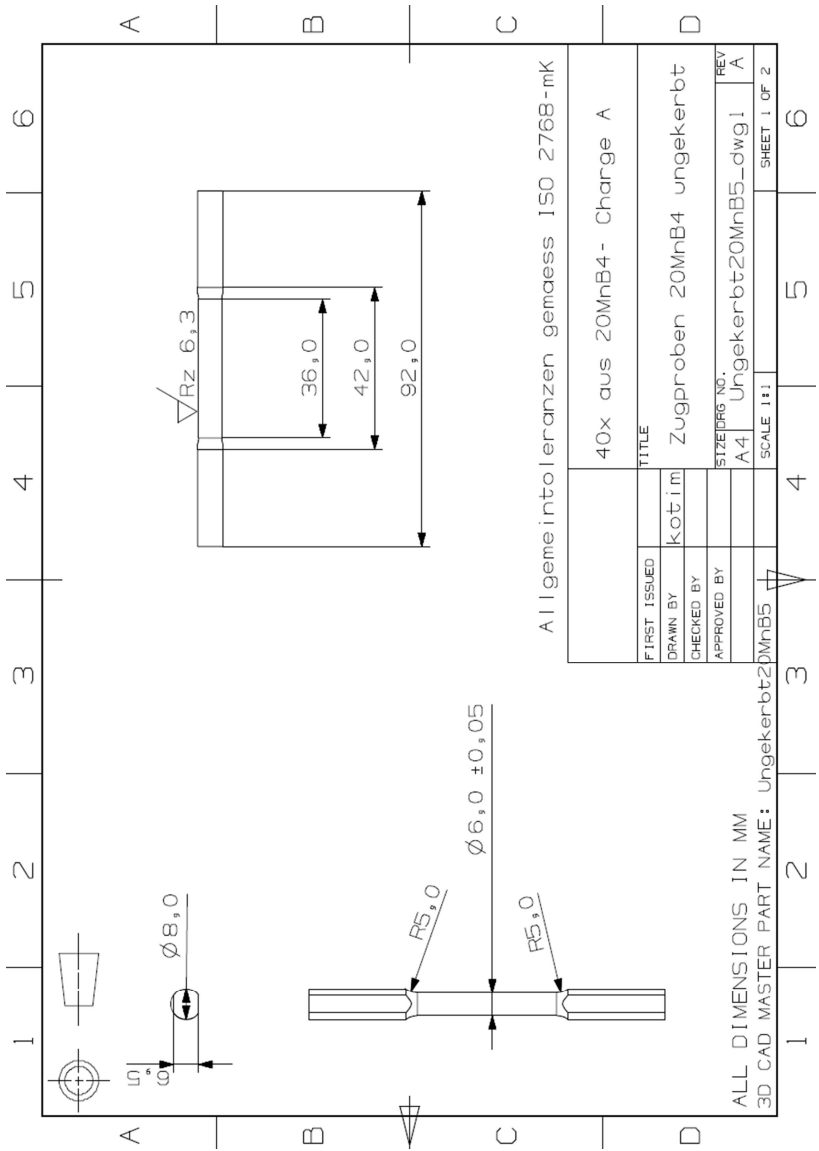
A virtual model of the cross rolling experiments is developed and runs in a stable way. It gives a reliable foundation to assess stress and strain states to fracture. To validate the model, force and torque evolution over the process were compared between experiment and simulation. A very good agreement was found. This justifies the use of a purely isotropic hardening model without the incorporation of kinematic hardening effects for the performed simulations. An analysis of the stress state in the workpiece core shows that the wider the roller the more intense the tensile stress state in the core during deformation. Narrow rollers deform the workpiece core under lower stress triaxiality and normalized Lode angle parameter closer to -1. The stress states under which core cracks happen are found to be far from the ones reached by standard fracture experiments, such as tension and torsion experiments, which makes these cross rolling experiments revealing from the point of view of ductile fracture research.

The previously calibrated ductile fracture criteria were implemented as subroutines into commercial finite element packages. Like this, the damage distribution over the workpiece in the simulations of the cross rolling experiments was evaluated. The location of crack initiation is generally predicted well by all investigated monotonic ductile fracture criteria. An analysis of damage evolution in the critical particles in the workpiece core for the whole experimental program delivers that with an average error in damage at the diameter of crack initiation of 15% the Mohr Coulomb fracture criterion delivers the highest accuracy. The error in predicted diameter reduction to fracture is even lower with only 7% for the MC model. Although the HC model is meant to be an extension of the MC model, for the investigated process it

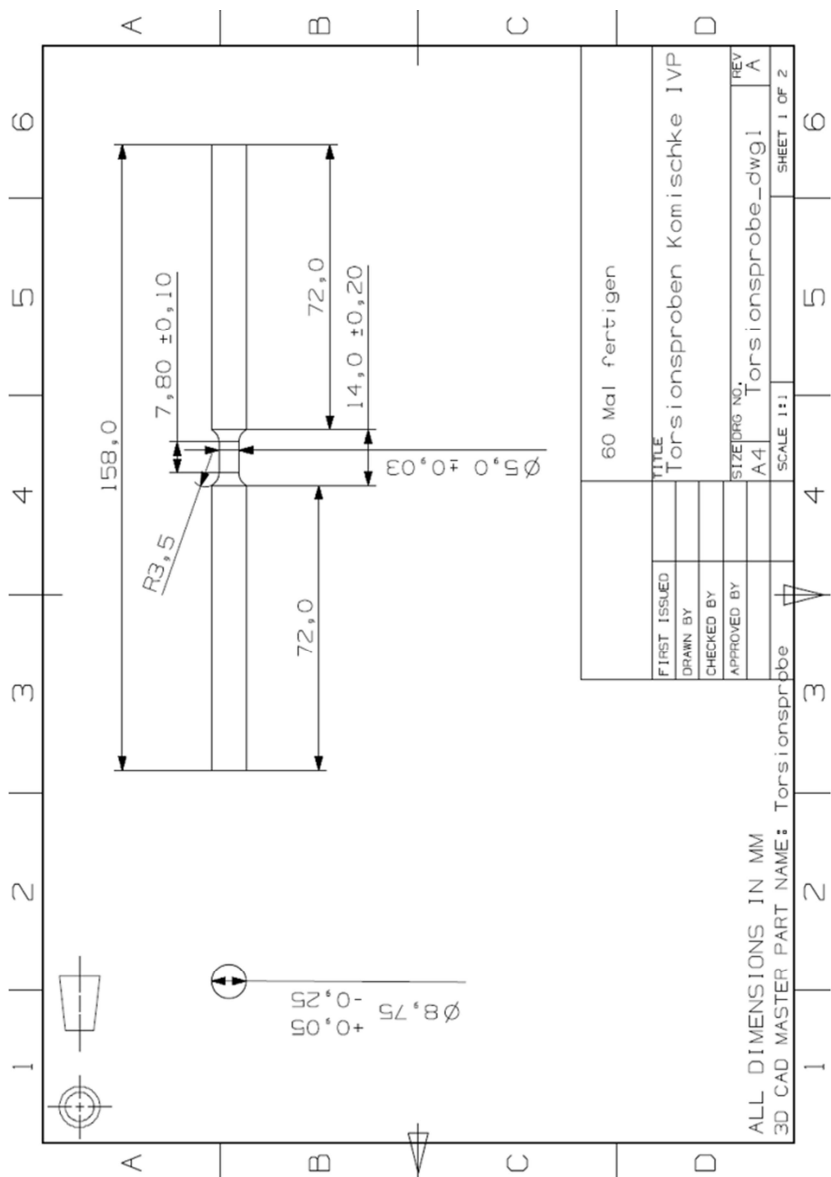
showed a lower accuracy in core crack prediction. The errors of the JC fracture model are the highest, especially for experiments with normalized Lode angle parameter close to -1, indicating that fracture criteria being formulated independently of the Lode angle parameter can lack accuracy for certain applications.

To assess the reliability of the numerical results, a robustness analysis was performed in which various input parameters to the numerical cross rolling simulations were varied. These investigated parameters include friction, process cooling, hardening curve approximation and workpiece discretization. For all the varied input parameters the change of numerical stress and strain results in the workpiece core was assessed. The total reliability of numerical results has been proven to be good, even though the correct extrapolation of the hardening curve to high strain values is shown to be very important to obtain reliable results in simulations of cross rolling operation.

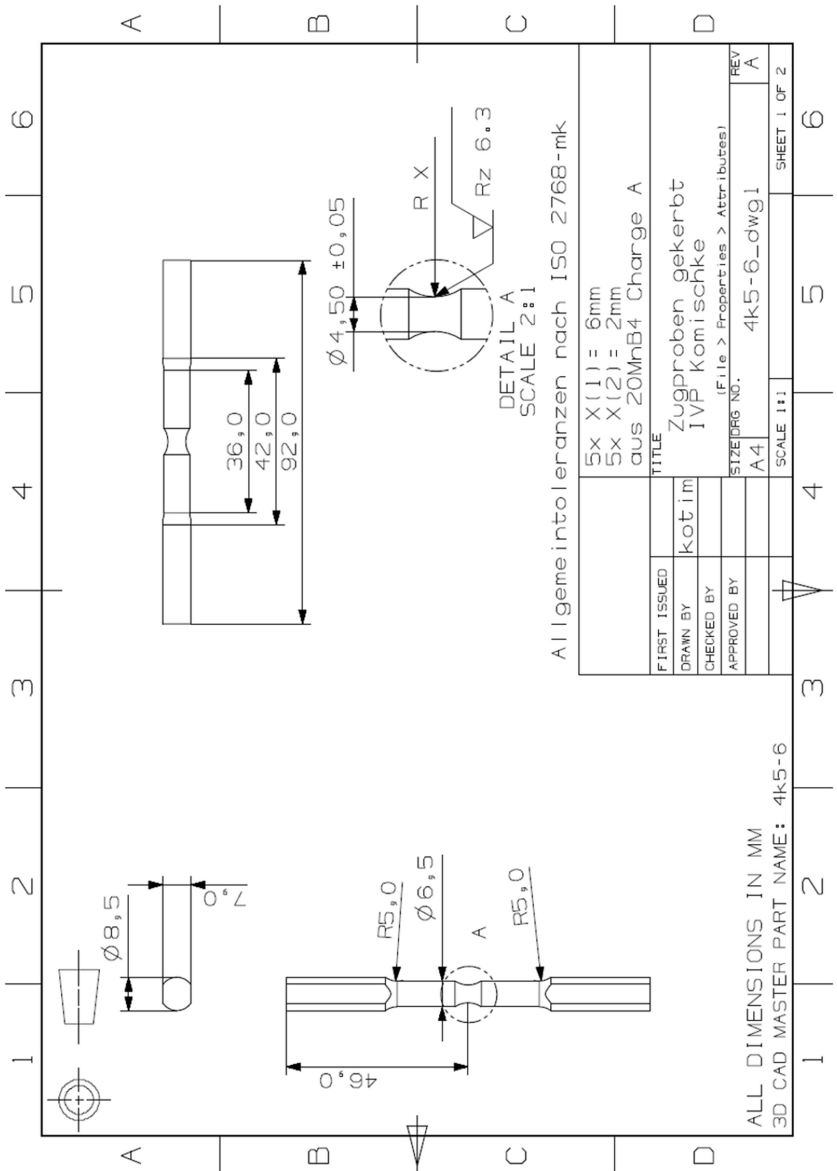
An approach to assess the fracture models' robustness is given. It consists of reducing the number of fracture experiments used for calibration of the criteria and re-evaluating them using the remaining fracture experiments. It was found that performing these re-calibration of criteria under a reduced number of experiments, the MC criterion delivers the least variation of shape of the criterion in the mixed stress strain space and the smallest maximum errors of all criteria. For this reason this criterion is judged to be more robust than the other two investigated fracture criteria.



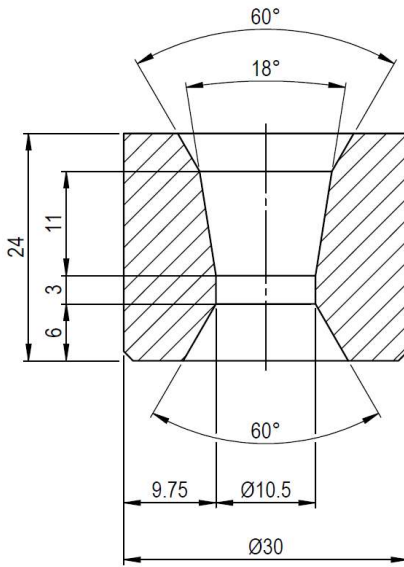
Appendix 2: Technical drawing of used unnotched tensile specimens



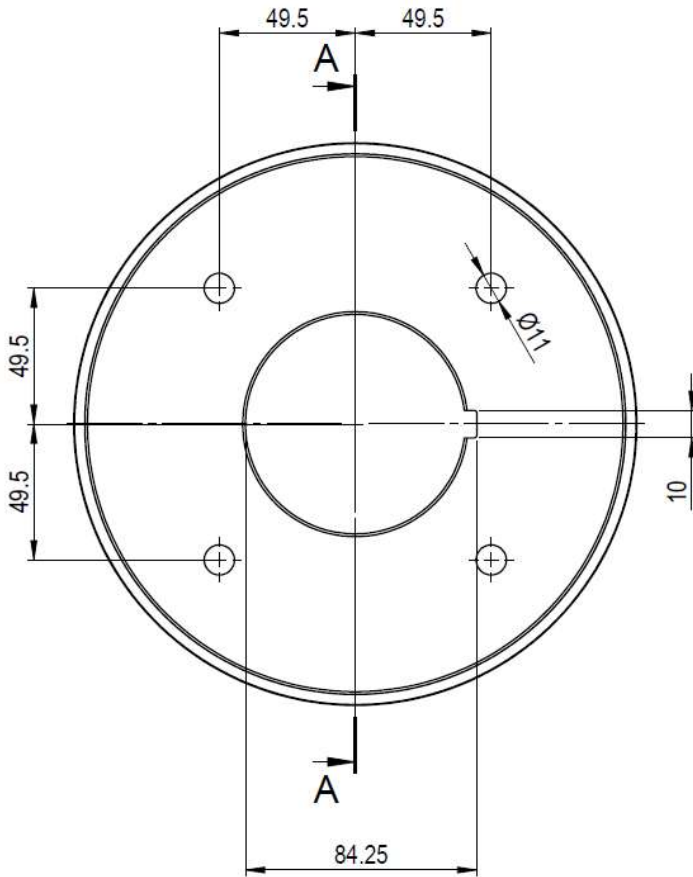
Appendix 3: Technical drawing of used torsion specimens



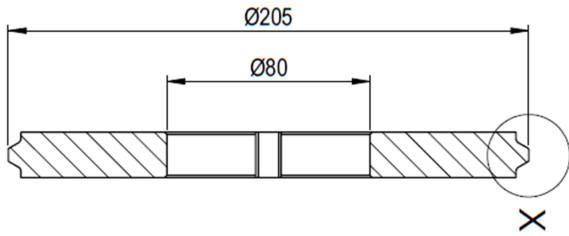
Appendix 4: Technical drawing of used notched tensile specimens



Appendix 5: Technical drawing of used drawing die AK30-75-10,50-18 (measures in [mm])

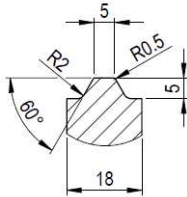


Appendix 6: Technical drawing of used roller segments (1/2) (measures in [mm])

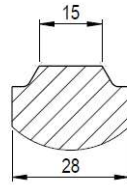


A-A

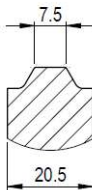
X Var B5



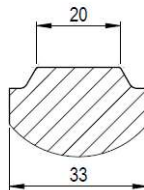
X Var B15



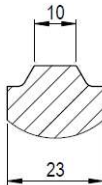
X Var B7.5



X Var B20



X Var B10



Appendix 7: Technical drawing of used roller segments (2/2) (measures in [mm])

	Value	Unit
Machine	Vtomex s 240 (GE)	-
Sensor	DXR 250	-
Accelerating voltage	210	kV
Current	50	μ A
Exposure time	4	s
Pictures for averaging	20	Pictures

Appendix 8: Parameters of X-Ray analysis

R1: 20mm Roller X=6 Rev./mm- 15Rpm	Diameter [mm]	Diameter reduction [mm]	Average core crack class	Number of rolled samples	Thereof no core crack	Thereof crack class 1	Thereof crack class 2	Thereof crack class 3
	10.38	0.12	0	2	2	0	0	0
	10.25	0.25	0	3	2	1	0	0
	10.2	0.3	0	6	5	1	0	0
	10.15	0.35	1	5	1	4	0	0
	10.1	0.4	2	4	0	0	4	0
	10.05	0.45	2	3	0	0	3	0
	10.01	0.49	3	2	0	0	0	2
R2: 15mm Roller X=6 Rev./mm- 15Rpm	Diameter [mm]	Diameter reduction [mm]	Average core crack class	Number of rolled samples	Thereof no core crack	Thereof crack class 1	Thereof crack class 2	Thereof crack class 3
	10.2	0.3	0	4	2	1	0	0
	10.1	0.4	0	4	3	0	0	0
	10	0.5	2	4	0	1	3	0
	9.9	0.6	3	4	0	0	0	4
R3: 10mm Roller, X=6 Rev./mm- 15Rpm	Diameter [mm]	Diameter reduction [mm]	Average core crack class	Number of rolled samples	Thereof no core crack	Thereof crack class 1	Thereof crack class 2	Thereof crack class 3
	10.1	0.4	0	2	2	0	0	0
	9.86	0.64	0	2	2	0	0	0
	9.82	0.68	0	3	2	1	0	0
	9.69	0.81	0	4	3	1	0	0
	9.62	0.88	0	2	1	1	0	0
	9.58	0.92	1	5	2	2	1	0
	9.48	1.02	1	4	1	2	1	0
	9.34	1.16	2	2	0	0	2	0
	9.06	1.44	3	2	0	0	0	2
R4: 7.5mm Roller, X=6 Rev./mm, 15Rpm	Diameter [mm]	Diameter reduction [mm]	Average core crack class	Number of rolled samples	Thereof no core crack	Thereof crack class 1	Thereof crack class 2	Thereof crack class 3
	9.01	1.49	0	2	2	0	0	0
	8.9	1.6	0	3	3	0	0	0
	8.8	1.7	1	5	1	4	0	0
	8.7	1.8	1	4	0	3	1	0
	8.6	1.9	2	4	0	1	1	0
	8.5	2	2	5	0	3	1	0
	8.4	2.1	2	2	0	0	1	0
	8.26	2.24	2	2	0	0	2	0
	8	2.5	2	2	0	0	2	0
	7.45	3.05	3	2	0	0	0	2

Appendix 9: Detailed results of cross rolling experiments (1/2)

R5: 7.5mm Roller, X=2 Rev./mm, 5Rpm	Diameter [mm]	Diameter reduction [mm]	Average core crack class	Number of rolled samples	Thereof no core crack	Thereof crack class 1	Thereof crack class 2	Thereof crack class 3
	8.45	2.05	0	3	2	0	0	0
	8.3	2.2	0	4	3	1	0	0
	8.2	2.3	1	9	1	5	1	0
	8.05	2.45	1	2	0	2	0	0
	7.95	2.55	1	6	0	5	1	0
	7.8	2.7	2	8	1	2	4	0
	7.6	2.9	2	8	1	2	4	0
	7.3	3.2	2	3	0	1	2	0
	7.1	3.4	2	3	0	1	2	0
6.9	3.6	3	3	0	0	1	2	
R6: 5.0mm Roller, X= 4 Rev./mm- 10Rpm	Diameter [mm]	Diameter reduction [mm]	Average core crack class	Number of rolled samples	Thereof no core crack	Thereof crack class 1	Thereof crack class 2	Thereof crack class 3
	7	3.5	0	4	3	0	0	0
	6.8	3.7	0	4	4	0	0	0
	6.55	3.95	1	4	0	1	1	0
	6.26	4.24	2	4	0	2	2	0
	6	4.5	2	5	0	0	5	0
R7: 5.0mm Roller, X=2 Rev./mm- 5Rpm	Diameter [mm]	Diameter reduction [mm]	Average core crack class	Number of rolled samples	Thereof no core crack	Thereof crack class 1	Thereof crack class 2	Thereof crack class 3
	7.1	3.4	0	4	4	0	0	0
	6.6	3.9	0	4	4	0	0	0
	6.3	4.2	0	5	4	0	0	0
	6.05	4.45	1	4	2	1	1	0
	5.95	4.55	1	5	2	2	1	0
	5.7	4.8	1	5	2	1	1	0
	5.5	5	2	9	0	3	3	2

Appendix 10: Detailed results of cross rolling experiments (2/2)

List of references

- Bai, Y., & Wierzbicki, T. (2008). A new model of metal plasticity and fracture with pressure and Lode dependence. *International Journal of Plasticity*, 24(6), 1071-1096. doi:<http://dx.doi.org/10.1016/j.ijplas.2007.09.004>
- Bai, Y., & Wierzbicki, T. (2015). A comparative study of three groups of ductile fracture loci in the 3D space. *Engineering fracture mechanics*, 135, 147-167. doi:<https://doi.org/10.1016/j.engfracmech.2014.12.023>
- Bai, Y., & Wierzbicki, T. (2010). Application of extended Mohr-Coulomb criterion to ductile fracture. *International Journal of Fracture*, 161, 1-20.
- Bao, Y., & Wierzbicki, T. (2005). On the cut-off value of negative triaxiality for fracture. *Engineering Fracture Mechanics*, 72(7), 1049-1069. doi:<https://doi.org/10.1016/j.engfracmech.2004.07.011>
- Barsoum, I., & Faleskog, J. (2007). Rupture mechanisms in combined tension and shear—Experiments. *International Journal of Solids and Structures*, 44(6), 1768-1786. doi:<http://dx.doi.org/10.1016/j.ijsolstr.2006.09.031>
- Bathe, K.-J. (2006). *Finite element procedures*. Englewood Cliffs N.J.: Prentice Hall.
- Belytschko, T., Liu, W. K., & Moran, B. (2000). *Nonlinear Finite Element Analysis for Continua and Structures* (1. Auflage ed.): John Wiley & Sons.
- Besson, J., Steglich, D., & Brocks, W. (2001). Modeling of crack growth in round bars and plane strain specimens. *International Journal of Solids and Structures*, 38(46), 8259-8284. doi:[https://doi.org/10.1016/S0020-7683\(01\)00167-6](https://doi.org/10.1016/S0020-7683(01)00167-6)
- Brozzo, P., Deluca, B., & Rendina, R. (1972). *A new method for the prediction of the formability limits of plastic sheets*.
- Çakırcalı, M., Kılıçaslan, C., Güden, M., Kıranlı, E., Shchukin, V. Y., & Petronko, V. V. (2013). Cross wedge rolling of a Ti6Al4V (ELI) alloy: the experimental studies and the finite element simulation of the deformation and failure. *The International Journal of Advanced Manufacturing Technology*, 65(9), 1273-1287. doi:10.1007/s00170-012-4256-3

- Carvill, J. (1993). 3 - Thermodynamics and heat transfer. In J. Carvill (Ed.), *Mechanical Engineer's Data Handbook* (pp. 102-145). Oxford: Butterworth-Heinemann.
- Cockroft, M., & Latham, D. (1968). Ductility and the Workability of Metals. *Journal of the institute of metals*, 96, 33-39.
- Colpaert, H. (2018). *Metallography of Steels: Interpretation of Structure and the Effects of Processing*: ASM International.
- Coppola, T., Iob, F., & Campanelli, F. (2014). Critical Review of Ductile Fracture Criteria for Steels. *Procedia Materials Science*, 3, 1548-1553.
doi:<http://dx.doi.org/10.1016/j.mspro.2014.06.250>
- Coulomb, C. A. (1776). Essai sur une application des regles des maximis et minimis a quelques problemes de statique relatifs a l'architecture. Memoires de l'Academie. *Royale pres Divers Savants*, 7.
- Danas, K., & Aravas, N. (2012). Numerical modeling of elasto-plastic porous materials with void shape effects at finite deformations. *Composites Part B: Engineering*, 43(6), 2544-2559.
doi:<http://dx.doi.org/10.1016/j.compositesb.2011.12.011>
- de Borst, R., & Verhoosel, C. V. (2018). Damage, material instabilities, and failure. *Encyclopedia of Computational Mechanics Second Edition*, 1-50.
- DIN1547. (1969-07). *Hartmetall-Ziehsteine und -Ziehringe; Begriffe, Bezeichnung, Kennzeichnung*.
- DIN8583-2. (2003-09). *Fertigungsverfahren Druckumformen- Teil2: Walzen; Einordnung, Unterteilung, Begriffe*.
- Dong, Y., Tagavi, K. A., Lovell, M. R., & Deng, Z. (2000). Analysis of stress in cross wedge rolling with application to failure. *International Journal of Mechanical Sciences*, 42(7), 1233-1253. doi:[https://doi.org/10.1016/S0020-7403\(99\)00035-1](https://doi.org/10.1016/S0020-7403(99)00035-1)
- Dunand, M., & Mohr, D. (2014). Effect of Lode parameter on plastic flow localization after proportional loading at low stress triaxialities. *Journal of the Mechanics and Physics of Solids*, 66, 133-153.
doi:<https://doi.org/10.1016/j.jmps.2014.01.008>
- EN-10263-4. (2002). *Steel rod, bars and wire for cold heading and cold extrusion- Part 4: Technical delivery conditions for steels for quenching and tempering*.

- Freudenthal, A. M. (1950). *The Inelastic Behavior of Engineering Materials and Structures*. New York: Wiley; London: Chapman.
- Fritz, A. H., & Schulze, G. (2010). *Fertigungstechnik* (Vol. 1). Berlin: Springer Verlag.
- Gao, X., Zhang, T., Zhou, J., Graham, S. M., Hayden, M., & Roe, C. (2011). On stress-state dependent plasticity modeling: Significance of the hydrostatic stress, the third invariant of stress deviator and the non-associated flow rule. *International Journal of Plasticity*, 27(2), 217-231. doi:<https://doi.org/10.1016/j.ijplas.2010.05.004>
- Ghiotti, A., Fanini, S., Bruschi, S., & Bariani, P. F. (2009). Modelling of the Mannesmann effect. *CIRP Annals*, 58(1), 255-258. doi:<https://doi.org/10.1016/j.cirp.2009.03.099>
- Ghosh, A. K. (1977). The influence of strain hardening and strain-rate sensitivity on sheet metal forming. *Journal of Engineering Materials and Technology*, 99, 264.
- Gil Sevillano, J., van Houtte, P., & Aernoudt, E. (1980). Large strain work hardening and textures. *Progress in Materials Science*, 25(2), 69-134. doi:[https://doi.org/10.1016/0079-6425\(80\)90001-8](https://doi.org/10.1016/0079-6425(80)90001-8)
- Gorji Bandpay, M. (2015). *Instability and Fracture Models to Optimize the Metal Forming and Bending Crack Behavior of Al- Alloy Composites*. ETH-Zürich. Retrieved from <http://hdl.handle.net/20.500.11850/107677>
- Gorni, A. A., & Soares, M. R. S. d. (2015). MICROSTRUCTURAL EVOLUTION OF THE NORMALIZING PLATE ROLLING OF NIOBIUM MICROALLOYED STEELS. *Tecnologia em Metalurgia, Materiais e Mineração*, 12(1), 72.
- Gurson, A. L. (1977). Continuum Theory of Ductile Rupture by Void Nucleation and Growth: Part I---Yield Criteria and Flow Rules for Porous Ductile Media. *Journal of Engineering Materials and Technology*, 99, 2-15. doi:10.1115/1.3443401
- Han, H. (2002). The validity of mathematical models evaluated by two-specimen method under the unknown coefficient of friction and flow stress. *Journal of Materials Processing Technology*, 122(2), 386-396. doi:[https://doi.org/10.1016/S0924-0136\(02\)00059-6](https://doi.org/10.1016/S0924-0136(02)00059-6)

- Hancock, J. W., & Mackenzie, A. C. (1976). On the mechanisms of ductile failure in high-strength steels subjected to multi-axial stress-states. *Journal of the Mechanics and Physics of Solids*, 24, 147-160. doi:10.1016/0022-5096(76)90024-7
- Hensel, A., & Spittel, T. (1979). *Kraft- und Arbeitsbedarf bildsamer Formgebungsverfahren*. Leipzig: Deutscher Verlag für Grundstoffindustrie.
- Hershey, A. V. (1954). The elasticity of an isotropic aggregate of anisotropic cubic crystals. *Journal of applied mechanics-transactions of the ASME*, 21(3), 236-240.
- Hill, R. (1948). A Theory of the Yielding and Plastic Flow of Anisotropic Metals. *Proceedings of the Royal Society of London. Series A, Mathematical and Physical Sciences*, 193, 281-297.
- Hochholdinger, B., Hora, P., & Wegener, K. (2012). *Simulation des Presshärteprozesses und Vorhersage der mechanischen Bauteileigenschaften nach dem Härten*. ETH, Zürich. Open WorldCat database.
- Hockett, J. E., & Sherby, O. D. (1975). Large strain deformation of polycrystalline metals at low homologous temperatures. *Journal of the Mechanics and Physics of Solids*, 23, 87-98. doi:10.1016/0022-5096(75)90018-6
- Hollomon, J. H. (1945). Tensile Deformation. *Transactions of the American Institute of Mining and Metallurgical Engineers*, 162, 268–290.
- Hosford, W. F. (1979). *On yield loci of anisotropic cubic metals*. Paper presented at the Proceedings of the Seventh North American Metal working Conference SME.
- Houska, M., & Rotarescu, M. I. (1999). *EXPERIMENTAL AND FINITE-ELEMENT ANALYSIS OF AXIAL FEED BAR ROLLING (A VQ)*. Paper presented at the Proc. of the 6 th ICTP.
- Jia, Z., Zhou, J., Ji, J.-j., Yu, Y.-y., & Xiao, C. (2012). Influence of tool parameters on internal voids in cross wedge rolling of aluminum alloy parts. *Transactions of Nonferrous Metals Society of China*, 22, s21-s26. doi:[https://doi.org/10.1016/S1003-6326\(12\)61678-1](https://doi.org/10.1016/S1003-6326(12)61678-1)
- John, M. (2018). *Experimentelle und numerische Methoden zur Beschreibung tribologischer Kontakte bei Walzprozessen*. (Master Thesis), ETH Zürich.

- Johnson, G. R., & Cook, W. H. (1985). Fracture characteristics of three metals subjected to various strains, strain rates, temperatures and pressures. *Engineering fracture mechanics*, 21, 31-48. doi:10.1016/0013-7944(85)90052-9
- Johnson, W., & Mamalis, A. G. (1977). A Survey of Some Physical Defects Arising in Metal Working Processes. In S. A. Tobias (Ed.), *Proceedings of the Seventeenth International Machine Tool Design and Research Conference: held in Birmingham 20th – 24th September, 1976* (pp. 607-621). London: Macmillan Education UK.
- Komischke, T., & Hora, P. (2018). *On the sensitivity of the Mohr-Coulomb ductile fracture criterion in the mixed stress-strain space on varying hardening curve approximations*. Paper presented at the IOP Conference Series: Materials Science and Engineering.
- Komischke, T., Hora, P., & Domani, G. (2018). A New Experimental Method for the Evaluation of Fracture Criteria in Bulk Forming Operations. *Experimental and numerical methods in the FEM based crack prediction*, 65-69.
- Komischke, T., Hora, P., Domani, G., Plamondon, M., & Kaufmann, R. (2018). Prediction of crack induced failure phenomena in rolling operations. *Procedia Manufacturing*, 15, 176-184.
- Kukielka, L., & Kukielka, K. (2006). Numerical analysis of the process of trapezoidal thread rolling. *WIT Transactions on The Built Environment*, 85.
- Lange, K. (1988). *Umformtechnik- Handbuch für Industrie und Wissenschaft* (Vol. 2). Berlin Heidelberg: Springer-Verlag.
- Lemaitre, J. (1984). How to use damage mechanics. *Nuclear Engineering and Design*, 80(2), 233-245. doi:[http://dx.doi.org/10.1016/0029-5493\(84\)90169-9](http://dx.doi.org/10.1016/0029-5493(84)90169-9)
- Li, Q., & Lovell, M. (2008). Cross wedge rolling failure mechanisms and industrial application. *The International Journal of Advanced Manufacturing Technology*, 37(3), 265-278. doi:10.1007/s00170-007-0979-y
- Li, Q., & Lovell, M. R. (2004). The establishment of a failure criterion in cross wedge rolling. *The International Journal of Advanced Manufacturing Technology*, 24(3), 180-189. doi:10.1007/s00170-003-1607-0
- Li, Q., Lovell, M. R., Slaughter, W., & Tagavi, K. (2002). Investigation of the morphology of internal defects in cross

- wedge rolling. *Journal of Materials Processing Technology*, 125-126, 248-257. doi:[https://doi.org/10.1016/S0924-0136\(02\)00303-5](https://doi.org/10.1016/S0924-0136(02)00303-5)
- Lode, W. (1926). Versuche über den Einfluß der mittleren Hauptspannung auf das Fließen der Metalle Eisen, Kupfer und Nickel. *Zeitschrift für Physik*, 36, 913-939. doi:10.1007/BF01400222
- Ludwik, P. (1909). *Elemente der technologischen Mechanik*. Berlin: J. Springer.
- Malvern, L. E. (1969). *Introduction to the mechanics of a continuous medium*. Englewood Cliffs, N.J: Prentice-Hall.
- Manopulo, N. (2011). *An ALE based FE formulation for the 3D simulation of the fineblanking process*. Zürich: ETH/Institut für virtuelle Produktion.
- McClintock, F., Kaplan, S., & Berg, C. (1966). Ductile fracture by hole growth in shear bands. *International Journal of Fracture Mechanics*, 2. doi:10.1007/BF00184558
- McClintock, F. A. (1968). A Criterion for Ductile Fracture by the Growth of Holes. *Journal of Applied Mechanics*, 35, 363-371. doi:10.1115/1.3601204
- Mohr, D., & Marcadet, S. (2015). Micromechanically-motivated phenomenological Hosford-Coulomb model for predicting ductile fracture initiation at low stress triaxialities. *International Journal of Solids and Structures*, 67-68, 40-55.
- Mohr, O. (1914). *Abhandlungen aus dem Gebiete der technischen Mechanik* (2.Aufl. ed.). Berlin: WERNST.
- MSC-Software. (2015). Marc Manual, Volume C: Program Input.
- Nahshon, K., & Hutchinson, J. W. (2008). Modification of the Gurson Model for shear failure. *European Journal of Mechanics - A/Solids*, 27(1), 1-17. doi:<http://dx.doi.org/10.1016/j.euromechsol.2007.08.002>
- Neugebauer, R., Hellfritsch, U., & Lahl, M. (2008). Advanced process limits by rolling of helical gears. *International Journal of Material Forming*, 1(1), 1183-1186. doi:10.1007/s12289-008-0152-7
- Neukamm, F., Feucht, M., & Haufe, A. (2008). *Consistent Damage Modelling in the Process Chain of Forming to Crashworthiness Simulations*. Paper presented at the LS-DYNA Anwenderforum, Bamberg.

- Noneder, H., & Merklein, M. (2012). Manufacturing of complex high strength components out of high nitrogen steels at industrial level. *Transactions of Nonferrous Metals Society of China*, 22, s512-s518. doi:[https://doi.org/10.1016/S1003-6326\(12\)61754-3](https://doi.org/10.1016/S1003-6326(12)61754-3)
- Novella, M. F., Ghiotti, A., Bruschi, S., & Bariani, P. F. (2015). Ductile damage modeling at elevated temperature applied to the cross wedge rolling of AA6082-T6 bars. *Journal of Materials Processing Technology*, 222, 259-267. doi:<https://doi.org/10.1016/j.jmatprotec.2015.01.030>
- Pater, Z., Gontarz, A., & Weronki, W. (2004). New method of thread rolling. *Journal of Materials Processing Technology*, 153, 722-728.
- Pavlina, E. J., & Van Tyne, C. J. (2008). Correlation of Yield Strength and Tensile Strength with Hardness for Steels. *Journal of Materials Engineering and Performance*, 17(6), 888-893. doi:10.1007/s11665-008-9225-5
- Pineau, A., Benzerga, A. A., & Pardoën, T. (2016). Failure of metals I: Brittle and ductile fracture. *Acta Materialia*, 107, 424-483. doi:<https://doi.org/10.1016/j.actamat.2015.12.034>
- Pöhlandt, K. (2013). *Vergleichende Betrachtung der Verfahren zur Prüfung der plastischen Eigenschaften metallischer Werkstoffe* (Vol. 80): Springer-Verlag.
- Profiroll-Technologies-GmbH. (2000). PWZ40CNC/AC-Produktbeschreibung.
- Rabotnov, Y. N. (1963). Paper 68: On the Equation of State of Creep. *Proceedings of the Institution of Mechanical Engineers, Conference Proceedings*, 178(1), 2-117-112-122. doi:10.1243/PIME_CONF_1963_178_030_02
- Rice, J. R., & Tracey, D. M. (1969). On the ductile enlargement of voids in triaxial stress fields*. *Journal of the Mechanics and Physics of Solids*, 17(3), 201-217. doi:[http://dx.doi.org/10.1016/0022-5096\(69\)90033-7](http://dx.doi.org/10.1016/0022-5096(69)90033-7)
- Rousselier, G. (1987). Ductile fracture models and their potential in local approach of fracture. *Nuclear Engineering and Design*, 105, 97-111. doi:16/0029-5493(87)90234-2
- Siebel, E., & Pomp, A. (1927). Die Ermittlung der Formänderungsfestigkeit von Metallen durch den Stauchversuch. *Mitt. KWI Eisenforsch.*, 9, 157- 171.

- Silva, M. L. N., Pires, G. H., & Button, S. T. (2011). Damage evolution during cross wedge rolling of steel DIN 38MnSiVS5. *Procedia Engineering*, 10, 752-757.
- simufact-engineering-GmbH. (2016). Simufact Material Datenbank.
- Tabor, D. (1956). The physical meaning of indentation and scratch hardness. *British Journal of Applied Physics*, 7(5), 159.
- Tvergaard, V., & Needleman, A. (1984). Analysis of the cup-cone fracture in a round tensile bar. *Acta Metallurgica*, 32(1), 157-169. doi:[http://dx.doi.org/10.1016/0001-6160\(84\)90213-X](http://dx.doi.org/10.1016/0001-6160(84)90213-X)
- Voce, E. (1948). The relationship between stress and strain for homogeneous deformation. *J Inst Met*, 74, 537-562.
- voestalpineGrobblechGmbH. (2018). Normalizing rolling. Retrieved from <https://www.voestalpine.com/stahl/en/Companies/voestal-pine-Grobblech-GmbH/Technology/As-delivered-conditions/Normalizing-rolling>. Accessed on 01.04.2019
- Wang, M.-t., Li, X.-t., & Du, F.-s. (2009). Analysis of Metal Forming in Two-Roll Cross Wedge Rolling Process Using Finite Element Method. *Journal of Iron and Steel Research, International*, 16(1), 38-43. doi:[https://doi.org/10.1016/S1006-706X\(09\)60008-X](https://doi.org/10.1016/S1006-706X(09)60008-X)
- Wesner, T. (2017). *Virtuelle und experimentelle Methoden zur Voraussage des Prozessfensters beim Feinschneiden*. ETH Zürich. Retrieved from <http://hdl.handle.net/20.500.11850/129512>
- Wierzbicki, T., Bao, Y., Lee, Y.-W., & Bai, Y. (2005). Calibration and evaluation of seven fracture models. *International Journal of Mechanical Sciences*, 47(4-5), 719-743. doi:<http://dx.doi.org/10.1016/j.ijmecsci.2005.03.003>
- Wierzbicki, T., & Xue, L. (2005). On the effect of the third invariant of the stress deviator on ductile fracture. *Impact and Crashworthiness Laboratory, Technical Report*, 136.
- Xue, L. (2007). Damage accumulation and fracture initiation in uncracked ductile solids subject to triaxial loading. *International Journal of Solids and Structures*, 44(16), 5163-5181. doi:<http://dx.doi.org/10.1016/j.ijsolstr.2006.12.026>
- Zhang, D.-W., & Zhao, S.-D. (2014). New method for forming shaft having thread and spline by rolling with round dies. *The International Journal of Advanced Manufacturing Technology*, 70(5-8), 1455-1462.

List of publications

- Komischke, T., & Hora, P. (2019). The cross-compression-tension-bar-experiment for the investigation of ductile fracture near pure shear conditions. Paper accepted at the ESAFORM19 conference.
- Komischke, T., & Hora, P. (2018). On the sensitivity of the Mohr-Coulomb ductile fracture criterion in the mixed stress-strain space on varying hardening curve approximations. Paper presented at the IOP Conference Series: Materials Science and Engineering.
- Komischke, T., Hora, P., & Domani, G. (2018). A New Experimental Method for the Evaluation of Fracture Criteria in Bulk Forming Operations. Experimental and numerical methods in the FEM based crack prediction, 65-69.
- Komischke, T., Hora, P., Domani, G., Plamondon, M., & Kaufmann, R. (2018). Prediction of crack induced failure phenomena in rolling operations. *Procedia Manufacturing*, 15, 176-184.
- Hora, P., Berisha, B., Hirsiger, S., Komischke, T., & Schober, R. (2018). Critical aspects of the experimental and theoretical crack prediction in sheet and bulk metal forming. Paper presented at the 11th Forming Technology Forum 2018.
- Pfaff, J., Warhanek, M., Huber, S., Komischke, T., Hänni, F., & Wegener, K. (2016). Laser touch dressing of electroplated CBN grinding tools. *Procedia CIRP*, 46, 272-275.
- Walter, C., Komischke, T., Beyer, P., & Wegener, K. (2014). A laser micro texturing technique for performance enhancement of superabrasive grinding wheels. Paper presented at the Proceedings of the 14th international conference of the European Society for Precision Engineering and Nanotechnology: Vol. 2.
- Walter, C., Komischke, T., Kuster, F., & Wegener, K. (2014). Laser-structured grinding tools—Generation of prototype patterns and performance evaluation. *Journal of Materials Processing Technology*, 214(4), 951-961.
- Walter, C., Komischke, T., Weingärtner, E., & Wegener, K. (2014). Structuring of CBN Grinding Tools by Ultrashort Pulse Laser Ablation. *Procedia CIRP*, 14, 31-36. doi:<https://doi.org/10.1016/j.procir.2014.03.093>

Curriculum Vitae

Personal Data

Name	Tim Komischke
Date of birth	09.09.1990
Place of birth	Schweinfurt, Germany
Nationality	German

Education

2016 – 2019	Doctoral studies <i>Institute of Virtual Manufacturing, ETH Zurich, Switzerland</i>
2015	Exchange semester <i>National University of Singapore, Singapore</i>
2014 – 2016	Master of Science ETH <i>In Mechanical Engineering, ETH Zurich, Switzerland</i>
2010 – 2013	Bachelor of Science ETH <i>In Mechanical Engineering, ETH Zurich, Switzerland</i>
2001 – 2010	High School <i>Rhabanus Maurus Gymnasium St. Ottilien, Eresing, Germany</i>

Professional experience

2015	Idea Manager Fabrication costs (Master Thesis) <i>Volkswagen AG, Wolfsburg, Germany</i>
2014	Working student in Consulting <i>Soltar AG, Zurich, Switzerland</i>
2014	Application Engineer <i>Hoerbiger Corporation of America, Pompano Beach, USA</i>